LSU Doctoral Dissertations   Graduate School

2009

Size Controlled Metal Oxide Nanoparticles:Synthesis, Characterization, and Application to Catalysis

Hongyi Wu
Louisiana State University and Agricultural and Mechanical College

Follow this and additional works at: https://digitalcommons.lsu.edu/gradschool_dissertations

Part of the Chemistry Commons

Recommended Citation

Wu, Hongyi, "Size Controlled Metal Oxide Nanoparticles:Synthesis, Characterization, and Application to Catalysis" (2009). *LSU Doctoral Dissertations*. 1442.

https://digitalcommons.lsu.edu/gradschool_dissertations/1442

This Dissertation is brought to you for free and open access by the Graduate School at LSU Digital Commons. It has been accepted for inclusion in LSU Doctoral Dissertations by an authorized graduate school editor of LSU Digital Commons. For more information, please contact gradetd@lsu.edu.

SIZE CONTROLLED METAL OXIDE NANOPARTICLES: SYNTHESIS, CHARACTERIZATION, AND APPLICATION TO CATALYSIS

A Dissertation

Submitted to the Graduate Faculty of the
Louisiana State University and
Agricultural and Mechanical College
in partial fulfillment of the
requirements for the degree of
Doctor of Philosophy

in

The Department of Chemistry

by
Hongyi Wu
B.S., University of Science and Technology of China, Hefei, P.R.China, 2002
May 2010

ACKNOWLEDGEMENTS

I would especially thank my major advisor, Dr. Barry Dellinger, for his continuous support and invaluable guidance throughout this project. This work would have been impossible without his patience and support. I also thank my co-advisor, Dr. Erwin Poliacoff, for his support and helpful insight which was critical important to my research studies. I would never have accomplished all that I have without the constant wisdom, invaluable insight and understanding of Dr. Slawomir Lomnicki. I would also thank my committee members, Dr. Andrew Maverick, Dr. Robin McCarley, Dr. Charles Lindau, for their time to read my thesis and many invaluable comments.

I would thank to all the people from the Dellinger group for all the help, discussions and sharing. It is my honor to work with you, Dr. Lavrent Khachatryan, Dr. Zofia Maskos, Shadrack Nganai, Eric Vejerano, William Gehling, Albert Dela Cruz, Michael Herring and Joshua Kibet. I am grateful to all the people in our department who provided a lot of assistance.

I would give my special thank to Mr. Richard Debate for his help in assisting me to correct my grammar mistakes of thesis writing.

Finally, I would like to thank my family for their constant support and believing that I could accomplish something that is very different from what they expected. Last but not least, I wish to share this accomplishment with my loved wife, Yingqin Zhang, who not only gave me continuous support and encouragement throughout my hard work to pursue the doctoral degree, but also provided me with invaluable suggestion to my graduate studies even she is not in science major.

TABLE OF CONTENTS

LIST OF TABLES

LIST OF FIGURES

ABSTRACT

The research in this dissertation focuses on the synthesis of size-controlled metal oxide nanoclusters (< 10 nm) on amorphous silica and their catalytic performance in thermal degradation of chlorinated benzenes with regard to the cluster size effect. Furthermore, with the concern that metal can condense as the nano-size nuclei core for particle growth in combustion process, a flow reactor was built to investigate the effect of metal oxide nanoparticles on the formation of soot in fuel-rich combustion.

The synthesis of copper oxide nanoclusters was carried by calcination of silica impregnated with dendrimer-metal complexes. The 4th generation poly(propylene imine) dendrimer DAB-Am$_{32}$ was used in this template-based method. The sizes of copper oxide nanoclusters were exquisitely controlled in the range of 1-5 nm with narrow size distribution by changing the stoichiometric ratio of metal ion to the terminal primary amines of dendrimer, the equivalent metal oxide loading on surface, and the impregnation procedure. XANES and XPS studies revealed that CuO was the dominant component of copper oxide nanoclusters. This method was also experimentally proven to be valid in the preparation of other metal oxide nanoparticles, e.g., Ni and Fe, and with other oxide substrates, e.g., titanium oxide.

Chlorinated benzenes were selected as the model compound for studying the activity of metal (Cu and Fe) oxide catalysts with regard to their cluster sizes. Compared to the surrogate of coarse metal oxide samples, which was prepared by incipient wetness method, their nanosize analogues showed superior catalytic activity on the conversion of chlorinated benzenes under both pyrolytic and oxidative thermal condition. Furthermore, such catalytic size effect was also observed on the selectivity of products yields.

Sooting combustion was performed using a two-zone flow reactor with precise control on experimental parameters. Gas suspended metal oxide nanoparticles were generated by burning off the organic backbone of the dendrimer-metal complexes in zone 1 and immediately transferred to zone 2, where the hydrocarbon combustion occurred. TEM results of the particulate sample collected at the outlet of reactor indicated that metal oxide nanoparticles promoted soot formation. GC/MS analysis of the extracted organic materials from soot samples suggested the formation of PAH was also promoted by metal addition as well.

CHAPTER I: INTRODUCTION

Nanoscale particulate material is a unique substance largely due to their size and properties effectively bridging bulk materials and atomic or molecular structures. With the increasing ability to synthesis and characterize nanoparticles in past decades, more and more scientific and industrial attention has been attracted onto this material because of their greatly potential use in different areas.[1-4] One of the most important applications of metal or metal oxide nanoparticles is catalysis, as the particle size affects not only the reactive activity but also the selectivity of catalysts.[5-9] The appearance of metal oxide nanoparticles in pollutant emission from combustion also raised the concern of their roles in pollutant formation and potential impact to human health.[10-13] However, there is only limited data regarding the nano size effects in these environmental impacts, mostly due to the non-uniform, complex composition of combustion-generated nanoparticles. Furthermore, soot formation has been intensively studied for decades because this type of particulate matter was believed to be the most important environmental sources of PAH.[14] Although some correlation of metal oxide particles and soot formation has been observed,[15-16] there is no direct experimental studies being reported using metal oxide nanoparticles directly for studying the effect of metal on soot formation. With these concerns, reproducible synthesis of nanoparticles with precise control over size and composition is desirable to conduct both above addressed catalysis and environmental studies.

1.1   Occurrence, Application and Risk of Nanoparticles

"Nano" is a prefix in the International System of Units (SI) denoting a factor of 10^{-9}. 1 nanometer (nm) is an extremely small length which is measured to about one 50,000th of the diameter of human hair. Although there is no exact definition of nanoparticles, this type of material is generally referred to as the aggregation of atoms bridging the spectrum between small molecules clusters of a few atoms with dimensions as small as 0.2 to 1 nm to chunks of solid

material containing millions of atoms with properties of macroscopic bulk materials.[17] In many cases,[10, 18-21] nanoparticles are defined as having an aerodynamic diameter smaller than 100 nm, or 10-20 nm in a narrower sense, where the physical properties or reactivity of these materials show difference from their bulk forms. For example, electrical properties such as ferroelectric and dielectric properties have been considered to be intrinsic, independent to the size of the materials. However, when the dimension of the particles decreases to less than several tens of nanometers, it was found that these physical properties of the materials became size-dependent.[22]

Particles in the nanometer regime have existed naturally on the earth for millions of years. They can be found as suspended particles in the air, in rivers or lakes, in the soil, in volcano ash, and even in our bodies. Anthropocentric activities also produce nanoparticles. Soot for instance, a product of the incomplete combustion of fossil or vegetation, may be the earliest nanometer size materials produced by mankind thousands of years ago. The making and use of nanoparticles can be traced as far back as 9th century from the analytical results of historical art pieces, in which nanoparticles were used for generating a glitter effect on the surface of pots [23]. This unique substance has been always considered as an invention of modern science because its use in large scale applications only emerged from late the 20th century.[3] Major routes for making nanoscale particulate materials are summarized as liquid-phase synthesis and gas-phase synthesis with detailed approaches listed in **Table 1.1**. Although the manufacturing techniques of nanoparticles have been developed and improved in the past decade, there are still some challenges presented in its syntheses, including size and shape control, means to achieve monodispersity, reproducibility, scale up, and building complex nanostructures.

Today, nanoparticle research including synthesis, characterization and potential applications has become intense areas of scientific research. This largely due to their potential

Table 1.1 Summaries of nanoparticles synthesis techniques

Category	Detailed Technique
Liquid-phase Synthesis	- Sol-gel processing [24] - Microemulsions [25] - Microwave synthesis [26] - Template synthesis [27] - Biometic synthesis [28] - Coprecipitation [29] - Sonochemical method [30] - Hydrothermal/solvothermal synthesis [31]
Gas-phase Synthesis	**Methods using solid precursors** - Ion Sputtering [32] - Pulsed Laser Ablation [33] - Spark Discharge Generation [34] - Inert Gas Condensation [35] **Methods using liquid or vapor precursors** - Chemical Vapor Synthesis [36] - Spray Pyrolysis [37] - Laser Pyrolysis/ Photochemical Synthesis [38] - Thermal Plasma Synthesis [39] - Flame Synthesis [39] - Flame Spray Pyrolysis [40] - Low-Temperature Reactive Synthesis [41]

applications in areas, such as catalytic,[6-7, 13, 42] electronic,[43] cosmetic,[4] energy,[44] environmental,[45] biomedical,[1] and materials fields.[46] Some examples of these emerging applications include, development of high-performance solid oxide fuel cells using Ni-YSZ nanoparticulate composite,[47] drug delivery to the brain with biodegradable polymeric nanoparticles,[48] making smart materials with tunable structural color based on closely packed monodispersed silica nanoparticles assembly,[49] enhancement of the performance of insulating materials using nanosize SiO_2,[50] etc. Supported metal/metal oxide are typically used as industrial catalyst.[51] The

3

development of the nanoscale analogue is of great interest because the chemical catalytic properties of transition metal exhibit unusual activity and selectivity in the nanometer regime.

The appearance of nanotechnology in our life also has increased concern on the health impact caused by the exposure to nanoscale particulate matter (PM). PM has been defined as one of the six common pollutants by EPA since 1971 and the regulation of PM_{10} (coarse particles, < 10 µm) and $PM_{2.5}$ (fine particles, < 2.5 µm) were legislated in 1987 and in 1997, respectively.[52] Only recently the ultrafine fraction ($PM_{0.1}$ or particles size < 100 nm) were considered as the likely source (along or in combination with other pollutants) of a majority of PM associated illnesses or death.[53] The paucity of studies on $PM_{0.1}$ and lack of regulation by EPA are largely due to the extremely small size of the ultrafine fraction which makes capture by air pollution control devices (APCD) difficult and inefficient. Compared to larger size PM, ultrafine particles can be transported over longer distance and penetrate deeper into the human respiratory system, which increase the potential risk on human health.[54-57]

The majority of ultrafine PM is formed by combustion and emerged as primary or secondary particles. The primary fraction is directly released into atmosphere by combustion processes. The secondary component is formed by atmospheric chemical reaction of other combustion emitting gaseous pollutants, particularly volatile organic compounds such as sulfur oxide and nitrogen oxides.[10, 58] The chart shown in **Figure 1.1** was based on the 1996 emissions inventory for the south Coast Air Basin of California, which indicated the largest sources of $PM_{0.1}$ were on-road motor vehicles and stationary source fuel combustion.[59]

Numerous research studies have demonstrated that fuel combustion generated nanoparticles with diameters from a few to several hundred nanometers contain potentially catalytic metals, organic species, "elemental carbon", and minerals.[15, 56, 60] It is widely accepted that relatively non-volatile species vaporized in high temperature flame zone form significant

4

amount of fine and ultrafine PM through condensation in the post flame region.[15, 60-61] In addition, the Kelvin Effect (reducing the vapor pressure of species on surface) was also considered to be the driving force of particle growth in post flame zone.[61] As a result, the presence of seed nuclei is necessary for more volatile species to condense into particles. Metals, usually in the forms of sulfate, oxide or chloride species, have been found to play a more active role than any of the other seed candidates.[62]
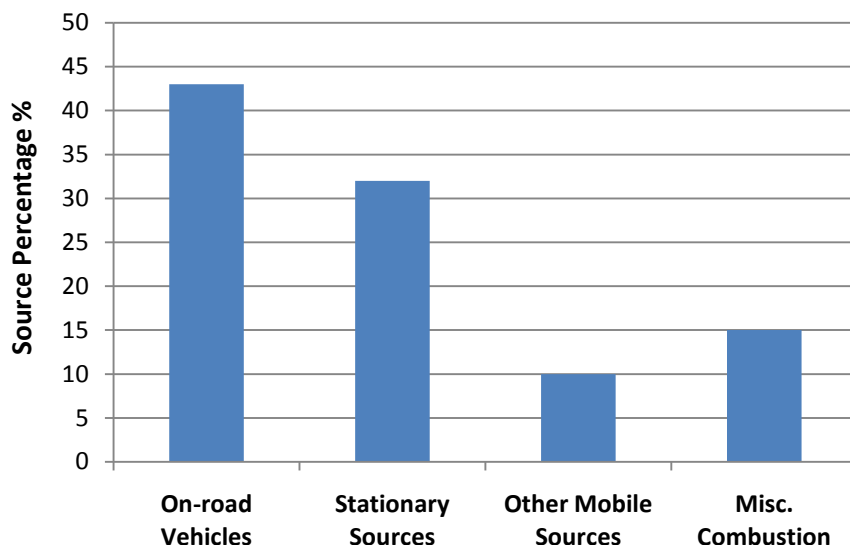
Figure 1.1 Emission inventory of combustion-generated ultrafine particles for the South Coast Air Basin (1996) (adapted from ref. 59)

Transition metals present in combustion-generated particulate matter are catalytically active in the reactions with organic species in the combustion and post combustion zones. For example, redox active metal, such as Fe and Cu in the form of supported metal oxide compound, has been suggested to promote the formation of dioxins via surface-mediated reactions at temperature range from 200 to 600 °C.[63-66] The terms of dioxins commonly refers to a class of highly toxic chemical pollutants, polychlorinated dibenzo-*p*-dioxin (PCDDs) and polychlorinated dibenzofurans (PCDFs). PCDD/Fs have been the subject of intense research through many years

due to their extreme toxicity to humans, including cancer, damage to immune system, birth defects, and other severe reproductive and development problems.[67-69]

1.2   Size Effect of Metal Oxide Nanocatalysis

From the viewpoint of chemists, the most valuable properties of nanoclusters is the size effect shown in reactivity, which can be the key answer to develop new catalysts with higher activity and better selectivity. The strong correlation between the reaction energies and the size of platinum nanoclusters based on theoretical calculation was reported.[70]   This was also confirmed by the experimental studies of CO and NO oxidation. Polymer-stabilized Au nanoclusters showed an increase in catalytic activity per unit cluster surface area with decreasing size when dispersed in water for aerobic oxidation of alcohol.[8] However, the decrease of particle size does not necessary result in higher catalytic activity. Iglesia has reported that too small clusters of metallic cobalt are inactive in Fisher-Tropsch synthesis, contrary to larger crystallites.[71]   Additionally, a recent research work regarding the hydrogenation of nitrate in water using Pd-Cu/TiO_2 catalysts indicated that the selectivity of products is largely depended on the size of active phase (catalyst) with critical value of about 3.5 nm, below which NO_2^- becomes the dominant product rather than nitrogen.[9] In industrial application, the capability to predict desired products by selective catalysts is very valuable for the enhancement of production efficiency and cost reduction.

The size effects of nanoclusters on catalytic properties have been attributed to many factors but generally limited into two aspects: the increase in the ratio of surface to volume, and the domination of quantum effects when the electrons in a nanoparticle are limited to a space of only a few atom-widths across.[72]

With the increase of surface-to-volume ratio, which is in reversed proportion to the size of particles, the ratio of atoms exposed on the surface to the total number of atoms of a particle

also increases. In heterogeneous catalysis, surface atoms of the catalyst play a great role since they are easier to be accessed or bonded than those inside the particles. For larger particulate matter with size of micron or submicron scale, the percentage of surface atoms does not significantly increase with the decrease of particle size, which is corresponded to the limited deviation of the properties from bulk form. However, when the particle size is small enough, e.g. several nanometers, the dependence of the material's properties on size becomes significant and non-scalable. For example, the number of atoms packed in a 1nm size particle only has the order of hundreds or thousands and most of the atoms are either directly exposed on the surface or in the sub-surface layer. In that case, the physical and chemical properties are strongly affected by the nature of atoms or molecules of the material itself, which can no longer be deduced or extrapolated from those known for larger sizes. **Table 1.2** shows the relationship between particle size and the fraction of surface atom which is based on the inter-atomic distance of 0.25 nm.[73]

Table 1.2 Particle size[*] and the fraction of atoms located at the particle surface

Number of atoms in a side	Number of atoms at the surface	Total number of atoms in particle	Number ratio surface atoms to the total (%)	Theoretical particles size (nm)
2	8	8	100	0.5
4	56	64	87.5	1
6	152	256	59.3	1.5
10	488	1000	48.8	2.5
100	58800	1×10^6	5.9	25
1000	6×10^6	1×10^9	0.6	250
10000	6×10^8	1×10^{12}	0.06	2.5 um
100000	6×10^{10}	1×10^{15}	0.006	25 um

 * Assuming all the particles are in cube shape.

Furthermore, when particles are small enough, electrons will be confined to a space only a few atoms across and the quantum effect becomes dominant. In that case the free electrons in nanoparticles behave similarly to those bound by atoms and can only occupy specific energy

states. The whole nanoparticle can be viewed as a "single atom" with discontinuous energy change. This quantum effect has been demonstrated in the study of electronic magnetic susceptibility using various sized Pd nanoparticles,[74] where the smallest clusters were tested and exhibited more electronic magnetic susceptibility when compared to larger clusters.

Although a large amount of research regarding nanoclusters have been conducted in different scientific areas, much less study has been focused on the transition metal oxide nanoclusters, primarily due to the lack of synthetic methods to produce monodispersed supported clusters in nanoscale. While there has been progress in the preparation of a variety of metal-oxide nanoparticles in recent years, a major obstacle to their widespread use is precise control of the particle size (selectivity) and size dispersity (control).[75-76] These issues are of particular concern for supported metal oxide nanoparticles, which is one of important types of catalysts used in industrial applications. Different from single-crystal surface model, the reactivity of supported nano catalyst is strongly related to particle agglomeration, size, and size dispersity.[70, 77-79] Significant progress has been made in the synthesis of metal nanoparticles by application of template-based methods that utilize precursors composed of metal ion-containers, e.g. dendrimers, micelles, and organometallic complexes.[38, 73, 80-88] Application of these template-based methods and other approaches to the synthesis of metal oxide nanoparticles has resulted in a group of studies that targets the fabrication of metal oxide nanoparticles of controlled size. For example, various sizes of nanocrystalline Fe_3O_4 from 5.7 to 16.8 nm was synthesized by thermal calcination of the precursor of chelate iron alkoxide complexes in solutions of corresponding alcohol, diethylene glycol, and N-methyl diethanolamine.[89] It has been reported the hydrolytic decomposition of platinum chloride resulted in the formation of water-soluble PtO_2 nanoparticles with size varying from ~1 to 50 nm depending on the PH value.[87] Using dendrimer as stabilizer, water-soluble iron oxide nanoparticles were produced with size in range from 20 to 30 nm,

8

which indicated aggregation in solution.[90]   However, results of these studies indicate that the made-to-order synthesis of metal oxide nanoparticles of controlled size and distribution still has significant limitations, thus, the development of fabricating a wide variety of well-defined nanoparticles is of great importance.

1.3   Dendrimer and Its Applications in Nanofabrication

1.3.1   Background of Dendrimer

Dendrimers are spheroid or globular macromolecules with regular, highly branched structure and surface functionality. The first example of these hyper-branched materials with thoroughly investigation was reported in the early 1980's by Donald Tomalia et al. and named as **dendrimer**, which originated from "dendron" (tree) in Greek.[91]   Different from traditional polymers, dendrimer has a unique core-shell structure which consists three basic architectural components: (1) a core, (2) an interior of shells constructed with repeating branch units, and (3) terminal functional groups (periphery or outer shell).[92] Dendrimers are synthesized through a set of iterative chemical reaction steps that build up from the molecular level to the nanoscale region under easy maintained conditions in an organic chemistry laboratory. Each additional iteration forms a new "generation" with double terminal groups and approximately twice the molecular weight of the previous generation. Meanwhile, the diameters of higher generation dendrimers also increase linearly from 1 to over 10 nm due to the geometrically increasing number of surface atoms.[92-94]

Dendrimers are generally prepared by two conceptually different hierarchical assemblies: divergent approach and convergent approach.[95] **Figure 1.2** presents the schematic strategies of the two approaches. In the divergent method, a dendrimer molecule is constructed outward from a central core toward peripheries in a stepwise growth. For each shell (generation) addition cycle, the number of coupling reactions between monomers and end groups increases exponentially. In

contrast, the convergent approach starts from peripheries toward the central core. In this method, different generations of dendrons (dendrimer branches) are pre-synthesized and attached to the same central core to give different generations of dendrimers. Though the synthesis of dendrimers involve many repeated reactions which usually lead to high cost production, in most case the reactants for synthesis are normally cheap and the iterative chemical reaction is straightforward. Consequently, the manufacture of dendrimers can be an economic process, which implies the possibility of large scale application. Today, the commercial production of two families of dendrimer poly(amido amine) (PAMAM) and poly(propylene imine) (PPI) dendrimers, which both are synthesized using the divergent approach, has greatly increased interest in the applications of these unique materials [92]. For example, dendrimers are used on pharmaceutics as coating agents to protect and deliver drug to specific sites in the body. In biomedical and preclinical studies, dendrimers are used as contrast agents for magnetic resonance. In catalysis and in environmental field, dendrimers can be used as molecule capturers for those insoluble materials, e.g. toxic metals.[38, 86, 96-99]
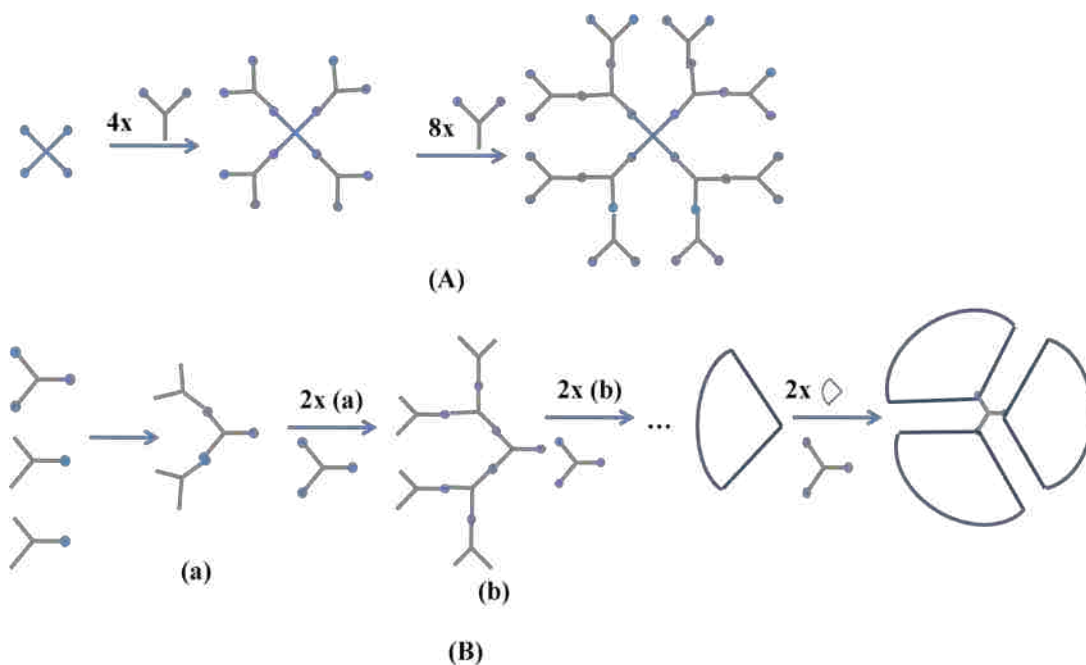
Figure 1.2 Synthesis routes of dendrimer (A) divergent (B) convergent (adapted from ref. [95])

1.3.2   Synthesis of Metal Oxide Nanoparticles Using Dendrimer Template

Among the potential applications for dendrimers, catalysis is of particular interest in nanoscience as dendrimeric template offers a reliable, flexible and reproducible method of generating metals/metal oxides nanoparticles with controlled size (typically < 10 nm), shape and composition.   Research of catalytic reactions involving these dendrimer-metal complex compounds include hydroformylation,[100] olefin metathesis,[101] Heck reactions,[102] hydrogenations and alkylation and Suzuki coupling.[103]   In many cases they are based on the fact that dendrimer molecules can coordinate or complex various metal ions at the periphery, interior or throughout all layers of the dendrimer "host" in a controlled manner.

The number of active sites of the heterogeneous catalysts is one of the important factors to their activity.   Since most of these active sites are presented on the surface, smaller particles naturally have more active sites due to their high surface-to-volume ratio.   However, small nanoparticles always have a tendency to aggregate due to their high total surface energy.   To avoid this undesired effect in commercial metal oxide catalysts, metal/metal oxide particles are dispersed on separation media, which typically is a high surface inorganic oxide material [104-105]. In traditional catalyst preparation methods such as incipient wetness, metal salts are impregnated onto the high surface areas and are subjected to subsequent thermal treatments.   However, depending on the nature of the solid support, nanoparticles prepared by this traditional route may have different mobility during the thermal process.   These processes vary widely for different metals and substrate and remain poorly understood.   Therefore there is only limited control over the size of nanoparticles and thus their catalytic properties when using these traditional preparation procedures.[106]   To address this issue, it is desirable to limit the mobility of metal clusters on the surface by adding some metallophilic absorbate to the metal precursor solution prior their deposition on surface.   Dendrimer is one of such absorbate due to its extraordinary

properties, including complexation with metal ions in a control manner and easy deposition onto solid surface.[5,107] In homogeneous catalyst synthesis, the presence of dendrimers can protect encapsulated metal nanoparticles from aggregation in solution. In heterogeneous catalyst synthesis, dendrimers are employed as metal template and stabilizer for retaining metal nanoparticles in situ on the surface. **Figure 1.3** illustrates the proposal schematic for making metal oxide nanoparticles using dendrimer template techniques, compared to the traditional incipient wetness method.
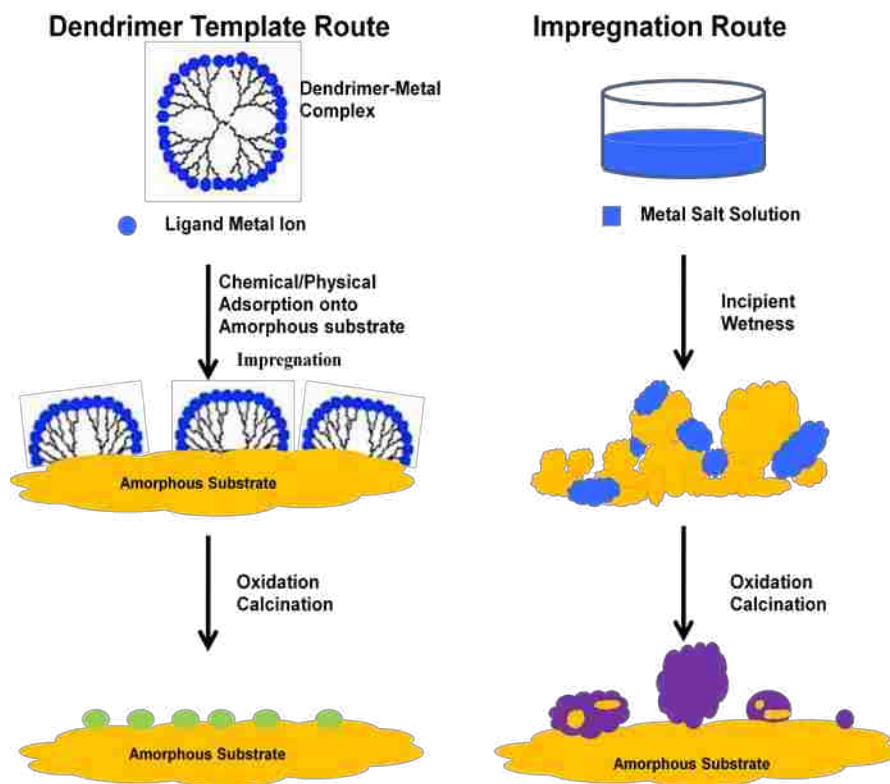
Figure 1.3 Comparison of supported metal oxide catalysts made by dendrimer template method and traditional incipient wetness method

Although synthesis of supported metal nanoparticles via the dendrimer template route has been reported in numerous research studies; most of them focus on the encapsulated metal particles synthesized by reduction pathway, which leaves the carbonaceous materials of the dendrimer template intact.[38, 73, 97, 108] It has been suggested that the presence of dendrimer frame

will not affect the catalytic properties of the inside metal particles significantly. However in most cases, uncoated metal oxide particulate matrix is necessary so that the presence of dendrimeric back-bone is avoided. For example, dendrimer-encapsulate metal particles supported on solid substrate showed no catalytic activity to bind CO, as the dendrimer collapsed on nanoparticles and poisoned the metal surface.[109-110]

1.4   Soot Formation from Combustion

1.4.1   Definition of Soot

Although there is no exact definition of soot, it is often referred to the solid carbonaceous particles resulting from the incomplete combustion of fossil fuels and biomass. Though the size, shape, composition of soot are widely varied depending on the combustion condition, such as type of combustor, residence time, temperature and fuel/oxygen ratio, there are some common features of this type of particulate matter. In general, soot particles are emitted in cluster-like or chain-like aggregates of near-spherical primary particles. Single soot particles are varied from 20 to 50 nm in diameter.[111-112] These particles consist mainly of carbon and hydrogen with varied C/H ratios ranging from about 1 for young soot to greater than 10 for well developed particles.[113-114] The increase of C/H ratio for the latter is a result of the graphitization of soot particles.[115] Other chemical species incorporated into soot include inorganic salts and metals obtained from burned out fuel impurities.[15]

1.4.2   Risks and Applications of Soot

Soot has long been recognized as one of the most hazardous pollutants to human health due to its breathable size and toxicity.[116] Generated and released by combustion sources, soot is one of the most representative kinds of airborne particulate matter. Combustion generated soot particles are categorized as fine and ultrafine particulate matter. Due to their extremely small dimension, soot particles can penetrate deep into the human respiratory system and cause severe

health risks upon inhalation. Furthermore, due to the nucleation effect, polycyclic aromatic hydrocarbons (PAHs) are frequently found in soot particles,[115, 117] which add to the toxicity of soot. Many PAHs are known for their toxicity as human carcinogen and mutagens.[118-120] The International Agency for Research on Cancer (IARC) has classified PAHs as a "known human carcinogen" since 1985.[121] As the current global soot production is estimated to be~50-200 x 10^{12} g/yr,[122] it is believed that soot is probably the most important source of PAHs in the environment.

In addition to their impact on human health, soot formation is also undesirable in many practical circumstances. For example, black carbon in soot can absorb visible solar radiation, leading to climate change.[14] As airborne soot can travel long distance for weeks, settling on glaciers in the Polar Regions accelerates the melting of ice, and raises the sea level. It is estimated that the emission of soot accounts 18% of global warming, the second strongest contributor after carbon dioxide emission.[123] Fouling problem in combustion system is another deleterious effect caused by soot deposit. During the operation of engines, the presence of soot can increase the radiating power of the flame and the heat transfer rate, leading to worn-out of engines and low efficient utilization of fossil energy.[124]

Soot formation can also be advantage. Carbon black (soot) collected from candle or lamps using animal fats had been used to make pigment or ink for centuries. It was reported recently that diesel soot can be recycled efficiently and used as a precursor for synthesis of single-wall carbon nanotubes.[125] Today black soot (technical carbon) is commercially produced at an estimated yield of 10^7 tons per year globally.[126] Their applications include filler for elastomers, printing ink for copy machine and laser printers, etc.

1.4.3 Homogeneous Soot Formation

With the above concerns, it is very desirable to gain control over the formation and emission of combustion generated soot particulate matter. This requires a better physical and chemical understanding of the combustion process. Over the past three decades, significant research effort on soot formation has been undertaken using different experimental setup, including flames, shock wave tubes, and flow reactors with the usage of different hydrocarbons (e.g. acetylene, benzene, methylnaphthalene, etc.) and diesel fuel as soot precursors.[127,128,129-137] Although soot formation is a complex phenomenon and the detailed mechanism remains poorly understood, it is widely accepted that this process can be broken down into general stages: (1) formation of gaseous precursors of soot, (2) inception of particles, (3) mass growth of particles through reaction with the gas-phase species, (4) coalescent and coagulation to particle growth, (5) carbonization of particulate matter, (6) oxidation of PAHs and soot particles.[112, 117] A proposed route for soot formation is shown in **Figure 1.4** and more details of these stages are summarized below.

The formation of molecular precursors is the first critical step in the soot formation process. In the initial stage of combustion, fuel molecules are decomposed through high temperature reaction. In an oxygen rich (carbon/oxygen ratio < 1) condition, most fuel molecules are completely oxidized and converted into CO, CO_2, and H_2O. With the decrease of oxygen feed, the fuel rich condition (carbon/oxygen ratio > 1) exists and pure or oxidative pyrolysis becomes dominant. Regardless of the initial types of fuel that are used, the fuel molecules initially degrade into small hydrocarbon radicals, and then break down into smaller unsaturated fragments, particularly acetylene (C_2H_2), due to the incomplete combustion. These small hydrocarbon species react to form large hydrocarbon molecules such as polycyclic

aromatic hydrocarbons (PAHs) and polyynes ($C_{2n}H_2$, n=2, 3...), which both are commonly considered as molecular precursors of soot.[127, 138]
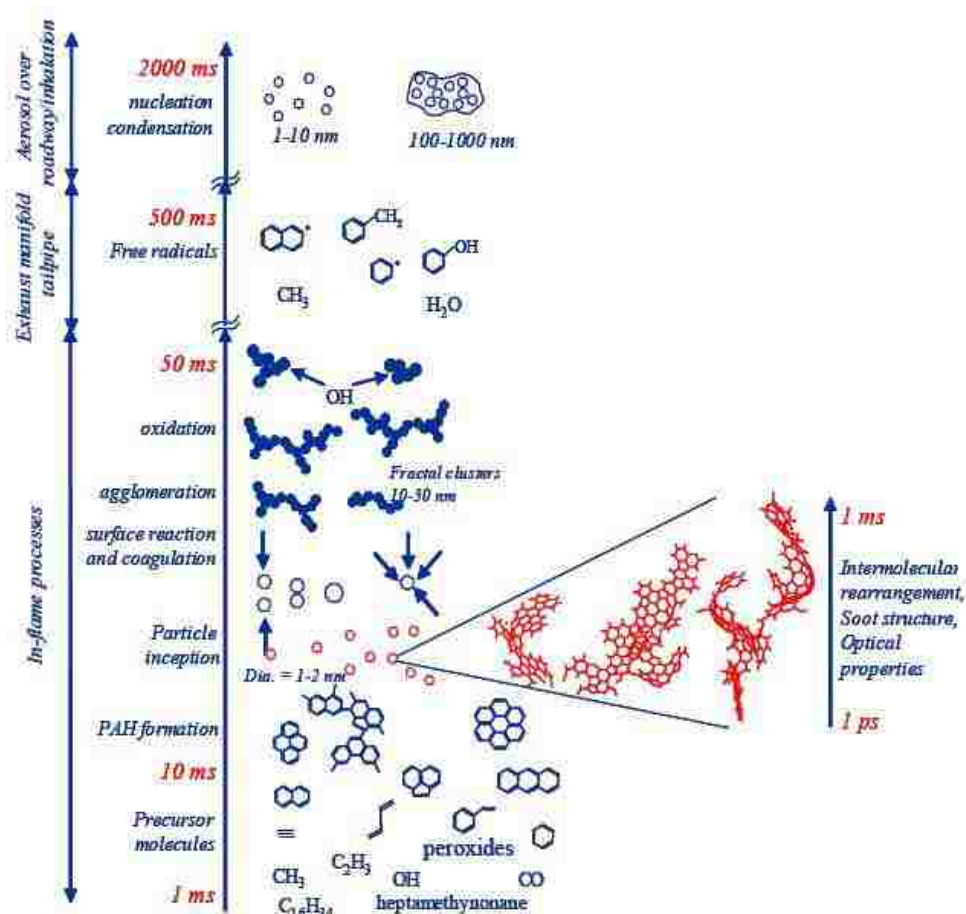
Figure 1.4 Schematic Soot Formation Process (adapted from ref. [139])

The second step of soot formation is particle inception, which involves conversion from gaseous molecular compound to particles. For example, heavy PAH molecules form nascent soot particles with the smallest detectable diameter of 1.5 nm, corresponding to a molecular weight about 2000 amu.[124] To understand this nucleation mode growth from molecule to particle, several competing theories starting from different types of precursor have been purposed in past years. One of the widely accepted pathways is the PAH model, which assumes that particle inception is a continuous molecular growth process due to the collision and coalescence in between PAH species.[140] Another popular hypothesis is the polyyne model, in

16

which every radical capable of forming polyyne complexes is assumed to be the center of a fast polymerization center, with the presence of "super-saturated polyynes vapor".[141]

Growth of the nascent soot particles progresses through the addition of gas phase species, such as acetylene and PAH. Radical sites on soot particles are believed to be involved in the stabilization of the molecular reactants. Although there is no significant change to the particles number in this surface growth step, the mass of soot significantly increases. This growth process can occur at temperature below the lower limit required for soot inception path.[142] A mechanistic explanation introduced by Freenklach treats the surface growth reactions similar to the planar growth of PAHs [143]. In this approach the surface of a young soot particle is assumed to be like giant PAH molecule that has abundance of C-H bonds. Applying the hydrogen-abstraction/carbon-addition (HACA) soot growth mechanism into this heterogeneous surface reaction, the abstraction of H on the atoms leads to the formation of surface radicals, which subsequently react with incoming gaseous molecules and promote the growth of particles.[142]

Mass growth via molecules forms particles of several nanometers in diameter. However, most soot particles are as large as tens to hundreds of nanometers, due to the agglomerating form of the primary particles. This growth process, correlating to the decrease of particle number without changing total mass of soot, is the result of the sticking collisions between already-formed particles, which occur immediately after particle inception, or when small/young soot particles form.[138] Coalescence makes it difficult to identify primary soot particulate units in electron microscopy. If particles collide and stick to each other without fusion, the resulting chain-like or cluster-like agglomeration retains the individual identification of the primary particles.

The observed soot formation is a combined result of the soot growth, carbonization, pyrolysis and oxidation (which decrease mass). Carbonization of soot particles typically occurs

in the late stages of soot formation, due to the long residence time and the pyrolytic condition of high temperature post-flame zone. In this process, the polyaromatic materials presented in the soot particles undergo functional group elimination, cyclization, ring condensation and fusion. This is accompanied by dehydrogenation, growth and alignment of polyaromatic layers, which convert the initial amorphous soot material into a progressively more graphitic material.[117] Depending on the combustion conditions, pyrolysis and oxidation may cause a significant mass loss of soot in comparison to the surface growth.

1.4.4 Effects of Metal on Soot Formation

In addition to the pathway of homogeneous nucleation and molecular growth of soot formation that has been widely accepted and studied, more and more recent research indicated the heterogeneous mode growth through the surface condensation on an already formed particle competes to the homogeneous mode growth of soot. Although semivolatile compositions, such as heavy hydrocarbons, sulfuric acid, dominates the particulate emission of fuel combustion, solid nuclei particles are commonly found as result of vaporization of relative non-volatile species in the high temperature flame zone, e.g. combustion of heavy oils, incineration of industrial waste streams. Typical solid compositions include suboxides of silica and alumina, common metals such as Fe, Zn, Ni, V and Cu, and some high-molecular weight organics. It has been reported that the metal content in PM from combustion of heavy fuel oils shows a strong dependence to the particle size. As particle size fell into the submicron range, the concentration of transition metals (Zn, Ni, and Fe) increased exponentially to over 60% and the carbon concentration decreased from nearly 90% to less than 30%. Another study of particle formation from combustion of #5 and #6 fuel oils also supported this finding. It was found that 80% of the nanometer particle fraction consisted of the transition metals, including Cu-, V-, Zn-, and Ni-sulfates. This data suggests that solid composition, with sizes of less than 10 nm and composed

of metal/metal oxide/metal sulfate, is not simply an inert substrate for condensation of organics, but is a reactive metal nanoparticle that promotes molecular growth reactions and thus particle growth.

Metal-based fuel additives have been greatly used for control and suppression of soot formation. Numerous studies concerning the effects of metal additives on soot suppression have been conducted in practical and laboratory-scale combustion system. For example, when alkali or alkaline earth metals were added to a premixed flame, significant reduction in the soot volume fraction were observed.[144] Some other research has found that iron, as well as manganese and barium, are the most effective soot-reducing fuel additives. Dicyclopentadiene iron ($Fe(C_5H_5)_2$), or ferrocene, are widely used in different combustion system,[145] because of their solubility in liquid fuels, air stability, innocuity and unusual thermal stability.[146] However, mixed results have been reported. Retrievi et al. observed that ferrocene-doped premixed flame produced more soot than undoped premixed flame.[147] As homogeneous nucleation of iron to iron oxide nanoparticles occurs prior to soot inception, these already formed particulate sites ease the nucleation of hydrocarbon and hence promote soot formation. Meanwhile, metal oxide incorporated into the soot matrix may act as a catalyst to promote soot burnout in oxygen-rich regions of the combustion system, which is seen as soot-suppression.[148]

Many details of these complex interactions between metal and hydrocarbon remain unclear. Therefore, the study for understanding the effects of metal on soot formation can significantly contribute to the control of soot emission and their impact to human health.

1.5   Research Objectives

The studies reported here can be divided into three projects. The first involves the synthesis and characterization of size-controlled metal oxide nanoparticles supported on substrate using dendrimeric template technique. The second concerns the catalytic application of

supported metal oxide nanoclusters, focusing on the cluster size-associated activity and selectivity in reaction. in the comparison with those of coarse particles which were prepared by incipient wetness impregnation method. Finally, dendrimeric technique is used to produce gaseous suspended metal oxide nanoparticles for the study of metal mediated soot formation, using a two-zone high temperature flow reactor.

The synthesis of dendrimer-encapsulated metal and semiconductor nanoparticles in aqueous phase or organic solvent had been reported.[38, 73, 97, 108, 149-150] However, there is very limited research considering the application of dendrimeric template technique for the synthesis of monodispersed metal oxide nanoclusters on support, which is of particular interest to the practical catalysis in industry. In the first project, supported size-selective metal oxide nanoparticles were synthesized through a modified dendrimeric template technique, based on the fact that dendrimer can complex metal ions in a controllable stoichiometric or sub-stoichiometric ratio.[73, 151] Various dendrimer-metal complexes were used as the metallic precursors for this synthesis. The approaches of tuning the size of metal oxide nanoclusters were performed via changing the substitution ratio of dendrimer in precursor, the concentration of dendrimer-metal complexes on substrate surface, the preparation procedure and the calcination temperature. This method was tested on matrixes using different metallic precursors (Cu, Ni, and Fe) and substrates (SiO_2 and TiO_2).

One of the biggest motivations to develop nanocatalyst is their surprising activity and selectivity in reactions. It is well known that smaller particles are correlated to higher surface/volume ratios and thus more active sites in the unit mass. However, when particle size decreases into the 1-10 nm regime, the surface atomic ratio becomes significant and quantum effect becomes dominant, the change of their reaction activity is not measurable because of the small size [42]. Furthermore, selective products may form as the result of the extremely small size

of particles. In order to better understand the size effect on reaction, a comparison study regarding the thermal degradation of chlorinated benzenes over supported copper/iron oxide nanoclusters and impregnated coarse particles was performed in the second project. Chlorinated benzenes were chosen as the gas phase precursor due to their abundance in the waste combustion source and the potential role lead to PCDD/Fs formation.[152]

In the last project, a custom-built two-zone high temperature flow reactor was used to investigate the effect of metal oxide nanoparticles on soot formation. Though numerous studies regarding the influence of the metal additive on the soot growth and inhibition have been reported, in most cases metal was mixed with fuel prior to the combustion process.[144-145] In the study reported here, the dendrimer-template technique was used to generate 1-3 nm metal oxide nanoparticles suspended in gas flow. 1-methylnaphthalene was used as the hydrocarbon fuel to produce soot. To investigate the influence of metal on soot formation, experiments of hydrocarbon combustion were performed with or without the introduction of synthetic metal oxide nanoparticles by carrier gas. The use of flow reactor ensures that the combustion condition can be accurately controlled, including residence time, combustion temperature, amount of reactants, and the gas supply.

In summary, the objectives of this dissertation have been to develop a new technique based on a dendrimer template to control the size of supported oxide nanoclusters, which contribute to the study of size effect in nanocatalysis. As combustion generated nanoparticles have been identified as the potential primary health impact caused by particulate matter, this catalytic study will contribute to the understanding of their reactivity in comparison to fine particulate matter. Furthermore, dendrimer-metal complex were used for generation of suspended metal oxide nanoparticles in soot formation. With the careful design of each project,

these studies provide the information for a better and thorough understanding of the chemical behavior of metal oxide nanoparticles in the pollutants.

1.6   References

1.   Gelperina, S.; Kisich, K.; Iseman, M. D.; Heifets, L., The potential advantages of nanoparticle drug delivery systems in chemotherapy of tuberculosis. *American Journal of Respiratory and Critical Care Medicine* 2005, 172, (12), 1487-1490.

2.   Haruta, M., Nanoparticles Can Open a New World of Heterogeneous Catalysis. *Journal of Nanoparticle Research* 2003, 5, (1-2), 3-4.

3.   Schmid, G.; Baumle, M.; Geerkens, M.; Helm, I.; Osemann, C.; Sawitowski, T., Current and future applications of nanoclusters. *Chemical Society Reviews* 1999, 28, (3), 179-185.

4.   Wissing, S. A.; Muller, R. H., Cosmetic applications for solid lipid nanoparticles (SLN). *International Journal of Pharmaceutics* 2003, 254, (1), 65-68.

5.   Ott, L. S.; Finke, R. G., Transition-metal nanocluster stabilization for catalysis: A critical review of ranking methods and putative stabilizers. *Coordination Chemistry Reviews* 2007, 251, (9-10), 1075-1100.

6.   Bell, A. T., The impact of nanoscience on heterogeneous catalysis. *Science* 2003, 299, (5613), 1688-1691.

7.   Yan, N.; Zhao, C.; Luo, C.; Dyson, P. J.; Liu, H. C.; Kou, Y., One-step conversion of cellobiose to C-6-alcohols using a ruthenium nanocluster catalyst. *Journal of the American Chemical Society* 2006, 128, (27), 8714-8715.

8.   Tsunoyama, H.; Sakurai, H.; Tsukuda, T., Size effect on the catalysis of gold clusters dispersed in water for aerobic oxidation of alcohol. *Chemical Physics Letters* 2006, 429, (4-6), 528-532.

9.   Gao, S. K.; Zhang, Y.; Meng, J. W.; Shu, J. A., Real-time analysis of soot emissions from bituminous coal pyrolysis and combustion with a vacuum ultraviolet photoionization aerosol time-of-flight mass spectrometer. *Science of the Total Environment* 2009, 407, (3), 1193-1199.

10.   Donaldson, K.; Li, X. Y.; Macnee, W., Ultrafine (nanometre) particle mediated lung injury. *Journal of Aerosol Science* 1998, 29, (5-6), 553-560.

11.   Cormier, S. A.; Lomnicki, S.; Backes, W.; Dellinger, B., Origin and health impacts of emissions of toxic by-products and fine particles from combustion and thermal treatment of hazardous wastes and materials. *Environmental Health Perspectives* 2006, 114, (6), 810-817.

12.   George D. Thurston, S. D., Ph.D.; NYU School of Medicine; John J. Godleski, M. H. M. S.,   Long-term Exposure to Particulate Matter and Risk of Death from Heart Disease. 2003.

13.   Hirano, S.; Nitta, H.; Moriguchi, Y.; Kobayashi, S.; Kondo, Y.; Tanabe, K.; Kobayashi, T.; Wakamatsu, S.; Morita, M.; Yamazaki, S., Nanoparticles in emissions and atmospheric environment: Now and future. *Journal of Nanoparticle Research* 2003, 5, (3-4), 311-321.

14.   Ramanathan, V.; Carmichael, G., Global and regional climate changes due to black carbon. *Nature Geoscience* 2008, 1, (4), 221-227.

15.   Allouis, C.; Beretta, F.; D'Alessio, A., Structure of inorganic and carbonaceous particles emitted from heavy oil combustion. *Chemosphere* 2003, 51, (10), 1091-1096.

16.   Feitelberg, A. S.; Longwell, J. P.; Sarofim, A. F., Metal Enhanced Soot and Pah Formation. *Combustion and Flame* 1993, 92, (3), 241-253.

17.   Navrotsky, A., *Environmental Nanoparticles* Taylor Francis Inc.: London, United Kingdom, 2004; Vol. 4.

18.   Paur, H. R.; Baumann, W.; Matzing, H.; Seifert, H., Formation of nanoparticles in flames; measurement by particle mass spectrometry and numerical simulation. *Nanotechnology* 2005, 16, (7), S354-S361.

19.   Fenger, J., Air pollution in the last 50 years - From local to global. *Atmospheric Environment* 2009, 43, (1), 13-22.

20.   Zhang, W. X., Nanoscale iron particles for environmental remediation: An overview. *Journal of Nanoparticle Research* 2003, 5, (3-4), 323-332.

21.   Limbach, L. K.; Wick, P.; Manser, P.; Grass, R. N.; Bruinink, A.; Stark, W. J., Exposure of engineered nanoparticles to human lung epithelial cells: Influence of chemical composition and catalytic activity on oxidative stress. *Environmental Science & Technology* 2007, 41, (11), 4158-4163.

22.   Hoshina, T.; Yasuno, H.; Kakemoto, H.; Tsurumi, T.; Wada, S., Particle size and temperature dependence of THz-region dielectric properties for BaTiO3 nanoparticles. *Ferroelectrics* 2007, 353, 55-62.

23.   del Rio, A. P.; Castaing, J.; Aucouturier, M., Metallic nano-particles in lustre glazed ceramics from the 15th century in Seville studied by PIXE and RBS. *Nuclear Instruments & Methods in Physics Research Section B-Beam Interactions with Materials and Atoms* 2006, 249, 596-600.

24.   Ennas, G.; Musinu, A.; Piccaluga, G.; Zedda, D.; Gatteschi, D.; Sangregorio, C.; Stanger, J. L.; Concas, G.; Spano, G., Characterization of iron oxide nanoparticles in an Fe2O3-SiO2 composite prepared by a sol-gel method. *Chemistry of Materials* 1998, 10, (2), 495-502.

25.   Wang, C. C.; Chen, D. H.; Huang, T. C., Synthesis of palladium nanoparticles in water-in-oil microemulsions. *Colloids and Surfaces a-Physicochemical and Engineering Aspects* 2001, 189, (1-3), 145-154.

26.   Liao, X. H.; Zhu, J. J.; Zhong, W.; Chen, H. Y., Synthesis of amorphous Fe2O3 nanoparticles by microwave irradiation. *Materials Letters* 2001, 50, (5-6), 341-346.

27.   Berger, A.; Gebbink, R. J. M. K.; Koten, G. v., Transition Metal Dendrimer Catalysts. In *Topic of Organometallic Chemistry*, Springer-Verlag: Berlin, 2006.

28.   Sewell, S.; Wright, D. W., Biomimetic synthesis of metal oxide nanoparticles utilizing PAMAM and PPI dendrimers. *Abstracts of Papers of the American Chemical Society* 2006, 231, -.

29.   Xu, X. H.; Zhou, H. Y.; He, P.; Wang, D. H., Catalytic dechlorination kinetics of p-dichlorobenzene over Pd/Fe catalysts. *Chemosphere* 2005, 58, (8), 1135-1140.

30.   Xie, R. G.; Li, D. S.; Yang, D. R.; Jiang, M. H., Surface synthesis of PbS nanoparticles on silica spheres by a sonochemical approach. *Journal of Materials Science* 2007, 42, (4), 1376-1380.

31.   Vazquez-Vazquez, C.; Lopez-Quintela, M. A., Solvothermal synthesis and characterisation of La(1-x)A(x)MnO(3) nanoparticles. *Journal of Solid State Chemistry* 2006, 179, (10), 3229-3237.

32.   Chung, C. K.; Wu, B. H., Thermally induced formation of SiC nanoparticles from Si/C/Si multilayers deposited by ultra-high-vacuum ion beam sputtering. *Nanotechnology* 2006, 17, (13), 3129-3133.

33.   Quintana, M.; Haro-Poniatowski, E.; Morales, J.; Batina, N., Synthesis of selenium nanoparticles by pulsed laser ablation. *Applied Surface Science* 2002, 195, (1-4), 175-186.

34.   Messing, M. E.; Dick, K. A.; Wallenberg, L. R.; Deppert, K., Generation of size-selected gold nanoparticles by spark discharge - for growth of epitaxial nanowires. *Gold Bulletin* 2009, 42, (1), 20-26.

35.   Lee, K. M.; Lee, D. J.; Ahn, H., XRD and TEM studies on tin oxide(II) nanoparticles prepared by inert gas condensation. *Materials Letters* 2004, 58, (25), 3122-3125.

36.   Dong, X. L.; Choi, C. J.; Kim, B. K., Chemical synthesis of Co nanoparticles by chemical vapor condensation. *Scripta Materialia* 2002, 47, (12), 857-861.

37.   Itoh, Y.; Okuyama, K., Preparation of agglomerate-free and highly crystalline (Ba-0.5, Sr-0.5)TiO3 nanoparticles by salt-assisted spray pyrolysis. *Journal of the Ceramic Society of Japan* 2003, 111, (11), 815-820.

38.   Chung, Y. M.; Rhee, H. K., Synthesis and catalytic applications of dendrimer-templated bimetallic nanoparticles. *Catal Surv Asia* 2004, 8, (3), 211-223.

39.   Akurati, K. K.; Vital, A.; Hany, R.; Bommer, B.; Graule, T.; Winterer, M., One-step flame synthesis of SnO2/TiO2 composite nanoparticles for photocatalytic applications. *International Journal of Photoenergy* 2005, 7, (4), 153-161.

40.   Madler, L.; Pratsinis, S. E., Bismuth oxide nanoparticles by flame spray pyrolysis. *Journal of the American Ceramic Society* 2002, 85, (7), 1713-1718.

41.   Chang, Y. H.; Wang, H. W.; Chiu, C. W.; Cheng, D. S.; Yen, M. Y.; Chiu, H. T., Low-temperature synthesis of transition metal nanoparticles from metal complexes and organopolysilane oligomers. *Chemistry of Materials* 2002, 14, (10), 4334-4338.

42.   Aiken, J. D.; Finke, R. G., A review of modern transition-metal nanoclusters: their synthesis, characterization, and applications in catalysis. *Journal of Molecular Catalysis a-Chemical* 1999, 145, (1-2), 1-44.

43.   Schaadt, D. M.; Feng, B.; Yu, E. T., Enhanced semiconductor optical absorption via surface plasmon excitation in metal nanoparticles. *Applied Physics Letters* 2005, 86, (6), -.

44.   Bhattacharjee, S.; Dotzauer, D. M.; Bruening, M. L., Selectivity as a Function of Nanoparticle Size in the Catalytic Hydrogenation of Unsaturated Alcohols. *Journal of the American Chemical Society* 2009, 131, (10), 3601-3610.

45.   Masciangioli, T.; Zhang, W. X., Environmental technologies at the nanoscale. *Environmental Science & Technology* 2003, 37, (5), 102a-108a.

46.   Amama, P. B.; Maschmann, M. R.; Fisher, T. S.; Sands, T. D., Dendrimer-templated Fe nanoparticles for the growth of single-wall carbon nanotubes by plasma-enhanced CVD. *Journal of Physical Chemistry B* 2006, 110, (22), 10636-10644.

47.   Fukui, T.; Murata, K.; Ohara, S.; Abe, H.; Naito, M.; Nogi, K., Morphology control of Ni-YSZ cermet anode for lower temperature operation of SOFCs. *Journal of Power Sources* 2004, 125, (1), 17-21.

48.   Das, D.; Lin, S. S., Double-coated poly (butylcynanoacrylate) nanoparticulate delivery systems for brain targeting of dalargin via oral administration. *Journal of Pharmaceutical Sciences* 2005, 94, (6), 1343-1353.

49.   Fudouzi, H., Fabricating high-quality opal films with uniform structure over a large area. *Journal of Colloid and Interface Science* 2004, 275, (1), 277-283.

50.   A.H.El-Hag; S.H. Jayaram; Cherney, E. A. *2004 Annual Report of Conference on Electrical Insulatin and Dielectric Phenomena*; 2005; pp 385-388.

51.   Wijngaarden, R. J.; Kronberg, A.; Westerterp, K. R., *Industrial catalysis : optimizing catalysts and processes* Wiley–VCH: Weinheim, 1998.

52.   Cavallaro, A., EPA's new PM standards. *Power Engineering* 2006, 110, (11), 40-+.

53.   Pope, C. A.; Burnett, R. T.; Thun, M. J.; Calle, E. E.; Krewski, D.; Ito, K.; Thurston, G. D., Lung cancer, cardiopulmonary mortality, and long-term exposure to fine particulate air pollution. *Jama-Journal of the American Medical Association* 2002, 287, (9), 1132-1141.

54.   D'Alessio, A.; D'Anna, A.; Gambi, G.; Minutolo, P.; Sgro, L.; Violi, A., Combustion generated nanoparticles. *Chimica e l'Industria* 1999, 81, 1001-1006.

55.   Kauppinen, E. I.; Pakkanen, T. A., Coal Combustion Aerosols - a Field-Study. *Environmental Science & Technology* 1990, 24, (12), 1811-1818.

56.   Lighty, J. S.; Veranth, J. M.; Sarofim, A. F., Combustion aerosols: Factors governing their size and composition and implications to human health. *Journal of the Air & Waste Management Association* 2000, 50, (9), 1565-1618.

57.   Shendrikar, A. D.; Ensor, D. S.; Cowen, S. J.; Woffinden, G. J.; Mcelroy, M. W., Size-Dependent Penetration of Trace-Elements through a Utility Baghouse. *Atmospheric Environment* 1983, 17, (8), 1411-1421.

58.   Xiong, C.; Friedlander, S. K., Morphological properties of atmospheric aerosol aggregates. *Proceedings of the National Academy of Sciences of the United States of America* 2001, 98, (21), 11851-11856.

59.   Cass, G. R.; Hughes, L. A.; Bhave, P.; Kleeman, M. J.; Allen, J. O.; Salmon, L. G., The chemical composition of atmospheric ultrafine particles. *Philosophical Transactions of the Royal Society of London Series a-Mathematical Physical and Engineering Sciences* 2000, 358, (1775), 2581-2592.

60.   Linak, W. P.; Wendt, J. O. L., Trace-Metal Transformation Mechanisms during Coal Combustion. *Fuel Processing Technology* 1994, 39, (1-3), 173-198.

61.   Haynes, B. S.; Neville, M.; Quann, R. J.; Sarofim, A. F., Factors Governing the Surface Enrichment of Fly-Ash in Volatile Trace Species. *Journal of Colloid and Interface Science* 1982, 87, (1), 266-278.

62.   Zappoli, S.; Andracchio, A.; Fuzzi, S.; Facchini, M. C.; Gelencser, A.; Kiss, G.; Krivacsy, Z.; Molnar, A.; Meszaros, E.; Hansson, H. C.; Rosman, K.; Zebuhr, Y., Inorganic, organic and macromolecular components of fine aerosol in different areas of Europe in relation to their water solubility. *Atmospheric Environment* 1999, 33, (17), 2733-2743.

63.   Dickson, L. C.; Lenoir, D.; Hutzinger, O., Surface-Catalyzed Formation of Chlorinated Dibenzodioxins and Dibenzofurans during Incineration. *Chemosphere* 1989, 19, (1-6), 277-282.

64.   Lomnicki, S.; Dellinger, B., A detailed mechanism of the surface-mediated formation of PCDD/F from the oxidation of 2-chlorophenol on a CuO/silica surface. *Journal of Physical Chemistry A* 2003, 107, (22), 4387-4395.

65.   Evans, C. S.; Dellinger, B., Surface-mediated formation of polybrominated dibenzo-p-dioxins and dibenzofurans from the high-temperature pyrolysis of 2-bromophenol on a CuO/silica surface. *Environmental Science & Technology* 2005, 39, (13), 4857-4863.

66.   Nganai, S.; Lomnicki, S.; Dellinger, B., Ferric Oxide Mediated Formation of PCDD/Fs from 2-Monochlorophenol. *Environmental Science & Technology* 2009, 43, (2), 368-373.

67.   Grassman, J. A.; Masten, S. A.; Walker, N. J.; Lucier, G. W., Animal models of human response to dioxins. *Environmental Health Perspectives* 1998, 106, 761-775.

68.   Mukerjee, D., Health impact of polychlorinated dibenzo-p-dioxins: A critical review. *Journal of the Air & Waste Management Association* 1998, 48, (2), 157-165.

69.   Demers, R.; Perrin, E.; Becker, C.; Borak, J.; Cannella, J.; Goldstein, B.; Hall, A.; Jackson, R. J.; Rodnick, J.; Wheater, R.; Wummer, B., Dioxin Toxicity. *American Family Physician* 1993, 47, (4), 855-861.

70.   Narula, C. K.; Moses, M. J.; Xu, Y.; Blom, D. A.; Allard, L. F.; Shelton, W. A.; Schneider, W. F., Catalysis by design - theoretical and experimental studies of model catalysts. *Soc. Automot. Eng., [Spec. Publ.] SP FIELD Full Journal Title:Society of Automotive Engineers, [Special Publication] SP* 2007, SP-2113, (Nanotechnology for Automotive Applications), 61-68.

71.   Ramallo-Lopez, M. A.; Requejo, F. G.; Craievich, A. F.; Wei, J.; Avalos-Borja, M.; Iglesia, E., Complementary methods for cluster size distribution measurements: supported platinum nanoclusters in methane reforming catalysts. *Journal of Molecular Catalysis a-Chemical* 2005, 228, (1-2), 299-307.

72.   Pool, R., Clusters - Strange Morsels of Matter. *Science* 1990, 248, (4960), 1186-1188.

73.   Floriano, P. N.; Noble, C. O.; Schoonmaker, J. M.; Poliakoff, E. D.; McCarley, R. L., Cu(0) nanoclusters derived from poly(propylene imine) dendrimer complexes of CU(II). *Journal of the American Chemical Society* 2001, 123, (43), 10545-10553.

74.   Schmid, G., Chemical synthesis of large metal clusters and their properties. *Nanostructured Materials* 1995, 6, (1-4), 15-24.

75.   Cushing, B. L.; Kolesnichenko, V. L.; O'Connor, C. J., Recent advances in the liquid-phase syntheses of inorganic nanoparticles. *Chemical Reviews* 2004, 104, (9), 3893-3946.

76.   Masala, O.; Seshadri, R., Synthesis routes for large volumes of nanoparticles. *Annual Review of Materials Research* 2004, 34, 41-81.

77.   Gai, P. L.; Roper, R.; White, M. G., Recent advances in nanocatalysis research. *Current Opinion in Solid State & Materials Science* 2002, 6, (5), 401-406.

78.   Tsodikov, M. V.; Rostovshchikova, T. N.; Smirnov, V. V.; Kiseleva, O. I.; Maksimov, Y. V.; Suzdalev, I. P.; Ikorskii, V. N., Structure and size effects in catalysis by immobilized nanoclusters of iron oxides. *Catalysis Today* 2005, 105, (3-4), 634-640.

79.   Kurr, P.; Kasatkin, I.; Girgsdies, F.; Trunschke, A.; Schlogl, R.; Ressler, T., Microstructural characterization of Cu/ZnO/Al2O3 catalysts for methanol steam reforming - A comparative study. *Applied Catalysis a-General* 2008, 348, (2), 153-164.

80.   Lisiecki, I.; Billoudet, F.; Pileni, M. P., Syntheses of copper nanoparticles in gelified microemulsion and in reverse micelles. *J Mol Liq* 1997, 72, (1-3), 251-261.

81.   Kralik, M.; Biffis, A., Catalysis by metal nanoparticles supported on functional organic polymers. *J Mol Catal a-Chem* 2001, 177, (1), 113-138.

82.   Velarde-Ortiz, R.; Larsen, G., A poly(propylene imine) (DAP-Am-64) dendrimer as Cu2+ chelator for the synthesis of copper oxide clusters embedded in sol-gel derived matrixes. *Chem Mater* 2002, 14, (2), 858-866.

83.   Esumi, K., Dendrimers for nanoparticle synthesis and dispersion stabilization. *Top Curr Chem* 2003, 227, 31-52.

84.   Fujdala, K. L.; Drake, I. J.; Bell, A. T.; Tilley, T. D., Atomic level control over surface species via a molecular precursor approach: Isolated Cu(I) sites and Cu nanoparticles supported on mesoporous silica. *J Am Chem Soc* 2004, 126, (35), 10864-10866.

85.   Gu, J. L.; Shi, J. L.; Xiong, L. M.; Chen, H. R.; Ruan, M. L., A new strategy to incorporate highly dispersed nanoparticles into the pore channels of mesoporous silica thin films. *Micropor Mesopor Mat* 2004, 74, (1-3), 199-204.

86.   Shi, X. Y.; Sun, K.; Balogh, L. P.; Baker, J. R., Synthesis, characterization, and manipulation of dendrimer-stabilized iron sulfide nanoparticles. *Nanotechnology* 2006, 17, (18), 4554-4560.

87.   He, B. L.; Ha, Y.; Liu, H. F.; Wang, K. M.; Liew, K. Y., Size control synthesis of polymer-stabilized water-soluble platinum oxide nanoparticles. *Journal of Colloid and Interface Science* 2007, 308, (1), 105-111.

88.   Ledesma-Garcia, J.; Garcia, I. L. E.; Rodriguez, F. J.; Chapman, T. W.; Godinez, L. A., Immobilization of dendrimer-encapsulated platinum nanoparticles on pretreated carbon-fiber surfaces and their application for oxygen reduction. *J Appl Electrochem* 2008, 38, (4), 515-522.

89.   Caruntu, D.; Caruntu, G.; Chen, Y.; O'Connor, C. J.; Goloverda, G.; Kolesnichenko, V. L., Synthesis of variable-sized nanocrystals of Fe3O4 with high surface reactivity. *Chemistry of Materials* 2004, 16, (25), 5527-5534.

90.   Strable, E.; Bulte, J. W. M.; Moskowitz, B.; Vivekanandan, K.; Allen, M.; Douglas, T., Synthesis and characterization of soluble iron oxide-dendrimer composites. *Chemistry of Materials* 2001, 13, (6), 2201-2209.

91.   Tomalia, D. A.; Baker, H.; Dewald, J.; Hall, M.; Kallos, G.; Martin, S.; Roeck, J.; Ryder, J.; Smith, P., A New Class of Polymers - Starburst-Dendritic Macromolecules. *Polymer Journal* 1985, 17, (1), 117-132.

92.   Bosman, A. W.; Janssen, H. M.; Meijer, E. W., About dendrimers: Structure, physical properties, and applications. *Chemical Reviews* 1999, 99, (7), 1665-1688.

93.   Advances in Dendritic Macromolecules. In Newkome, G. R., Ed. JAI Press: Greenwich, Conn., 1994; Vol. 1.

94.   Sheiko., S. S.; Möller., M., Hyperbranched Macromolecules: Soft Particles with Adjustable Shape and Persistent Motion Capability. In *Dendrimers III*, Springer Berlin: Heidelberg, 2001; Vol. 212.

95.   Hodge, P., Organic-Chemistry - Polymer Science Branches Out. *Nature* 1993, 362, (6415), 18-19.

96.   Patri, A. K.; Majoros, I. J.; Baker, J. R., Dendritic polymer macromolecular carriers for drug delivery. *Current Opinion in Chemical Biology* 2002, 6, (4), 466-471.

97.   Knecht, M. R.; Garcia-Martinez, J. C.; Crooks, R. M., Synthesis, characterization, and magnetic properties of dendrimer-encapsulated nickel nanoparticles containing < 150 atoms. *Chemistry of Materials* 2006, 18, (21), 5039-5044.

98.   Li, Z. M.; Liu, J. M.; Chen, X. H.; Yang, M. L.; Chen, X. H.; Shi, X. M., A new 4.0-generation dendrimer phosphorescence labeling reagent and its application to determination of trace alkaline phosphatase by affinity adsorption solid substrate-room temperature phosphorimetry. *Chinese Journal of Chemistry* 2007, 25, (10), 1529-1535.

99.   Jain, N. K.; Gupta, U., Application of dendrimer-drug complexation in the enhancement of drug solubility and bioavailability. *Expert Opinion on Drug Metabolism & Toxicology* 2008, 4, (8), 1035-1052.

100.   Gong, A. J.; Fan, Q. H.; Chen, Y. M.; Liu, H. W.; Chen, C. F.; Xi, F., Two-phase hydroformylation reaction catalysed by rhodium-complexed water-soluble dendrimers. *Journal of Molecular Catalysis a-Chemical* 2000, 159, (2), 225-232.

101.   Chase, P. A.; Gebbink, R. J. M. K.; van Koten, G., Where organometallics and dendrimers merge: the incorporation of organometallic species into dendritic molecules. *Journal of Organometallic Chemistry* 2004, 689, (24), 4016-4054.

102.   Alper, H.; Arya, P.; Bourque, S. C.; Jefferson, G. R.; Manzer, L. E., Heck reaction using palladium complexed to dendrimers on silica. *Canadian Journal of Chemistry-Revue Canadienne De Chimie* 2000, 78, (6), 920-924.

103.   Wu, L.; Li, B. L.; Huang, Y. Y.; Zhou, H. F.; He, Y. M.; Fan, Q. H., Phosphine dendrimer-stabilized palladium nanoparticles, a highly active and recyclable catalyst for the Suzuki-Miyaura reaction and hydrogenation. *Organic Letters* 2006, 8, (16), 3605-3608.

104.   Zhang, F. X.; Miao, S.; Yang, Y. L.; Zhang, X.; Chen, J. X.; Guan, N. J., Size-dependent hydrogenation selectivity of nitrate on Pd-Cu/TiO2 catalysts. *Journal of Physical Chemistry C* 2008, 112, (20), 7665-7671.

105.   Giraudon, J. M.; Nguyen, T. B.; Leclercq, G.; Siffert, S.; Lamonier, J. F.; Aboukais, A.; Vantomme, A.; Su, B. L., Chlorobenzene total oxidation over palladium supported on ZrO2, TiO2 nanostructured supports. *Catalysis Today* 2008, 137, (2-4), 379-384.

106.   Wang, Z. L.; Liu, Q. S.; Yu, J. F.; Wu, T. H.; Wang, G. J., Surface structure and catalytic behavior of silica-supported copper catalysts prepared by impregnation and sol-gel methods. *Applied Catalysis a-General* 2003, 239, (1-2), 87-94.

107.   Sun, L.; Crooks, R. M., Dendrimer-Mediated Immobilization of Catalytic Nanoparticles on Flat, Solid Supports. *Langmuir* 2002, 18, 8231-8236.

108.   Lemo, J.; Heuze, K.; Astruc, D., Synthesis and catalytic activity of DAB-dendrimer encapsulated Pd nanoparticles for the Suzuki coupling reaction. *Inorganica Chimica Acta* 2006, 359, (15), 4909-4911.

109.   Lang, H. F.; May, R. A.; Iversen, B. L.; Chandler, B. D., Dendrimer-encapsulated nanoparticle precursors to supported platinum catalysts. *Journal of the American Chemical Society* 2003, 125, (48), 14832-14836.

110.   Liu, D. X.; Gao, J. X.; Murphy, C. J.; Williams, C. T., In situ attenuated total reflection infrared spectroscopy of dendrimer-stabilized platinum nanoparticles adsorbed on alumina. *Journal of Physical Chemistry B* 2004, 108, (34), 12911-12916.

111.   Megaridis, C. M.; Dobbins, R. A., Comparison of Soot Growth and Oxidation in Smoking and Non-Smoking Ethylene Diffusion Flames. *Combustion Science and Technology* 1989, 66, (1-3), 1-16.

112.   Haynes, B. S.; Wagner, H. G., Soot formation. *Prog. Energy Combust. Sci. FIELD Full Journal Title:Progress in Energy and Combustion Science* 1981, 7, (4), 229-73.

113.   Oktem, B.; Tolocka, M. P.; Zhao, B.; Wang, H.; Johnston, M. V., Chemical species associated with the early stage of soot growth in a laminar premixed ethylene-oxygen-argon flame. *Combustion and Flame* 2005, 142, (4), 364-373.

114.   Homann, K. H., Carbon Formation in Premixed Flames. *Combustion and Flame* 1967, 11, (4), 265-&.

115.   Celnik, M.; Raj, A.; West, R.; Patterson, R.; Kraft, M., Aromatic site description of soot particles. *Combustion and Flame* 2008, 155, (1-2), 161-180.

116.   Pinkerton, K. E.; Zhou, Y. M.; Teague, S. V.; Peake, J. L.; Walther, R. C.; Kennedy, I. M.; Leppert, V. J.; Aust, A. E., Reduced lung cell proliferation following short-term exposure to ultrafine soot and iron particles in neonatal rats: Key to impaired lung growth? *Inhalation Toxicology* 2004, 16, 73-81.

117.   Richter, H.; Howard, J. B., Formation of polycyclic aromatic hydrocarbons and their growth to soot - a review of chemical reaction pathways. *Progress in Energy and Combustion Science* 2000, 26, (4-6), 565-608.

118.   Wood, A. W.; Levin, W.; Chang, R. L.; Huang, M. T.; Ryan, D. E.; Thomas, P. E.; Lehr, R. E.; Kumar, S.; Koreeda, M.; Akagi, H.; Ittah, Y.; Dansette, P.; Yagi, H.; Jerina, D. M.; Conney, A. H., Mutagenicity and Tumor-Initiating Activity of Cyclopenta(C,D)Pyrene and Structurally Related-Compounds. *Cancer Research* 1980, 40, (3), 642-649.

119.   Busby, W. F.; Stevens, E. K.; Kellenbach, E. R.; Cornelisse, J.; Lugtenburg, J., Dose-Response Relationships of the Tumorigenicity of Cyclopenta[Cd]Pyrene, Benzo[a]Pyrene and 6-Nitrochrysene in a Newborn Mouse Lung Adenoma Bioassay. *Carcinogenesis* 1988, 9, (5), 741-746.

120.   Moser, G. J.; Foley, J.; Burnett, M.; Goldsworthy, T. L.; Maronpot, R., Furan-induced dose-response relationships for liver cytotoxicity, cell proliferation, and tumorigenicity (furan-induced liver tumorigenicity). *Experimental and Toxicologic Pathology* 2009, 61, (2), 101-111.

121.   IRAC *SOOTS (summary and evaluation)*; International Agency for Research on Cancer: 1985; p 219.

122.   Kuhlbusch, T. A. J., Black carbon and the carbon cycle. *Science* 1998, 280, (5371), 1903-1904.

123.   Rosenthal, E., Third-World Stove Soot Is Target in Climate Fight *The New York Times* April 15, 2009.

124.   Bozzano, G.; Dente, M.; Faravelli, T.; Ranzi, E., Fouling phenomena in pyrolysis and combustion processes. *Applied Thermal Engineering* 2002, 22, (8), 919-927.

125.   Uchida, T.; Ohashi, O.; Kawamoto, H.; Yoshimura, H.; Kobayashi, K.; Tanimura, M.; Fujikawa, N.; Nishimoto, T.; Awata, K.; Tachibana, M.; Kojima, K., Synthesis of single-wall carbon nanotubes from diesel soot. *Japanese Journal of Applied Physics Part 1-Regular Papers Brief Communications & Review Papers* 2006, 45, (10A), 8027-8029.

126.   Mansurov, Z. A., Soot formation in combustion processes (review). *Combustion Explosion and Shock Waves* 2005, 41, (6), 727-744.

127.   Naydenova, I.; Vlasov, P. A.; Warnatz, J. In *Detailed Kinetic Modeling of Soot Formation in Pyrolysis of Benzene/Acetylene/Argon Mixtures*, Conf-Proceedings of the European Combustion Meeting, 2005; 2005.

128.   Naydenova, I.; Nullmeier, M.; Warnatz, J.; Vlasov, P. A., Detailed kinetic modeling of soot formation during shock-tube pyrolysis of C6H6: Direct comparison with the results of time-resolved laser-induced incandescence (LII) and CW-laser extinction measurements. *Combust Sci Technol* 2004, 176, (10), 1667-1703.

129.   Tesner, P. A.; Shurupov, S. V., Soot formation during pyrolysis of naphthalene, anthracene and pyrene. *Combust Sci Technol* 1997, 126, (1-6), 139-151.

130.   Alexiou, A.; Williams, A., Soot formation in shock-tube pyrolysis of toluene, toluene-methanol, toluene-ethanol, and toluene-oxygen mixtures. *Combust Flame* 1996, 104, (1-2), 51-65.

131.   Commodo, M.; Violi, S.; D'Anna, A.; D'Alessio, A.; Allouis, C.; Beretta, F.; Minutolo, P., Soot and nanoparticle formation in laminar and turbulent flames. *Combust Sci Technol* 2007, 179, (1-2), 387-400.

132.	D'Anna, A.; Alfe, A.; Apicella, B.; Tregrossi, A.; Ciajolo, A., Effect of Fuel/Air ratio and aromaticity on sooting behavior of premixed heptane flames. *Energ Fuel* 2007, 21, (5), 2655-2662.

133.	Knorre, V. G.; Tanke, D.; Thienel, T.; Wagner, H. G., Soot formation in the pyrolysis of benzene/acetylene and acetylene/hydrogen mixtures at high carbon concentrations. *Conf-Symp. (Int.) Combust., [Proc.] FIELD Full Journal Title:Symposium (International) on Combustion, [Proceedings]* 1996, 26th, (Vol. 2), 2303-2310.

134.	Mendiara, T.; Domene, M. P.; Millera, A.; Bilbao, R.; Alzueta, M. U., An experimental study of the soot formed in the pyrolysis of acetylene. *J Anal Appl Pyrol* 2005, 74, (1-2), 486-493.

135.	Mikofski, M. A. Flame Structure and Soot Formation in Inverse Diffusion Flames. University of California, Berkeley, 2005.

136.	Parker, T. E.; Foutter, R. R.; Rawlins, W. T., Soot initiation and particle growth in the pyrolysis of toluene at high inert gas pressure. *Conf-AIP Conf. Proc. FIELD Full Journal Title:AIP Conference Proceedings* 1990, 208, (Curr. Top. Shock Waves), 481-6.

137.	Shurupov, S. V.; Tesner, P. A., Soot formation during isothermal pyrolysis of carbon tetrachloride and methane-carbon tetrachloride mixture. *Conf-Symp. (Int.) Combust., [Proc.] FIELD Full Journal Title:Symposium (International) on Combustion, [Proceedings]* 1998, 27th, (Vol. 1), 1581-1588.

138.	Bockhorn, H., *Soot Formation in Combustion: Mechanisms and Models*. Springer-Verlag: Berlin, 1994.

139.	Longwell, J. P.; Wornat, M. J.; Mukherjee, J.; Sarofim, A., The Role of Biaryl Reactions in PAH and Soot Formation. In *Springer Series in Chemical Physics*, Springer-Verlag: Berlin, 1994; Vol. 54.

140.	Frenklach, M., Reaction mechanism of soot formation in flames. *Phys Chem Chem Phys* 2002, 4, (11), 2028-2037.

141.	Krestinin, A. V., Detailed modeling of soot formation in hydrocarbon pyrolysis. *Combust Flame* 2000, 121, (3), 513-524.

142.	M.Frenklach; Wang, H., Soot Formation in Combustion In Bockhorn, H., Ed. Springer: 1994; Vol. 59.

143.	Frenklach, M.; Wang, H., Detailed modeling of soot particle nucleation and growth. *Symp. (Int.) Combust., [Proc.]* 1991, 23rd, 1559-66.

144.	Bonczyk, P. A., Effects of Metal Additives on Soot Precursors and Particulates in a C2h4/O2/N2/Ar Premixed Flame. *Fuel* 1991, 70, (12), 1403-1411.

145.   Hirasawa, T.; Sung, C. J.; Yang, Z. W.; Joshi, A.; Wang, H., Effect of ferrocene addition on sooting limits in laminar premixed ethylene-oxygen-argon flames. *Combustion and Flame* 2004, 139, (4), 288-299.

146.   Mitchell, J. B. A., Smoke Reduction from Burning Crude-Oil Using Ferrocene and Its Derivatives. *Combustion and Flame* 1991, 86, (1-2), 179-184.

147.   Ritrievi, K. E.; Longwell, J. P.; Sarofim, A. F., The Effects of Ferrocene Addition on Soot Particle Inception and Growth in Premixed Ethylene Flames. *Combustion and Flame* 1987, 70, (1), 17-31.

148.   Howard, J. B.; Kausch, W. J., Soot Control by Fuel Additives. *Progress in Energy and Combustion Science* 1980, 6, (3), 263-276.

149.   Balogh, L.; Tomalia, D. A., Poly(amidoamine) dendrimer-templated nanocomposites. 1. Synthesis of zerovalent copper nanoclusters. *Journal of the American Chemical Society* 1998, 120, (29), 7355-7356.

150.   Zhao, M. Q.; Crooks, R. M., Dendrimer-encapsulated Pt nanoparticles: Synthesis, characterization, and applications to catalysis. *Advanced Materials* 1999, 11, (3), 217-+.

151.   Bosman, A. W.; Schenning, A. P. H. J.; Janssen, R. A. J.; Meijer, E. W., Well-defined metallodendrimers by site-specific complexation. *Chemische Berichte-Recueil* 1997, 130, (6), 725-728.

152.   Takasuga, T.; Makino, T.; Tsubota, K.; Takeda, N., Formation of dioxins (PCDDs/PCDFs) by dioxin-free fly ash as a catalyst and relation with several chlorine-sources. *Chemosphere* 2000, 40, (9-11), 1003-1007.

CHAPTER II: EXPERIMENTAL

2.1   Dendrimer-Templated Synthesis of Metal Oxide Nanoclusters with Support

2.1.1   Chemicals

Metal Precursor – All the metal precursors were used as received from Sigma-Aldrich, including cupric nitrate hemi(pentahydrate) $Cu(NO_3)_2 \cdot 2.5H_2O$ (99.99%), ferric nitrate nonahydrate $Fe(NO_3)_3 \cdot 9H_2O$ (99.99%) and nickel(II) nitrate hexahydrate $Ni(NO_3)_2 \cdot 6H_2O$ (99.999%).

Dendrimer – Amine-terminated poly (propylene imine) (PPI) 4th generation dendrimer DAB-AM-32 (G4) was purchased from SyMO-CHEM and used without further modification.

Substrate – Cab-O-Sil (CABOT Cop., EH-5) is a high purity (99.8%) fume silica powder with high surface area (380 m^2/g) and average particle size (aggregated) of 0.2-0.3 µm.[1] To test the generality of the synthesis route, titanium oxide (Sigma-Aldrich) with particle size <100nm (BET) was used as well.

Solvent – All aqueous solutions were prepared with HPLC chromatographic grade Methanol (99.8%).

2.1.2   Synthesis Procedure

Amine-terminated poly (propylene imine) (PPI) dendrimer DAB-Am$_{2n}$ was used as a macrochelating agent for synthesis of metal oxide nanoclusters.   DAB stands for the diaminobutane-core, and 2n for the number of primary amine terminal groups which is associated with the generation m ($n = 2^m$).   In this study, 4th generation of DAB dendrimer which has 32 amine terminal groups was used and symbolized as G4 in this dissertation. Similarly, the nomenclature used to describe the dendrimer-metal complex is as follows: G4Me$_n$, where Me represents the metal and n is the number of metal ions coordinated in one G4 dendrimer molecule. It was reported that the amine terminal groups coordinated with Cu^{2+} ions

in a 2:1 stoichiometric ratio.[2-3] Therefore, one G4 molecule can complex up to 16 Cu^{2+} ions in a fully stoichiometric substitution. **Figure 2.1** presents the structure of a G4 molecule and its fully substituted cupric complex analogue $G4Cu(II)_{16}$ in a 2-dimensional projection. The oxygen atoms present in the complex molecule could be associated with the methanol solvent, nitrate anions or water.[3]
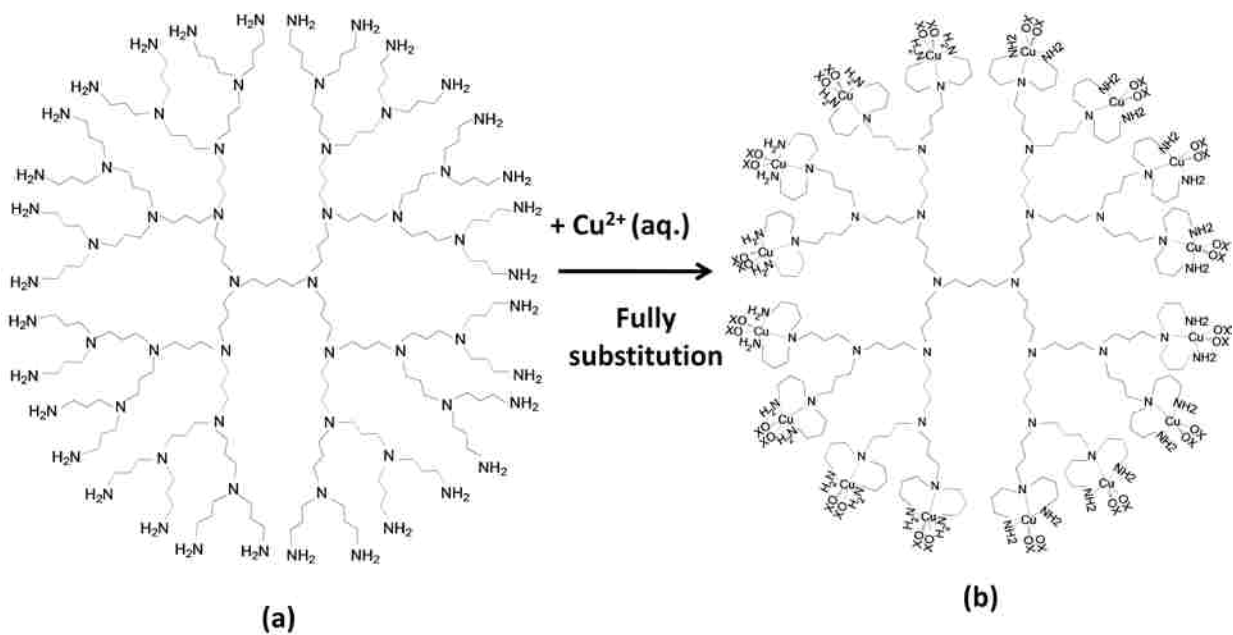
Figure 2.1 Generation 4 Amine-terminated Poly(propylene imine) Dendrimer (a) Un-substituted Dendrimer DAB-Am32, (b) Fully Substituted Dendrimeric-Copper Complex DAB-Am32-Cu(II)₁₆

The procedure for synthesis of substituted dendrimer copper complexes can be illustrated by the example of $G4Cu(II)_{16}$. A methanolic solution of $Cu(NO_3)_2 \cdot 2.5H_2O$ (5 mL, 10 mM), in pale blue, color was added to a solution of G4 in methanol (20 mL, 0.156 mM), immediately resulting in an ocean blue color due to the complexation of copper with amino groups. It should be noted that the quantities of the solutions taken were selected to obtain a final dendrimer-Cu(II) solution with the 2mM of Cu(II) concentration. Cu(II) concentration was kept constant in

the preparations of other substituted level dendrimer complexes, which required the concentrations of G4 for half and quarter substituted cupric dendrimer complexes were 0.312 mM and 0.624 mM, respectively. The final solution was thoroughly stirred for 30 min to ensure the complete coordination between Cu ions and dendrimers.[3]

To impregnate the silica powder with the 2 mM dendrimer-Cu(II)$_n$ methanol solution, Cab-O-Sil powder in the amount corresponding to final 5 wt.% CuO/SiO$_2$ was suspended in methanol and sonicated for 20 minutes. A dendrimer-copper complex solution was then added, and the solvent was removed by rotary vacuum evaporation, producing dendrimer- Cu(II) coated silica powder in sky blue color. To remove the residual methanol prior to calcination, the solid powder was oven dried at 120 °C for 6 hours. To burn-off the dendrimeric material and oxidize the metal species, the dried powder was then calcined for another 5 hours in a high temperature furnace. Except to examine the calcination temperature effect on the formation of metal oxide nanoclusters, all the pre-dried powder samples were calcined at 450 °C.

To minimize the probable agglomeration of dendrimer-metal complexes occurring in solution or on a supporting surface, as well as the surface migration and aggregation of the metal oxide nanoclusters during calcination process, a different preparation approach was used. Prior to solvent removal, the suspension containing dendrimer-Cu(II) complex and Cab-O-Sil silica was shaken for 24 hours to allow the diffusion and adsorption of the dendrimers on the silica surface. This approach was referred to as "pre-adsorption", which was applied to ensure no diffusion limitation of the dendrimer-Cu(II) complex to the surface of silica particles during the fast solvent evaporation process.

In order to test the generality of this synthesis method, other metals, e.g. Ni and Fe, and other supported matrixes, e.g. titanium oxide (TiO$_2$), were also selected for synthesis of other supported metal oxide nanoclusters system.

2.1.3   Characterization Techniques

2.1.3.1 Morphology Analysis (HR-TEM)

Nanoparticle images were obtained using a JEOL-2010 high-resolution transmission electron microscope (HR-TEM) operated at 200 kV with a LaB_6 emitter. With a magnification ranging from 50 – 1,500,000, it can image objects at a point-to-point resolution up to 0.23 nm. Initially the TEM was only equipped with a conventional film imaging system. The negative films were then scanned into a computer for digital processing. Later a CCD-camera (Gatan, model SC1000) was installed in TEM for imaging purposes, which produced digital images directly. Though two different imaging systems were used, the results obtained from both systems were comparable as calibration of the new system was conducted upon its installation. All images were taken in bright field mode. 400 meshes holey-carbon coated metallic TEM grids (purchased from SPI, West Chester, PA) were used for microscope imaging.

The powder sample for the test was initially suspended in methanol for 1 minute using an ultrasonic bath. Then a TEM grid was dipped into the resulted suspension for 5-10 seconds and dried in air to allow the deposition of silica particles on its carbon film. The digitized images were imported into the program ImageJ for measuring the diameter of each particle on the micrographs.[4-5] After that the tabulated data of ImageJ was imported into IGOR (WaveMatrics, IGOR PRO 5) to generate the particle-size distribution by making histogram graphs with bin-widths of 0.2 nm. Gaussian Fitting was also applied to the histograms to produce the statistical results, including the mean sizes and standard deviations of particles. For each sample, 150-500 particles were measured from several TEM micrographs to establish particle size distribution histograms.

EDS (Energy Dispersive X-ray Spectroscopy) was used to analyze local composition information of the interested region. This in-situ elemental analysis was conducted using an

EDAX DX-4 package integrated in the TEM system. In order to identify copper oxide nanoclusters, nickel TEM grids were used instead of the more typical copper grid. The measured area was typically 200x200 nm^2.

2.1.3.2 Elemental Analysis (XPS & XANES)

The XPS (X-ray Photoelectron Spectroscopy) analysis was performed using a Kratos AXIS 165 X-ray photoelectron spectrometer equipped with an Mg/Al source. Powder samples were fixed on a steel holder with double-sided adhesive tape (Type 415 acrylic, 3M) and inserted into the UHV chamber of the instrument (10^{-9} Torr). In order to remove the charging effect posing on the insulating samples, the Charge-Neutralization function was selected throughout the analysis procedure. To determine the elemental compositions, including carbon, gold stubs were used as the sample holder rather than adhesive tape which contains carbonaceous ingredients. Survey and high-resolution scans were collected with energies of 160 eV and 40 eV, respectively. The spectrometer utilized the hybrid magnification mode, providing for an analysis area of about 700 microns by 300 microns, which is suitable for survey mode spectroscopic XPS analysis at low- and high-energy resolutions.

XANES (X-ray absorption near edge structure) spectra at the Cu K-edge were collected using the Double Crystal Monochromator (DCM) beam line at CAMD synchrotron research center. A 20 wt.% sample of Cu(II)O mechanically ground with Cab-O-Sil silica was used as a reference sample for the study of copper-based nanoclusters. Each sample was packed into a 15 mm x 2 mm window in an aluminum sample holder with both sides of the opening sealed with Kapton tape. The reported spectra are the sum of 3 to 5 scans. The data extraction and plotting were performed using standard X-ray absorption methods included in the commercial analysis program WinXAS (Version 3.0).[6] Background subtraction and normalization were performed using WinXAS. Pre-edge absorption due to the background and detector were subtracted using a

linear fit to the data in the range of -150 to -50 eV relative to the sample edge energy (E_0). Each spectrum was then normalized using a constant determined by the average absorption in the range of 25-300 eV relative to E_0.

2.2   Thermal Diagnostic Studies of Chlorinated Benzenes over Metal Oxide Catalysts

2.2.1   Chemicals

Test Reagents – 1,2-Dichlorobenzene (o-DCBz) (99%) and monochlorobenzene (MCBz) (99.8%) were used as received from Sigma-Aldrich. It is well known that chlorinated hydrocarbons are an important category of air pollutants which generated from the municipal and medical waste incinerators. There is particular interest for studying their chemical reactions due to their environmental problems like air and water pollutions, as well as for industrial applications. In this work, o-DCBz and MCBz, which are structurally similar to the extremely toxic 2,4,7,8-tetrachlorodibenzodioxin, were chosen as the model compounds for studying their thermal degradation in the reactions with metal oxide (particles) catalysts. **Figure 2.2** presents the formula structure of o-DCBz and MCBz molecular as well as the dioxin.
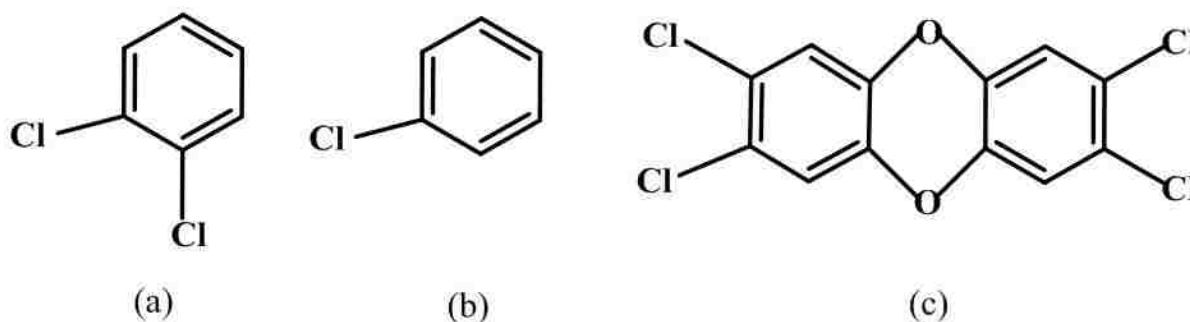

Figure 2.2 Chemical structure of (a) 1,2-dichlorobenzene, (b) monochlorobenzene, and (c) 2,4,7,8-tetrachlorodibenzodioxin

2.2.2   Preparation of Catalysts

Copper and iron oxide were selected for catalysis tests, partially due to their abundance in combustion emission and proven role in dioxin formation.[7] All supported metal oxide

nanocatalysts were prepared using the procedure described in the previous section. Briefly, a methanol solution of dendrimer-metal complex with concentration chosen to yield 5 wt.% metal oxides on the silica matrix was used as the active phase precursor and added into the suspension of amorphous silica powder (Cab-O-Sil). After the removal of solvent by rotary vacuum evaporation, thermal decomposition and oxidation in air of the silica-supported dendrimer-metal resulted in the formation of nanometer size (1-4 nm) clusters on the surface of silica substrate. Each metal oxide nanocatalyst was prepared in three different average size series by using fully, half, and quarter substituted metallic dendrimers as precursors, respectively.

The surrogate of larger metal oxide clusters used for catalytic comparison study was prepared by the incipient wetness method. To choose the amount of metal precursor (water solution) to make 5% metal oxide in silica system, the total volume of water was carefully added to the given mass of Cab-O-Sil powder to achieve incipient wetness, which required the water added to silica to be contained within the pore structure and/or bound to adsorption sites on the surface, i.e. no bulk water is present. The resulting gel was well mixed and dried at 120 °C for 24 hours, followed by 12 hour calcination at 450 °C in air to convert the metal nitrate salt into metal oxide on a silica support.

2.2.3   Characterization of Catalysts

Inductively Coupled Plasma (*ICP*) is an analytical technique used for the elemental determination. In this experimental section, a Spectro Ciros ICP analyzer was used to obtain the information of metal oxide loading in each catalyst. Extraction of metal species from the catalyst samples was performed by adding 2 ml of 70 wt.% nitric acid onto 10 mg 5 wt.% metal oxide/silica for 48 hour digestion. After that, 0.2 ml of the resulted supernate was diluted to 10 ml for ICP analysis. This dilution process reduced the concentration of nitric acid below 3 wt.% due to the limitation of ICP.

X-Ray Diffraction (XRD) Analysis was performed on a Bruker/Siemens D5000 Automated powder X-ray diffractometer to obtain the structure information of the metal oxide catalysts.

2.2.4　System for Thermal Diagnostic Studies

All catalysis tests were performed using the System for Thermal Diagnostic Studies (STDS), which was designed to study thermal behavior of organic and inorganic substances.[8-9] One of the advantages of STDS is that the substances for testing can be in gaseous, liquid, solid, composite, or even a multiphase constituent, which makes it suitable to investigate the thermally surface-mediated reaction of various organic compounds in the combustion study. Furthermore, its capability of in-line analysis increases the sensitivity for detecting products. STDS is a closed continuous system which has a modular design with interchangeable components to provide flexibility and versatility for different experimental tasks. In the catalytic study described in a later section, the STDS was composed of four major subassemblies, including the instrumentation console, thermal compartment equipped with high-temperature fused silica flow reactor, cryogenic trapping, and gas chromatograph/mass spectrometer (GC/MS) for effluent product separation and detection. The last two units were controlled and monitored through the computer interface. **Figure 2.3** illustrates the configuration of STDS in use.

The thermal compartment was basically composed of the oven of a Varian CP-3800 gas chromatograph with removal of the GC column and detector. Organic compounds in liquid phase were introduced into the reactor via the thermal injection port located on the top of GC. A digital syringe pump (KD Scientific, model 100) was used to inject liquid samples at a constant flow rate so that the initial concentration of sample can remain constant in the flow reactor. A quartz tube insert was installed in the injection port to maintain an inert atmosphere inside the STDS. In order to deliver organic reactants in gas-phase to the reactor, the samples were

vaporized in the temperature-controlled injector and then immediately transferred to the reactor by the gas carrier. The straight tube flow reactor (0.23 cm inner diameter, 20 cm long) was made of quartz which can remain stable at extremely high temperatures up to 1200 °C. Furthermore, all the transfer lines were made by stainless steel with fused silica coating to maintain a chemically inert atmosphere.
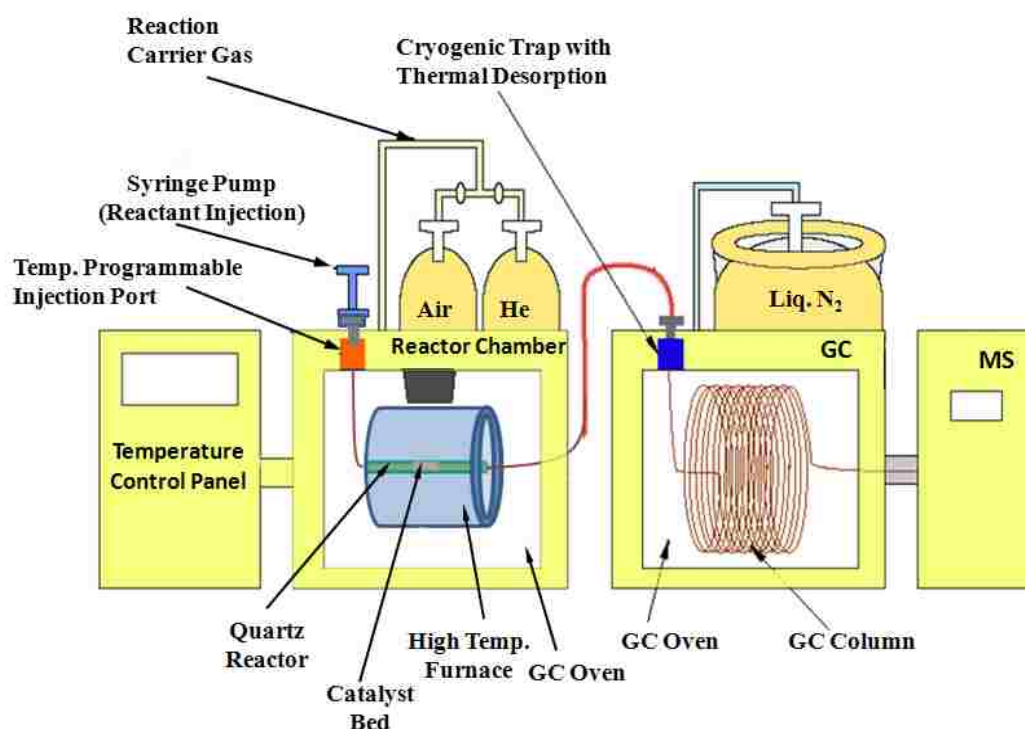
Figure 2.3 Diagram of System for Thermal Diagnostic Studies

The flow reactor was placed in a radiant ceramic tube furnace with separate temperature control from the instrumentation console (c.f. **Figure 2.4**). To maintain the thermal condition of surrounding peripheries of the furnace, including all connections coming from the injection port to the reactor and going from the reactor to the heated transfer line, the reaction assembly (reactor + furnace + connection) was housed in the GC oven. The downstream transfer line was composed of a deactivated silica-coated stainless steel tube which could be heated independently through the instrumentation console. In this study, the temperature of the GC oven and the

transfer line were held at 200 °C and 220 °C, respectively. This temperature setting was to maintain the organic reactants and products in a gas phase before transferring to the analysis units (GC/MS).

Figure 2.4 Fused silica flow reactor located in the high temperature furnace

The in-line GC/MS system (Varian, model CP-3800 GC and Saturn 2000 MS) was used for cryogenic trapping, separation and detection of the effluent from flow reactor. Liquid nitrogen was used to maintain the capillary column (Chrompack, part no. CP Sil 8) head at a low temperature (-60 °C) to ensure the effluents were trapped cryogenically. Immediately after the preset time for trapping, the column was temperature programmed from -60 to 300 °C at 15 °C/min so that the collected products are separated with characteristic retention time. Detection and quantification of the separated products were done by using the Mass Spectrometer (MS) where compounds with molecule weight between 40 to 650 amu could be analyzed. A computer

station installed with Saturn GC/MS software was used to collect GC/MS data so that the products could be identified with the included mass-spectral library (NIST and Saturn) and quantified digitally.

In order to conduct quantitative experiments, the STDS system had to be cleaned and well maintained regularly. Prior to use every day, the transfer line and reactor were heated under air flow at 300 °C and 450 °C, respectively. This procedure burned off the possible organic residual left from previous experiments. The GC/MS system was cleaned by using a preset method which set the column at 300 °C for 1 hour and returned to 120 °C after that. Additionally, the oil of the mechanical pump needs to be changed every six months.

2.2.5   Experimental Procedure

For each test, 10 mg of metal oxide/silica powder was mixed with 40 mg quartz particles (60-100 mesh). The use of quartz particles was to avoid pressure build-up, which occurs for fine powder packed beds. Furthermore, addition of quartz also helped to avoid local overheating and maintained space velocity. The catalyst was placed in a packed bed between quartz wool plugs in a 3.9 mm i.d. fused silica reactor in the STDS.

For all experiments, the volumetric flow rate through the reactor was maintained at 20 cc/min and the inject rate of liquid reactants was at 1 µL/hr. With these settings, the contact time for reactant on solid active phase is approximate 0.03~0.05 second, and the gas phase concentration of reactants was 200 ppm and 183 ppm for o-DCBz and MCBz, respectively. To avoid condensation of the reaction products, all transfer lines were maintained at a constant temperature of 200 °C. Ultra pure helium was used as carrier gas for pyrolytic reaction, while 20% oxygen in helium was used for oxidative reaction.

A blank test at a temperature of 200 °C was performed prior to each catalytic test to ensure the quantitative transportation of the gas reactants. The tests of chlorinated benzenes

reaction over metal oxide catalysts for each temperature were conducted in the STDS system with the detailed procedure described as following.

1. Load the catalytic sample contained reactor into the ceramic furnace with all connections tightened. Set the furnace to the desired reaction temperature.

2. Set the GC oven (the one that houses the reactor) and the transfer-line temperature at 200 °C to maintain the sample in gas-phase throughout the STDS.

3. Set the injection port at the temperature (180 °C for o-DCBz and 135 °C for MCBz) to vaporize all liquid sample into a gas phase before entering flow reactor.

4. Once the furnace was heated to a preset temperature, switch on the carrier gas (helium or oxygen/helium mixture) for reactant with set flow rate of 20 cc/min.

5. Program the GC/MS run from an initial set temperature of -60 °C with a holding time of 5 minutes to 300 °C at the rate of 15 °C/min for duration of 29.1 minutes.

6. Open the liquid nitrogen valve to cool the cryogenic trapping of the GC to -60 °C.

7. Insert the transfer line into the injection port of the GC/MS.

8. When all temperatures are stabilized and the flow rate is constant, the sample is ready to be injected. Draw up desired amount of liquid reactants into a syringe and place it in the syringe pump with the injection rate set at 1 uL/hr.

9. Insert the syringe to the injection port and start the syringe pump followed immediately with the start of the GC/MS run.

10. When the set injection runtime completes, stop the syringe pump and remove the transfer line from the injection port of the GC/MS.

11. Switch off the furnace and the oven to cool down adequately so that the quartz reactor can be removed safely.

12. Once the GC/MS run is complete, repeat above steps for next run with fresh catalyst.

2.2.6   Identification and Quantification of Reaction Products

Identification of each product (peak) was based on the mass spectrum, the software included library database (NIST 98 version 1.6d) and the standards of the products. Quantification of reactants and products was performed using the calibration curves of analytical standards. The yields of the products were calculated using the following expression.

$$Percent\ Yield = \frac{[Product]}{[Reactant]_0} \times 100$$

[Product] is the concentration of specific product formed (in moles), and [Reactant]$_0$ is the concentration of the reactant (in moles) injected into the reactor. All data were plotted using IGOR.

2.3   Combustion Studies in Entrained Flow Reactor

2.3.1   Chemicals

Metal precursor – Fully substituted dendrimer-metal complexes (G_4Cu_{16} or G_4Fe_{16}) were prepared in methanol solution according to **Section 2.1.2**.

Soot precursor - 1-Methylnaphthalene ($C_{11}H_{10}$) (95%) was chosen as the hydrocarbon fuel due to its high tendency to form soot.

Carrier Gas - Nitrogen (N_2) gas was used as the carrier gas in both injection ports. UHP Air (21% O_2, 79% N_2) was introduced to the flow reactor system only through the injection port of the particle generator. By adjusting the flow rates of the carrier gas, the resident time of reactants and oxygen concentration in the flow reactor can be tuned accordingly.

2.3.2   Design of Two-Zone Entrained Flow Reactor

The entrained flow reactor system was designed and built to study the effects of metal oxide nanoparticles on soot formation. The schematic diagram of the experimental setup is presented in **Figure 2.5**. The flow reactor was composed of 4 parts: particle generator (1st stage
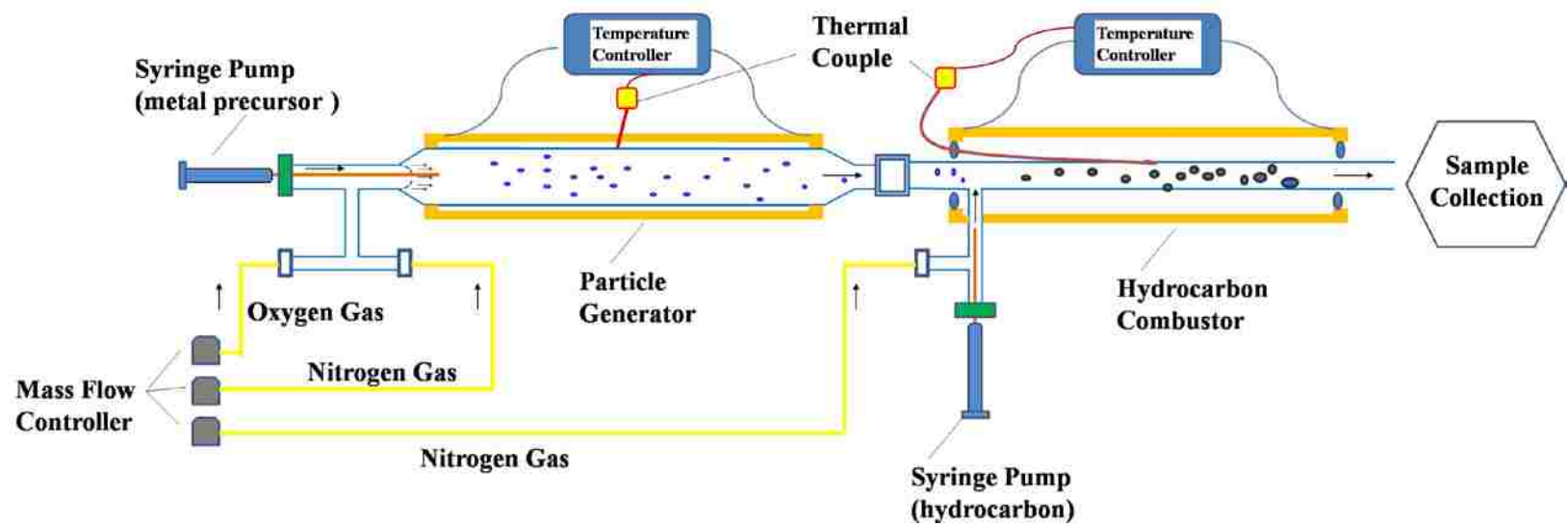
Figure 2.5 Schematic diagram of ultrafine entrained flow reactor

reactor), hydrocarbon combustor (2nd stage reactor), gas/liquid sample delivery systems (one for metal precursor and one for soot precursor), and sample collection assembly.

The particle generator consisted of a vacuum formed ceramic tube furnace (Omega, CRRS series) and a quartz tube reactor (I.D. 23 mm, Length 300 mm). The temperature inside the furnace is controlled electronically using a relay temperature controller. This segment was used to generate metal oxide nanoparticles suspended in gas phase. During experiments, a methanolic solution of the metal precursor was fed into the reactor at a constant flow rate by using a digital syringe pump, which was described previously in **section 2.2.2**. The injection port was configured with a gas/sample inlet and a quartz insert (I.D. 3.9 mm), which was customized with five evenly distributed pinholes (I.D. 1 mm) at the tip. This design was to ensure the injected liquid sample was "sprayed" uniformly into the heating zone without forming large condensed liquid drops. The carrier gases, air and nitrogen, were fed and controlled using the mass flow controllers (Omegalux®, model SSRL240DC25). The injection port was maintained at a mild temperature of 75 °C to ensure the complete vaporization of the solvent.

The outlet of the particle generator was connected to the hydrocarbon reactor, in which the hydrocarbon fuel was burned with or without the introduction of metal oxide particulate matter. This segment also consisted of a tube furnace (Omega, CRWS series) with thermal-electronic temperature control and a quartz tube reactor (I.D. 3.9 mm, Length 300 mm). To maintain the temperature constant inside the furnace, both ends of the cylinder were covered with thermal insulation. During experiments, metal oxide nanoparticles formed in the particle generator were delivered through the inlet which is positioned parallel to the axial direction of the reactor tube. Meanwhile, hydrocarbon fuel was injected and transferred by carrier gas (nitrogen) from the "side" inlet arranged perpendicularly to the reactor tube. These two influents were then mixed in the high temperature heating zone. Such configuration of injection inlets

prevents pre-condensation of hydrocarbon on the surface of solid particulate matter before they were transferred to the desired temperature zone. In order to minimize the "back-flow" effect, the carrier gas from "side" inlet was maintained at a flow rate which is equal to that of the effluent from the particle generation reactor. Similar to the injection of the metal precursor, a digital syringe pump was also employed to deliver the liquid phase soot precursor into the system with a preset feeding rate. As the temperature inside the droplets is much colder than that in the gaseous phase, which hinders reaction rates,[10] it is necessary to keep the feeding hydrocarbon gaseous for reaction. To do so, the inlet for hydrocarbon (liquid) injection was held at a temperature higher than their melting point, but was slightly lower than their boiling point. This temperature setting allows the injected reactants to be gradually vaporized and transferred to the reaction chamber in the gaseous phase without pre-decomposition.

All the connections should be air-tight during the experiment. Stainless steel Swagelok fittings were used to connect the tubes and the peripherals of the system. Teflon type ferrules were used for most of the connections. However, for connections close to the high temperature area, graphic ferrules were used instead. To avoid damaging the quartz tube inlet/outlet by fittings when assembling the system, all the tube ends were fired-polished.

Particle samples were collected at the outlet of the entrained flow reactor. Depending on the analysis methods, different collection setups were used. HR-TEM was used to investigate the morphology of particulate matter generated in both two reactors. As these effluent particles were of a very small dimension (< 10 nm), a thermal diffusion effect arose for the collection.[11-12] To solve this problem, a "cold-trap" technique was employed based on the fact that high temperature particulate matter is energy favored to condense or deposit on the cold surface. In the experiment, a TEM grid held at the end of a brass-made sample stick was positioned closely at the reactor outlet. During the collection process, the arm of the sample stick was inserted into

the liquid nitrogen to keep the grip temperature as low as 0 ℃. A GC/MS was used to analyze the extraction of carbonaceous particulate matter formed in the hydrocarbon combustor. In order to collect the particulate products quantitatively without causing press build-up in the reactor, its outlet was inserted into a sample vial under ambient atmosphere. During the collection process, the sample vial was cryogenically cooled by placing the arm of the brass-made vial holder into liquid nitrogen.

2.3.3   Experimental Procedure

Since the purpose of this experiment was to investigate the influence of metal oxide nanoparticles on particle growth and soot formation, it is desirable to use metal oxide nanoparticles free of carbonaceous material. Therefore, this first part of this experiment was to determine the optimized conditions for carbonaceous-free metal oxide nanoparticle formation.

Methanolic solutions of fully substituted dendrimer-copper or -iron complexes (G4Me$_{16}$, Me = Cu, Fe) were used as metal oxide precursors and delivered into the flow reactor by a continuous syringe injection. Gas suspended metal oxide nanoparticles were generated through burning of the organic materials of the precursor at temperatures between 500 to 900 °C. During the experiment, the particle generator was maintained at an oxygen rich (> 10 times of stoichiometric combustion) thermal condition to ensure the complete burn-off of the organic materials, leaving metal oxides as the only composition of solid-phase products. The residence time (R.T.) was determined to be 30 to 60 seconds for all experiments to ensure the complete oxidation of metal precursor and methanol, without causing severe aggregation of nanoparticles. For morphology study, effluent particulate matter was collected independently for HR-TEM analysis to confirm the formation of metal oxide nanoparticles and removal of organic materials.

The second part of this experiment was to study the thermal decomposition of hydrocarbon fuel with or without the presence of metal oxide nanoparticles. One of the

advantages of this two-zone reactor design is that the formation of metal oxide nanoparticles could be independently controlled from the combustion of hydrocarbon., In this experiment, the particle generator was set at 700 °C and the carrier gas flow rate was set at 55 cc/min (room temperature) to ensure complete burn-off of all organic materials of the precursor. Metal oxide nanoparticles were introduced to the 2nd reactor chamber by the carrier gas. The hydrocarbon fuel, 1-methyl-naphthalene, was introduced into the reactor at a constant flow rate by using a digital syringe pump for injection and a secondary nitrogen stream as carrier gas.

The ratio of metal to hydrocarbon for reaction could be changed by adjusting the injection rate of 1-methyl-naphthalene or dendrimer-metal methanolic solution. In this experiment, the metal concentration to 1-methyl-naphthalene was maintained at 100ppm on a molar basis[1313].[14] Fuel to air equivalence ratio (C/O) is one of the key parameters affecting the formation of PAH and soot. For C/O = 1, the ratio of oxygen to hydrocarbon corresponds to stoichiometric combustion, in comparison with C/O > 1 and C/O < 1 corresponding to under stoichiometric and over stoichiometric ratios of oxygen to hydrocarbon, respectively. Since a fuel rich (C/O > 1) condition is favored by the occurrence of PAH and soot due to incomplete combustion, C/O values from 1.4 to 5 were used for in this experimental section. To obtain a comparable result, blank tests were performed using the same experimental parameters except replacing the metal precursor as methanolic solution of dendrimer. The relationship of total oxygen input at the inlet of the particle generator and the C/O value used in the hydrocarbon combustor was given in the following expression:

$$C/O = \frac{O_{st.}}{(O_{total} - O_{part.})} \times 100\%$$

Where: C/O is fuel to air equivalence ratio; $O_{st.}$ is the amount of oxygen required for stoichiometric combustion for the injected hydrocarbon fuel; O_{total} is the amount of oxygen input

from the inlet of the particle generator; and $O_{part.}$ is the amount of oxygen consumed by the metal oxide precursor or non-metal precursor and the corresponding methanol solution assuming a stoichiometric combustion.

Collection of the effluent carbonaceous particulate matter from the hydrocarbon combustor for HR-TEM study was similar to the procedure for metal oxide nanoparticle collection. For quantitative studies by GC/MS, carbonaceous particulate matter collected by the "cold-trap" vial was added in an organic solvent (chloroform, methanol, ethanol, dichloromethane, and hexane) and ultrasonically extracted for 20 min. To minimize the collection error, each sample was collected 3 times, at 15 min intervals with new sample vials used. The extraction of the three collections of each sample were combined and condensed to about 0.5 ml by vaporization under inner atmosphere (U.H.P nitrogen) at room temperature. Then the remaining supernate was transferred to a micro vial with a volume scale marker and refilled to 1 ml exactly by the same organic solvent used at the beginning. Finally the extract was centrifuged for 2 min by using a micro-centrifuge (LW Scientific, model ZS-1, 7000r/min), and the top clear liquid was analyzed using the Varian Saturn 3800 GC/MS system, which is equipped with a capillary column (CP-SIL 8CB, 30M x 0.32 mm ID, 0.25 µm film) made by Chrompack. PAH extracted by organic solvent were identified by comparing their mass spectra and retention times with standard spectra in NIST library and standard solution. The quantification of PAH products was based on relative rather than absolute value, due to the non-closed collection system.

2.3.4 Analysis and Calculation

As the collections of soot particles for GC/MS analysis were conducted at an open system, it was impossible to collect all the products in the sample vials. Therefore only relative yields of products could be calculated for the comparison between metal and non-metal

experiments. To do so, the relative total carbon value (TC) of the extractable organic materials from soot particles was calculated using following equation:

$$TC = \sum \frac{P_i}{C_i}$$

Where: P_i is the peak area of products i; C_i is the number of carbon in a molecule of products i. In order to compare the yield of products due to molecular growth, only PAH species with more than 11 carbon atoms in a molecule were counted in the calculation of relative total carbon value, due to the fact that the precursor 1-methylnaphthalene already has 11 carbon atoms in its molecule. Accordingly, the relative yield of PAH product i was given in the following equation, where TC_n is the highest TC values obtained from the reactions of 1-methylnaphthalene combustion.

$$Y_i = \frac{P_i}{TC_h}$$

2.4   Instrumentation Background

2.4.1   HR-TEM

High-resolution TEM (HR-TEM) has been proven to be one of the most useful methods for the characterization of nanoparticles,[14-15] largely due to the small de Broglie wavelength of electrons. Although other available techniques like X-ray or neutron diffraction can provide information about some structural features of the nanoparticles, TEM is unique to provide direct imaging in a real spatial resolution with high magnification.

Basically a TEM can be compared to a slide projector except that the illumination source of TEM is electron rather than light. The transmitted beam is projected onto a phosphor screen for the user to see. When the electron beam is generated and transmitted through the very thin specimen slice, it is affected by the structure and composition of the sample which has been

targeted. The brightness of a particulate area of the image is proportional to the number of electrons that have transmitted through the sample.

A modern TEM is a sophisticated viewing system composed of several components, which include an illumination system, a specimen stage, an imaging system, and a chemical analysis system.[16] From the top down, an electron emission source is the heart of the illumination system which emits electrons into the vacuum. With the presence of condenser lens on the upper column, a fine electron beam can be controlled at desired size and location for sample analysis. To achieve optimized images, which require the uninterrupted passage of electrons, TEM has to be operated under ultra high vacuum with pressures as low as $10^{-5} \sim 10^{-8}$ torr. The specimen stage and sample holder are designed for in-situ observation and analysis with the selection of different regions of interest. In the imaging system, objective lens forms an image on the phosphorescent viewing screen or the camera that used to record the image, while the intermediate and projector lens are functioning as the magnifier.

A built-in chemical analysis system is an energy dispersive x-ray spectroscope (EDS) or electron energy-loss spectroscope (EELS), which is attached on the side of the TEM column to provide quantified information of the chemical composition of the specimen. **Figure 2.6** illustrates the schematic structure of a transmission electron microscope.

2.4.2 XPS

XPS, also known as electron spectroscopy for chemical analysis (ESCA), is a standard technique in catalyst characterization.[17-19] XPS is a highly surface sensitive technique which can provide information from the top 1-10 nm of materials. When a mono-energetic X-ray beam irradiates on the sample, the core electron (i.e. electrons that play no significant in chemical interaction) in the surface atom can absorb the energy of the photon and then escape out of the
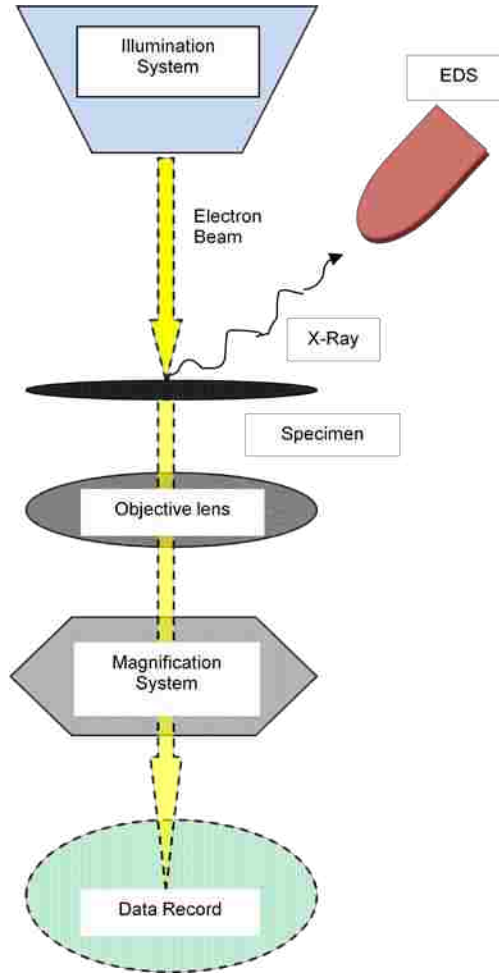
Figure 2.6 Schematic structure of a transmission electron microscope

sample with kinetic energy KE, which can be measured by the energy analyzer. **Figure 2.7** illustrates the process of photoelectronic emission.

As the energy of the X-ray photon is pre-determined by the emitting source and wave length, the binding energy BE of the core electron can be calculated according to the Einstein relationship:

$$BE = h\nu - KE - \emptyset$$

Where $h\nu$ is the energy of the used x-ray photon, Φ is the work function associated with the spectrometer. Binding energy, which represents the strength of interaction between the electron and nuclear charge, is characteristic to each element except hydrogen and helium. BE is

very sensitive to the chemical environment of elements, resulting an "energy shift" (1~10 eV) of the corresponding XPS peak. Therefore, the measurement of BE can provide valuable information of the sample, including elemental identification, chemical state, coordination (types of ligand, number, stereo-conformation). As the number of the emitted photoelectrons is proportional to the atomic concentration of that element in the sample, BE is also used to quantify the chemical composition.
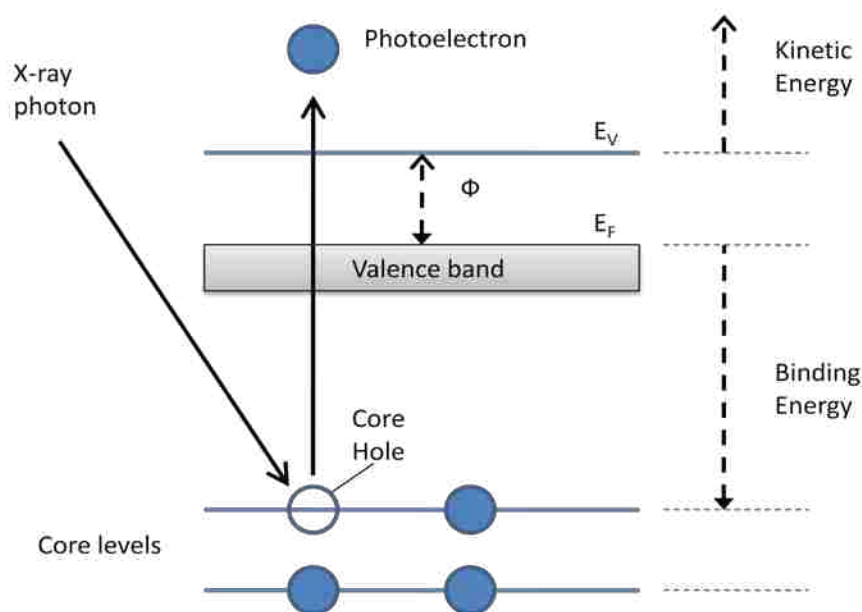

Figure 2.7 Schematic representation of generating a photoelectron from an atom

2.5 References

1.   Alderman, S. L.; Dellinger, B., FTIR investigation of 2-chlorophenol chemisorption on a silica surface from 200 to 500 degrees C. *J Phys Chem A* **2005,** 109, (34), 7725-7731.

2.   Bosman, A. W.; Schenning, A. P. H. J.; Janssen, R. A. J.; Meijer, E. W., Well-defined metallodendrimers by site-specific complexation. *Chem Ber-Recl* **1997,** 130, (6), 725-728.

3.   Floriano, P. N.; Noble, C. O.; Schoonmaker, J. M.; Poliakoff, E. D.; McCarley, R. L., Cu(0) nanoclusters derived from poly(propylene imine) dendrimer complexes of CU(II). *Journal of the American Chemical Society* **2001,** 123, (43), 10545-10553.

4.   Rasband, W. S. *ImageJ*, U.S. National Institutes of Health, Bethesda, MD, USA, 2007.

5.   Igathinathane, C.; Pordesimo, L. O.; Columbus, E. P.; Batchelor, W. D.; Methuku, S. R., Shape identification and particles size distribution from basic shape parameters using ImageJ. *Computers and Electronics in Agriculture* **2008,** 63, (2), 168-182.

6.   Ressler, T., WinXAS: a program for X-ray absorption spectroscopy data analysis under MS-Windows. *Journal of Synchrotron Radiation* **1998,** 5, 118-122.

7.   Stieglitz, L.; Vogg, H.; Zwick, G.; Beck, J.; Bautz, H., On Formation Conditions of Organohalogen Compounds from Particulate Carbon of Fly-Ash. *Chemosphere* **1991,** 23, (8-10), 1255-1264.

8.   Rubey, W. A.; Grant, R. A., Design Aspects of a Modular Instrumentation System for Thermal Diagnostic Studies. *Review of Scientific Instruments* **1988,** 59, (2), 265-269.

9.   Striebich, R. C.; Rubey, W. A.; Tirey, D. A., The thermal decomposition of various organic materials using the system for thermal diagnostic studies (STDS). *Int. SAMPE Environ. Conf. FIELD Full Journal Title:International SAMPE Environmental Conference* **1991,** 1, (Environment in the 1990's: A Global Concern), 155-62.

10.   Marsh, N. D.; Zhu, D.; Wornat, M. J., Pyrolysis product absorption by burning benzene droplets. *Symp. (Int.) Combust., [Proc.] FIELD Full Journal Title:Symposium (International) on Combustion, [Proceedings]* **1998,** 27th, (Vol. 2), 1897-1905.

11.   Langer, G. Particle impactor assembly for size selective high volume air sampler. 87-28981
4764186, 19870323., 1988.

12.   Van Gulijk, C.; Marijnissen, J. C. M.; Makkee, M.; Moulijn, J. A.; Schmidt-Ott, A., Measuring diesel soot with a scanning mobility particle sizer and an electrical low-pressure impactor: performance assessment with a model for fractal-like agglomerates. *Journal of Aerosol Science* **2004,** 35, (5), 633-655.

13.   Feitelberg, A. S.; Longwell, J. P.; Sarofim, A. F., Metal Enhanced Soot and Pah Formation. *Combustion and Flame* **1993,** 92, (3), 241-253.

14.   Helveg, S.; Hansen, P. L., Atomic-scale studies of metallic nanocluster catalysts by in situ high-resolution transmission electron microscopy. *Catalysis Today* **2006,** 111, (1-2), 68-73.

15.   Allard, L. F.; Panjabi, G. A.; Salvi, S. N.; Gates, B. C., Imaging of nearly uniform Os5C clusters dispersed on MgO powder. *Nano Letters* **2002,** 2, (4), 381-384.

16.   B.Fultz; J.M.Howe, *Transmission Electron Microscopy and Diffractometry of Materials*. Springer: Heidelberg, Germany, 2005.

17.   Jose A. Rodriguez; Jae Y. Kim; Jonathan C. Hanson; Manuel Perez; Frenkel, A. I., Reduction of CuO in H2: in situ time-resolved XRD studies. *Catalysis Letters* **2003,** 85, 247-254.

18.   Francisco, M. S. P.; Mastelaro, V. R.; Nascente, P. A. P.; Florentino, A. O., Activity and characterization by XPS, HR-TEM, Raman spectroscopy, and BET surface area of CuO/CeO2-TiO2 catalysts. *Journal of Physical Chemistry B* **2001,** 105, (43), 10515-10522.

19.   Fierro, G.; Lo Jacono, M.; Inversi, M.; Dragone, R.; Porta, P., TPR and XPS study of cobalt-copper mixed oxide catalysts: evidence of a strong Co-Cu interaction. *Topics in Catalysis* **2000,** 10, (1-2), 39-48.

CHAPTER III: RESULTS

A series of advanced scientific instruments have been used in the research described here. High-resolution transmission electron microscopy (HR-TEM) was chosen to conduct the morphology analysis of the synthetic nanoparticles. Chemical composition was determined by X-ray photoelectron spectroscopy (XPS) with regard to the concentration and oxidation state of elements on the particle surface. A System for Thermal Diagnostic Studies (STDS) was used to perform the catalysis tests of the prepared metal oxide nanoparticles and impregnated coarse particles. A two-zone high temperature flow reactor was designed and built for producing gas-suspended metal oxide nanoparticles as well as soot-like particulate matter. Morphology of the combustion generated particulate matter and their extractable composition was investigated using TEM and GC/MS, respectively.

3.1   Synthesis of Metal Oxide Nanoclusters

3.1.1   The Effect of Calcination Temperatures on Surface Composition

In order to find out the minimum temperature of calcination at which the dendrimer backbone could be burned off completely on the silica substrate, a series of silica samples impregnated with $G4Cu(II)_{16}$ were prepared and calcined at different temperatures varying from 250 to 450 ºC. The chemical composition of each sample obtained from XPS experiments is presented in **Table 3.1**.

The concentration of oxygen remained nearly constant at ~50% in all temperatures that were tested. Nitrogen and carbon, the major components of dendrimer, both decreased continuously when the calcination temperature were increased, and became undetectable at 350 ºC for nitrogen and 450 ºC for carbon. The surface concentration of copper species was 1.86% for the uncalcined sample and decreased from 1.46% to 0.43% as the calcination temperature

increased from 250 ℃ to 450 ℃. The percentage of silica elevated from 34% to 50% with the

increase in temperature.

Table 3.1 Suface composition (elemental wt.%) by XPS method of G4Cu(II)16 supported
on silica and calcined under different temperatures

Element	Calcination Temperature					
	Uncalcined*	250 °C	300 °C	350 °C	400 °C	450 °C
Carbon	13.18	2.21	0.98	0.82	0.28	<0.01
Nitrogen	3.51	0.92	0.27	n.d.	n.d.	n.d.
Oxygen	47.73	52.04	55.13	44.83	42.80	49.20
Copper	1.86	1.46	1.20	0.72	0.52	0.43
Silicon	33.72	43.37	42.42	53.62	56.40	50.4

*All samples were dried at 120 ℃ and then calcined at a prescribed temperature for 5
hours
** n.d. refers to none detected; the limits of detection for nitrogen are 0.01~0.1% for the

3.1.2   Determination of Oxidation State of Metal in Calcined Sample

XANES analysis was employed to study the oxidation state of copper calcined at 450 ℃.

Silica-supported copper oxide nanoclusters prepared using $G4Cu(II)_{16}$ as a precursor were

compared to the Cu(II) and Cu(I) standard samples. **Figure 3.1** depicts the XANES transmission

spectra obtained from various copper oxide samples: a) 5 wt.% $G4Cu_{16}$/silica calcined at 450

℃, and reference standards of 20 wt.% (b) Cu(II)O and (c) Cu(I)O mechanically mixed with

silica. In the pre-edge zone, the calcined $G4Cu_{16}$ sample show no peaks, in comparison to a weak

peak at 8.984 keV and a strong peak at 8.9801 keV for reference standards of Cu(II)O and

Cu(I)O, respectively.   Another reading of the edge energy was conducted at the maximum

adsorption.   The position of adsorption peak was 8.999 keV for both $G4Cu_{16}$ and standard

Cu(II)O samples, and 8.996 keV for standard Cu(I)O. From the view of the near-post-edge, the

calcined $G4Cu_{16}$ sample did not show the feature peaks at 9.012 keV which was presented in
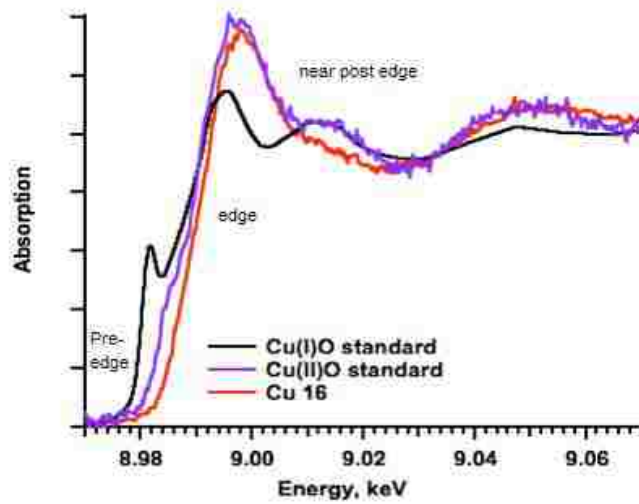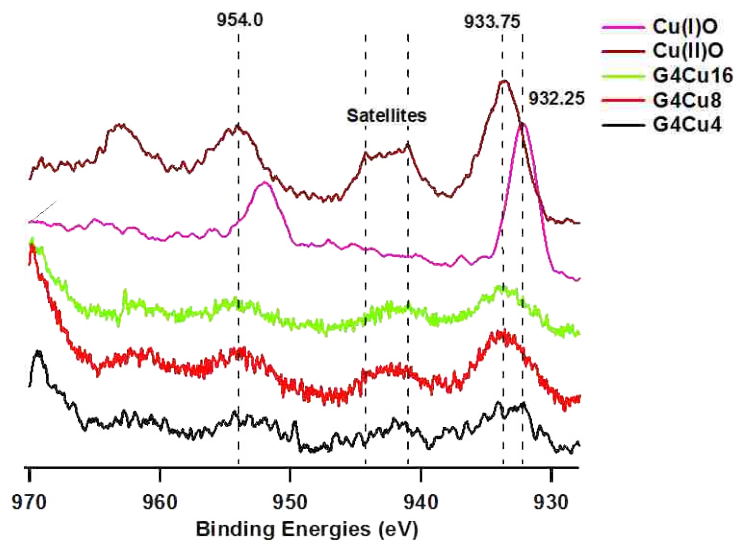
both Cu(II)O and Cu(I)O standard references.

Figure 3.1 XANES spectra of the CuO nanoclusters supported on silica (5 wt.% CuO/silica) in comparison with Cu(I)O and Cu(II)O standards

In addition to XANES, XPS analysis was also used to identify the oxidation states of metal in the nanoclusters samples. Copper oxide nanoclusters were prepared by the calcined samples of $G4Cu_n$/silica (n=16, 8, 4) and all reference samples were used as received from venders (>99%). XPS spectra of copper in these nanoclusters and reference samples are depicted in **Figure 3.2** over the binding energy range of 928 to 970 eV.

Figure 3.2 XPS spectra of the CuO nanoclusters supported on silica (5 wt.% CuO/silica) compared to Cu(I)O and Cu(II)O standards

61

In the spectrum of the Cu(II)O reference sample, 2 major peaks at 954.0 and a 933.8 eV and a group of intense satellite peaks at 940-945 eV were observed. For the Cu(I)O standard sample, the two major peaks were lined at 952.2 and 932.3 eV, respectively. In contrast to Cu(II)O, no satellite peaks were observed at the energy range of 940-945 eV. All the XPS spectra of the three nanocluster samples of $G4Cu_{16}$, $G4Cu_8$, and $G4Cu_4$ exhibited two major peaks at the same position of 954.0 and 933.8 eV, though the $G4Cu_4$ possessed an additional peak at 932.3 eV. Satellite peaks were also observed at 939-946 eV for all three nanocluster samples.

XPS spectra of iron oxide samples are depicted in **Figure 3.3**, including the standard references of ferric oxide (Fe_2O_3) and ferrous oxide (FeO), and three calcined samples of $G4Fe_n$ (n=16, 8, 4). For the Fe_2O_3 sample, 2 major peaks at 710.2 and 724.3 eV, as well as an intense satellite peak at 718.6 eV were observed. The XPS spectrum of FeO was similar to the Fe_2O_3 sample with 2 major peaks at 710.2 and 724.2 eV, respectively. A broad satellite peak was also observed at 716-720 eV. Three iron oxide nanocluster samples of $G4Fe_n$ (n=16, 8, 4) all exhibited two major peaks at the same position of 710.2 and 724.3 eV respectively. Weak satellite peaks at 715-721 eV were observed in the spectra of $G4Fe_{16}$ and $G4Fe_4$, but not in the spectrum of $G4Fe_8$. It should be noted that the present spectra of Fe_2O_3 and FeO reference samples were shifted 2.0 eV and 1.25 eV to the higher energy side from their original data, respectively, based on the calibration of the carbon peak. This energy shift was due to the result of charging of the oxides when their reference spectra were taken.[1]

XPS spectra for nickel oxide samples were depicted in **Figure 3.4**. The reference standard, NiO, exhibited two major peaks at 854.1 and 873.0 eV. Two intense satellite peaks were observed at 856.2 and 861.2 eV. All three calcined $G4Ni_n$ (n=16, 8, 4) possessed the same

two major peaks at 855.1 and 872.3 eV respectively. Weak but broad satellite peaks at 859-863 eV were identified in the spectra of all three G4Ni$_n$ samples as well.
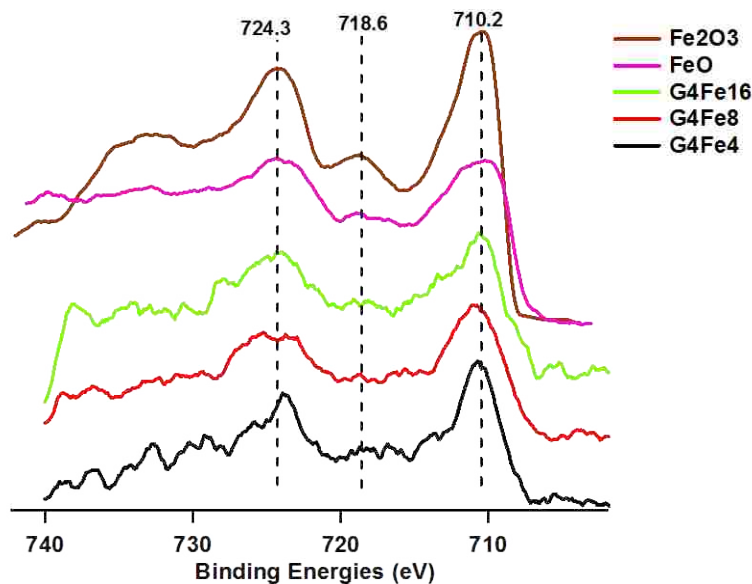

Figure 3.3 XPS spectra of the iron oxide nanoclusters supported on silica (5 wt.% Fe$_2$O$_3$/silica) compared to Fe$_2$O$_3$ standards
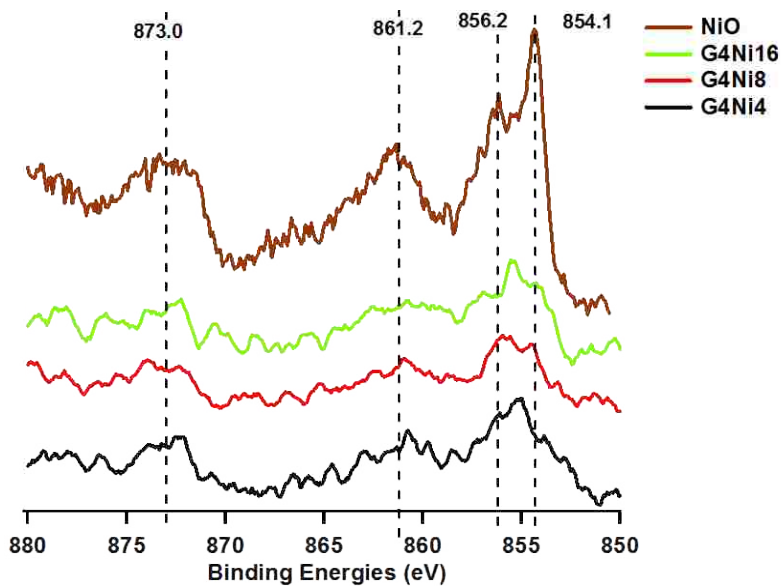

Figure 3.4 XPS spectra of the nickel oxide nanoclusters supported on silica (5 wt.% NiO/silica) compared to Ni(II)O standards

3.1.3 Size-controlled Approaches in Synthesis with Morphology Studies

3.1.3.1 The Effect of Substitution Degree of Dendrimer

Morphology of supported metal oxide nanoclusters that prepared was investigated using the JEOL 2010 HR-TEM. The initial approach to control the size of supported metal oxide nanoparticles was accomplished by changing the metal/dendrimer ratio in the solutions of the precursor. In the case of copper, these precursors were $G4Cu(II)_{16}$, $G4Cu(II)_8$, and $G4Cu(II)_4$, which stands for fully, half and quarter substituted dendrimer-copper complexes. Amorphous silica powder (Cab-O-Sil) was chosen as a solid substrate in the amount corresponding to 5 wt.% metal oxide loading. For references, blank Cab-O-Sil and uncalcined $G4Cu(II)_{16}$/Cab-O-Sil were also imaged using TEM, which were shown in **Figure 3.5 (a) and (b), respectively. In these images,** the darker gray area stands for the silica powder and the light gray area is for the carbon support film coated the TEM grid. **However, no** nano-size clusters of CuO were found on these samples.

| (a) | (b) |
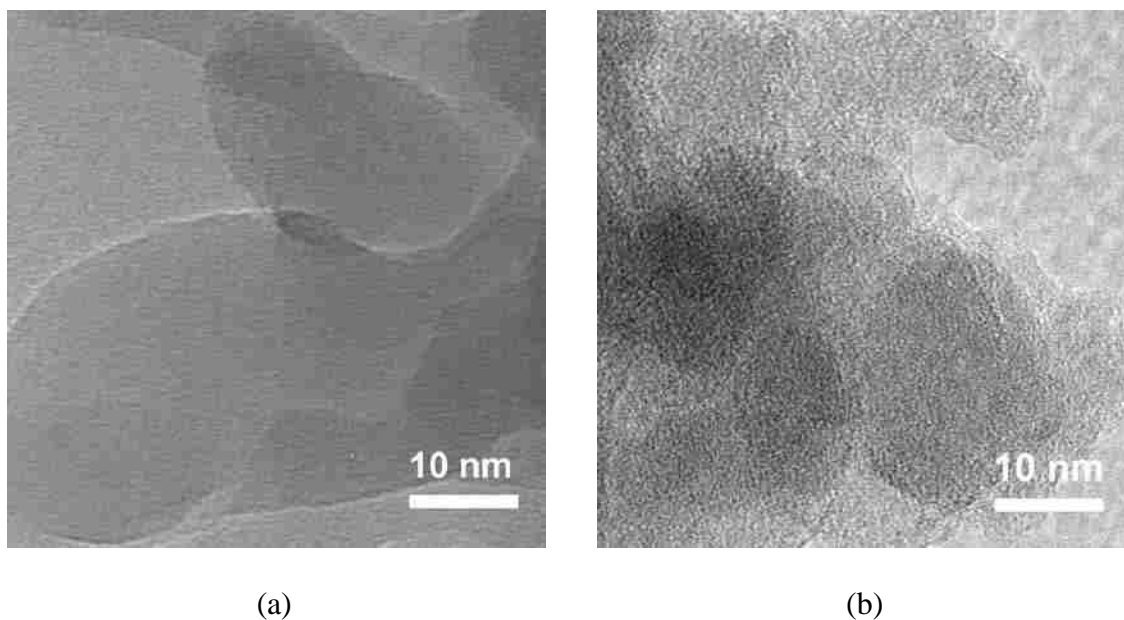
Figure 3.5 HRTEM micrographs of (a) blank Cab-O-Sil, and (b) uncalcined
$G4Cu(II)_{16}$/Cab-O-Sil

Figure 3.6 presents the TEM micrographs of the silica after impregnation with dendrimer-Cu(II) complexes followed by thermal oxidation at 450 °C. The appearance of the dark spots on the gray SiO_2 background after the oxidation of deposited dendrimer-metal complex indicates the formation of metal oxide nanoclusters. Uncalcined samples, though the micrographs are not shown here, did not yield the dark spots on the silica surface. Particle size distribution of the metal oxide nanocluster samples was obtained using Igor for statistical data treatment (see **Chapter 2.1**). For calcined $G4Cu_n$ samples, the particle sizes of copper oxide nanoclusters were 3.27±0.24 nm, 2.37±0.34 nm, and 1.68±0.69 nm for n=16, 8, 4, respectively.

Similar procedures were applied to prepare supported iron oxide and nickel oxide nanoclusters from their respective dendrimer-metal complexed with different substitution levels. The TEM micrographs and size distributions were presented in **Appendix 1-A**. Ni(II) was reported to coordinate with the amino ending groups of dendrimer in a ratio up to 1:2,[2] which enabled a DAB-Am_{32} (G4) dendrimer molecule to complex with 16, 8 and 4 Ni(II) ions for full, half and quarter substitution, respectively. For calcined $G4Ni_n$ samples (5 wt.% NiO loading on silica), particle sizes of nickel oxide nanoclusters were obtained from Igor results as 3.03±0.40 nm, 2.58±0.29 nm, and 1.83±0.27 nm for n =16, 8, 4, respectively.

Using the dendrimer/metal ratio to calculate the substitution degree of dendrimer was not as simple in the case of Fe(III). To exploit the possible maximum coordination numbers of Fe(III) with the amino ending groups of G4 dendrimer, the ratios of iron ions to dendrimer were selected as n = 16, 11, 8 and 4. Particle sizes of the iron oxide nanoclusters obtained from the calcination of $G4Fe_n$ were 3.07±0.31 nm, 2.79±0.32 nm, 2.60±0.25 nm, and 2.20±0.25 nm for n=16, 11, 8, 4, respectively. The TEM micrographs and size distributions are presented in **Appendix 1-B**.
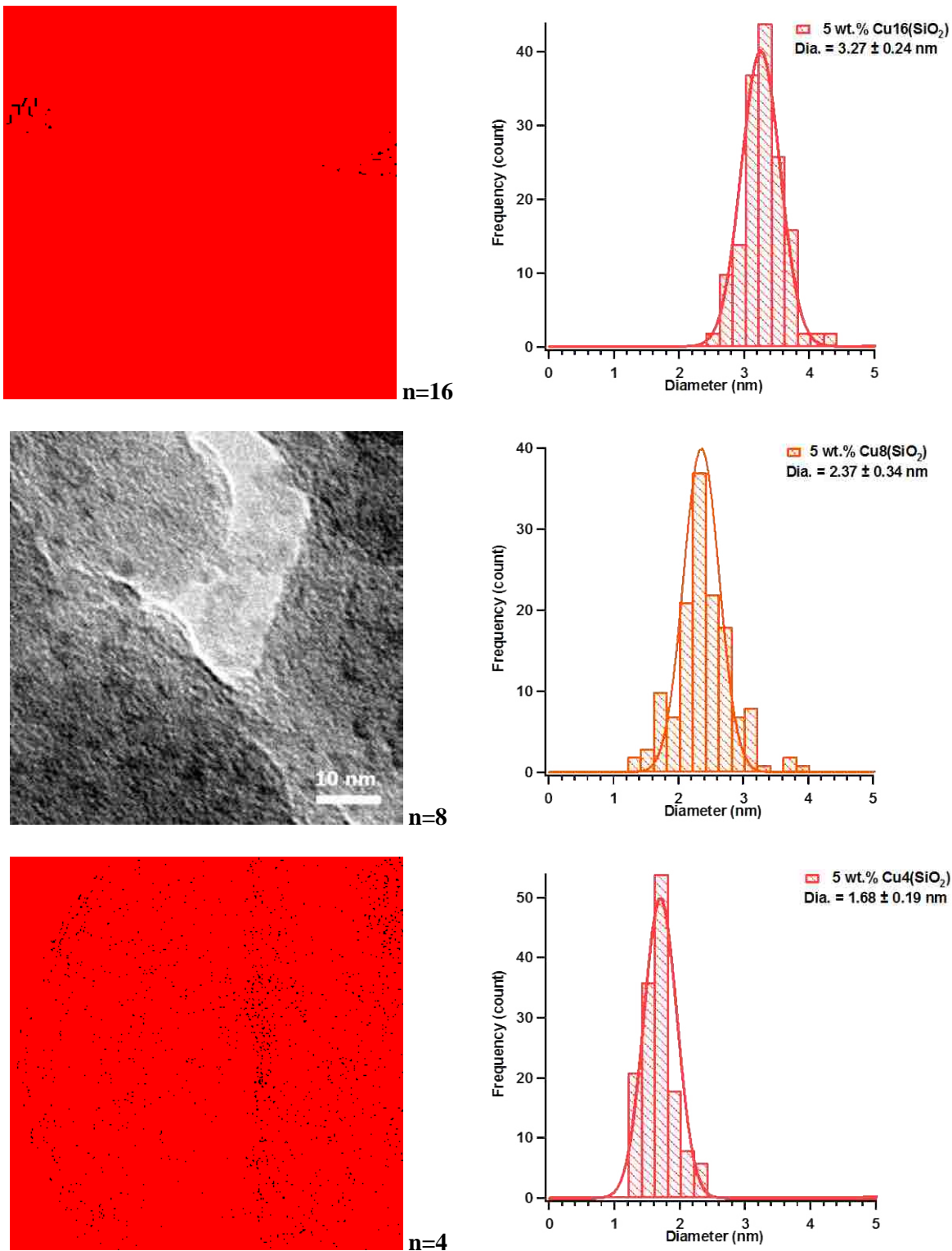
Figure 3.6 HR-TEM micrographs and particle size distribution of CuO nanoclusters supported on silica prepared by calcination (450 ºC, 5hrs) of G4Cu(II)$_n$/silica (n=16, 8, 4)

3.1.3.2 The Effect of Metal Oxide Loading

Studies of particle size as a function of metal oxide loading on silica support were performed. By retaining the same concentration of G4Cu(II)$_{16}$ in precursor solution, the amount of Cab-O-Sil was added accordingly so that the calculated metal oxide loading on silica was reduced to 2 wt.% and 1 wt.%, respectively. Both samples were also calcined at 450 °C for 5 hours. The particle sizes of the copper oxide clusters from these two calcined samples were compared to those of the 5 wt.% sample made previously (**Section 3.1.3.1**) as depicted in **Figure 3.7**. Specifically, particle size of CuO nanoclusters obtained from 1, 2 and 5 wt.% metal oxide loading were 2.40±0.31nm, 2.60±0.34 nm and 3.27±0.24 nm, respectively.
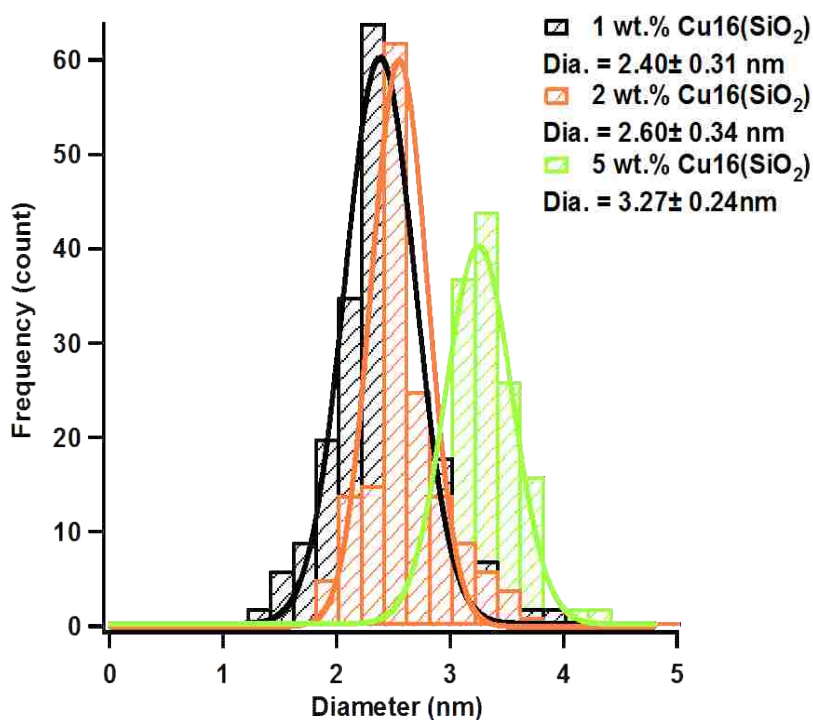
Figure 3.7 Particle size distribution of CuO nanoclusters supported on silica prepared by calcination of G4Cu(II)$_{16}$/silica (1 to 5 wt.% CuO loading)

A similar trend of size reduction with decreasing of metal oxide loading was observed in the case of nickel oxide. G4Ni$_{16}$/silica samples corresponding to the nickel oxide loading of 1

and 2 wt.% on silica were prepared and calcined at 450 °C for 5 hours, resulting in the formation of NiO nanoclusters with sizes of 2.35 ± 0.25 nm and 2.47 ± 0.39 nm, respectively. The particle size of 5 wt.% sample was depicted previously with a reported value of 3.03 ± 0.40 nm. The TEM micrographs and size distributions of these three samples are presented in **Appendix 1-C**.

3.1.3.3   The Effect of "Pre-adsorption" Procedure

In this experimental section, several copper oxide nanocluster samples were prepared using the revised dendrimer-template method with the additional "pre-adsorption" procedure. That is, prior to the deposition of dendrimer/copper complexes on silica support by vaporizing the solvent, the silica substrate was thoroughly impregnated with the precursor solution for 24 hours. Size distribution of copper oxide nanoclusters obtained from samples prepared using this technique is depicted in **Figure 3.8**. For samples with 5 wt.% copper oxide loading, the use of $G4Cu_{16}$ and $G4Cu_8$ as a precursor resulted in the formation of copper oxide nanoclusters with sizes of 2.04 ± 0.25 nm and 1.86 ± 0.17 nm, respectively. $G4Cu_{16}$ was also used to produce copper oxide nanocluster samples with lower metal oxide loadings of 1 and 2 wt.% and resulted in the formation of copper oxide nanoclusters with size of 1.76 ± 0.25nm and 1.55 ± 0.21nm, respectively.

In the side-by-side comparison with those prepared by the regular "non pre-adsorption" procedure, the use of "pre-adsorption" resulted in a significant size reduction of copper oxide nanoclusters. Specifically, there is a 38% decrease for 5 wt.% $G4Cu_{16}$, a 32% decrease for 2 wt.% $G4Cu_{16}$, a 35% decrease for 1 wt.% $G4Cu_{16}$ and a 22% decrease for 5 wt.% $G4Cu_8$. Although EDS analysis indicated the presence of copper associated with the silica, use of the "pre-adsorption" method for the 5 wt.% $G4Cu_4$ sample resulted in no nanoclusters visible under TEM examination.
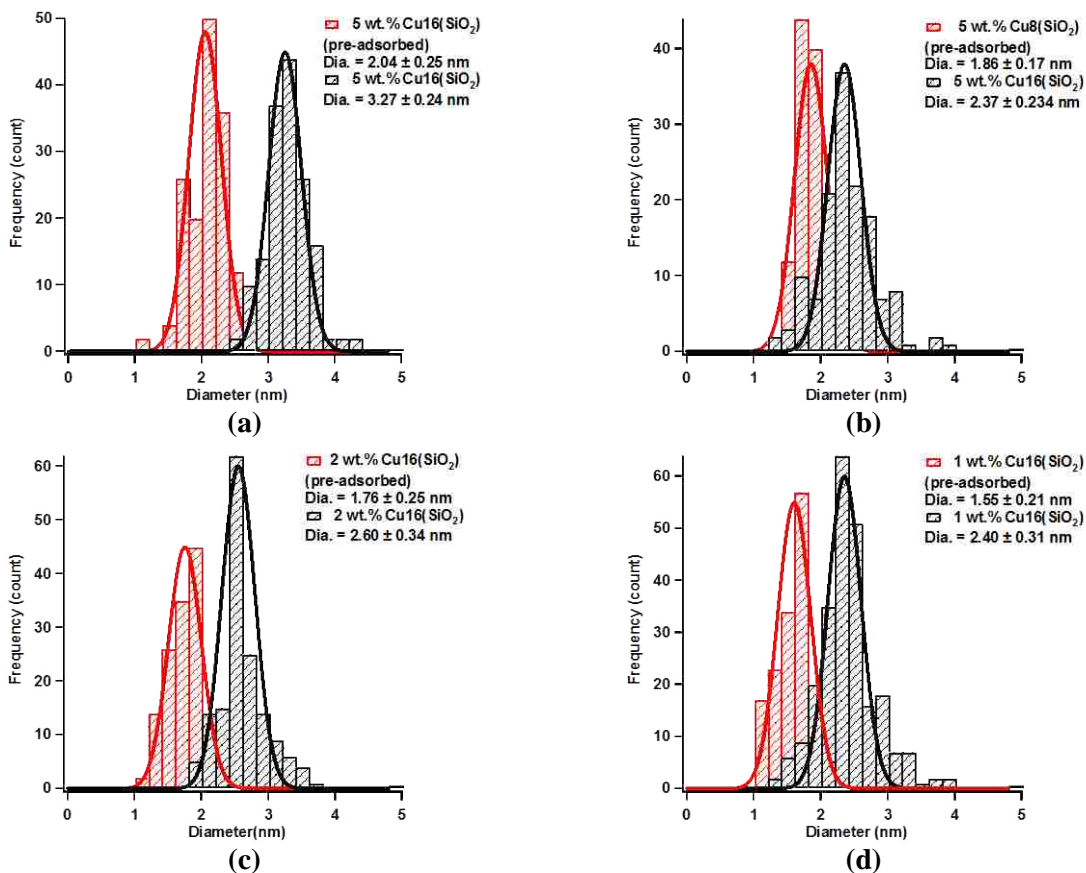
Figure 3.8 Comparison of particle size distribution of supported CuO nanocluster prepared by dendrimer-templates method with and without "pre-adsorption" procedure

3.1.3.4 The Effect of Calcination Temperature (> 450 °C)

In an effort to increase the spectrum of the nanoclusters sizes from the same generation of the dendrimer-metal precursor, the cluster "growing" approach was used. This technique utilized the increasing mobility of nanoclusters with elevating temperatures to increase the cluster size during the calcination process. As seen in **Figure 3.9** and **Table 3.2** (detailed information of size distribution are presented in **Appendix 1-D**, the mean size of CuO clusters shifted from 2.04 to 5.64 nm when the calcination temperature of 5 wt.% G4Cu16(II)/silica was elevated from 450 to 650 °C. It should be mentioned that these samples were treated with the "pre-adsorption" process to minimize the agglomeration of dendrimer before calcination.

69

Table 3.2 Particle size of CuO nanoclusters as a function of calcination temperatures

Sample	Ave. Size of Nanoclusters (nm)		Std. Deviation (nm)
	Calcination temp (°C)	Mean diameter (nm)	
1 wt.% G4Cu16(II)/Silica	450	1.55	0.21
1 wt.% G4Cu16(II)/Silica	550	1.84	0.55
1 wt.% G4Cu16(II)/Silica	600	2.09	0.76
5 wt.% G4Cu16(II)/Silica	450	2.04	0.25
5 wt.% G4Cu16(II)/Silica	550	3.17	0.71
5 wt.% G4Cu16(II)/Silica	600	4.09	1.59
5 wt.% G4Cu16(II)/Silica	650	5.64	2.52

Although the calcination temperature did show a significant impact on the clusters sizes of 5 wt.% copper oxide samples, which percentage increase were ~55% for ~550 °C, ~100% for 600 °C and ~180% for 650 °C when compared to 450 °C, this was not the case for samples with lower metal oxide loading. Specifically, for 1 wt.% copper oxide samples, increasing calcination temperature from 450 °C to 550 °C and 600 °C only resulted in ~17% and ~28% increase of the sizes of copper oxide nanoclusters, respectively.

(a)   (b)
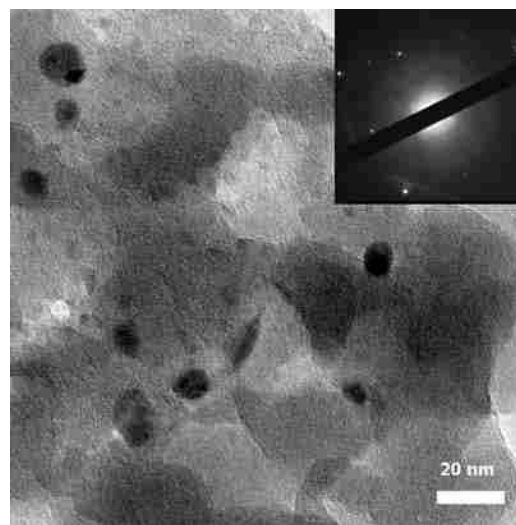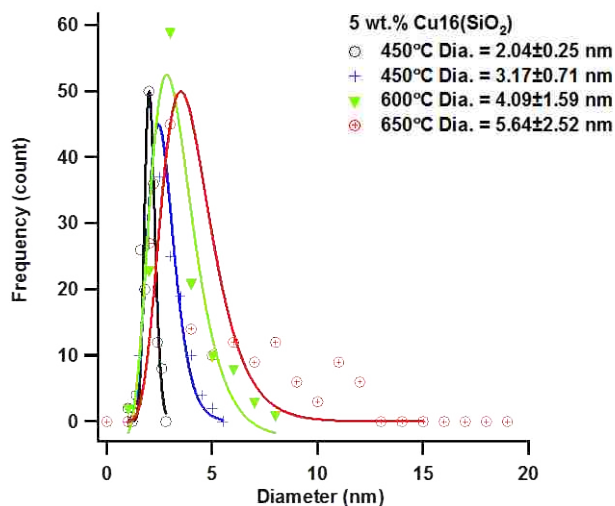
Figure 3.9 (a) Comparison of the CuO cluster size supported on silica achieved from the calcinations of 5 wt.% G4Cu (II)$_{16}$/silica at various temperatures (450 to 650 °C). **(b)** Crystalline-like CuO nanoclusters were easily found in sample calcined at 650 °C (diffraction pattern image taken at a large CuO cluster > 10 nm)

3.1.3.5 The Effect of Supporting Substrates

To explore the universal application of this dendrimer based method for nanocluster fabrication, we have extended our technique to other supports in addition to Cab-O-Sil silica. Sub-micron size titanium oxide particles were therefore selected as the supporting substrate for copper oxide nanoclusters, which were produced using the same "pre-adsorption" procedure for silica samples. The calcination of G4Cu(II)$_{16}$/TiO$_2$ (5 wt.%) at 450 °C resulted in the formation of copper oxide nanoclusters with a size of 2.20±0.25 nm (c.f. **Figure 3.10**).
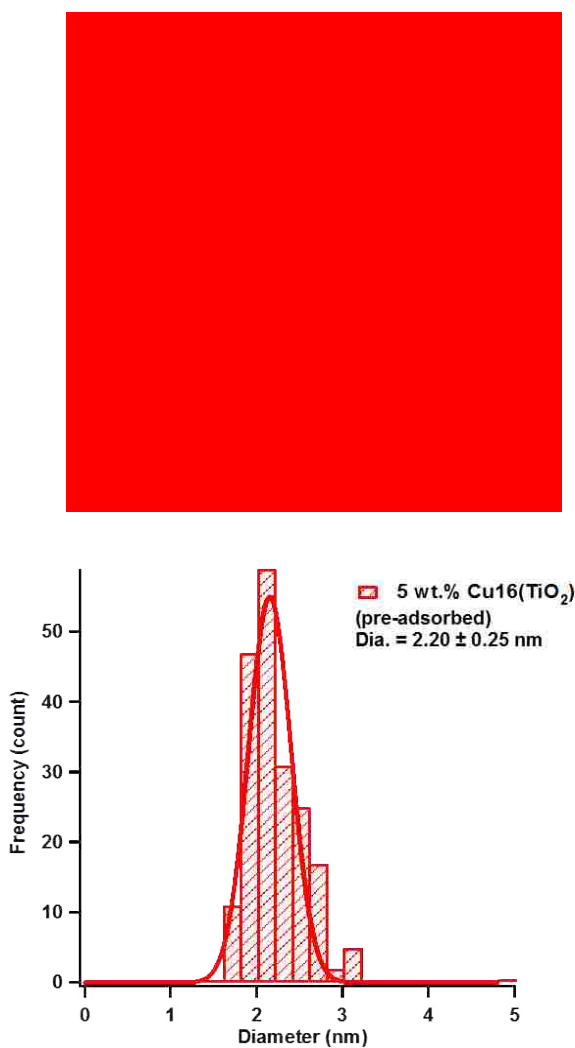
Figure 3.10 Copper oxide nanoclusters supported on Titania using "pre-adsorption" method for 5 wt.% G4Cu(II)$_{16}$/silica

71

3.2 Thermal Decomposition of Chlorinated Benzenes over Different Size Metal Oxide (Particles) Catalysts

3.2.1 Preparation of Catalysts and Blank Test

In this catalysis experiments, the candidate of nano-size catalysts were prepared by the dendrimer-based method. According to the substitution degree of dendrimer in precursor, these samples were labeled as $G4Me_n$ (Me = Cu, Fe, n = 16, 8, 4). Based on the experimental results presented in **Chapter 3.1**, the size distribution of these metal oxide clusters was ranged from 1-4 nm, as listed in **Table 3.3** Brief label and composition of catalysts studied. The surrogate of coarse metal oxide particles was prepared using the traditional incipient wetness impregnation method. As indicated by the TEM micrographs shown in **Figure 3.11**, "giant" clusters with size as large as several hundred nanometers are not rare anymore. With their sizes varied widely from several to several hundred nanometers, it is impossible to obtain a meaningful size distribution of these samples. Similar phenomenon of uniform "giant" clusters of iron oxide catalysts prepared by impregnation method is expected. In fact, XRD analysis of both impregnated CuO and Fe2O3 show strong crystalline peaks in their spectra, which is not the case in their nano-size analogues (**Appendix 3**). All the catalysts were pre-activated (400 ºC, 1 hour, and ambient atmosphere) within 12 hours of the catalysis test. This procedure was to remove the potential surface adsorbed water vapor and organics during storage. **Table 3.1Table 3.3** summarizes the catalysts used in this experiment.

Before determining the catalytic activity of substrate-supported metal oxide clusters, it is necessary to run the blank tests, including both empty reactor and pure substrate (Cab-O-Sil silica) under the same reaction condition for catalysis test. **Figure 3.12(a)** shows the conversion of o-DCBz under pyrolytic and oxidative condition at temperature from 250 to 550 ºC. **Figure 3.12(b)** shows the conversion of MCBz under pyrolytic and oxidative condition at temperature

from 300 to 550 ℃. At the highest reaction temperature of 550 ℃, there was only 8% o-DCBz and 4% MCBz being converted. Furthermore, except for the reactants o-DCBz and MCBz, no other products were detected in the blank tests.
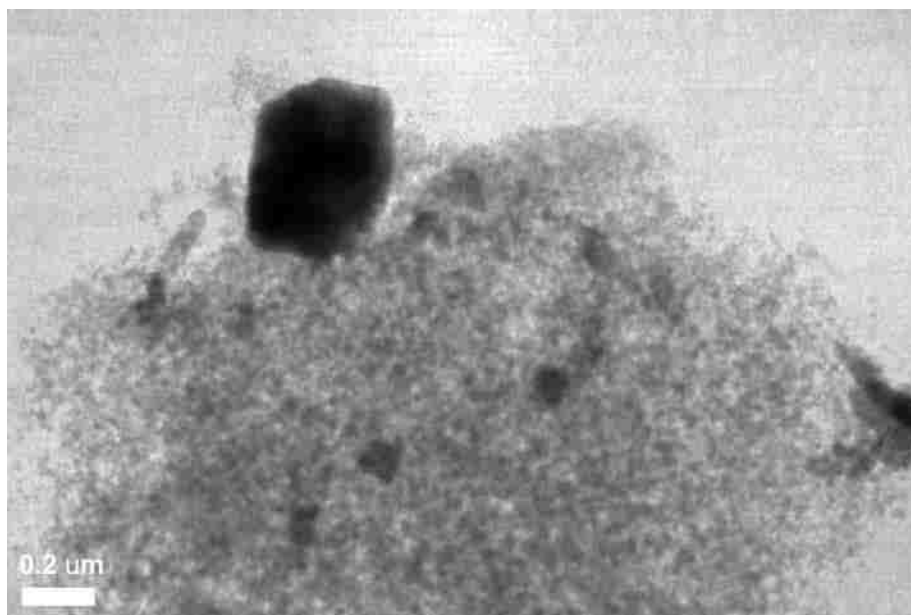

Figure 3.11 Silica supported copper oxide catalysts prepared by incipient wetness impregnation method

Table 3.3 Brief label and composition of catalysts studied

Catalysts	Preparation Method	Me[*]/G4 Molar Ratio	% M_xO_y[**]	Size (nm)
G4Cu$_{16}$	Dendrimer-Template	16	4.93	3.3
G4Cu$_8$	Dendrimer-Template	8	4.87	2.4
G4Cu$_4$	Dendrimer-Template	4	5.11	1.7
ImpCu	Impregnation	-	4.97	1~1000
G4Fe$_{16}$	Dendrimer-Template	16	4.79	3.1
G4Fe$_8$	Dendrimer-Template	8	5.08	2.6
G4Fe$_4$	Dendrimer-Template	4	4.95	2.2
ImpFe	Impregnation	-	5.13	1~1000
Blank[***]	-	-	0	-

*   Metal ion (Cu^{2+} or Fe^{3+})
**   Metal oxide loading (wt.% M_xO_y) on silica support (ICP-MS Results)
***   Non-metal contained Cab-O-Sil®
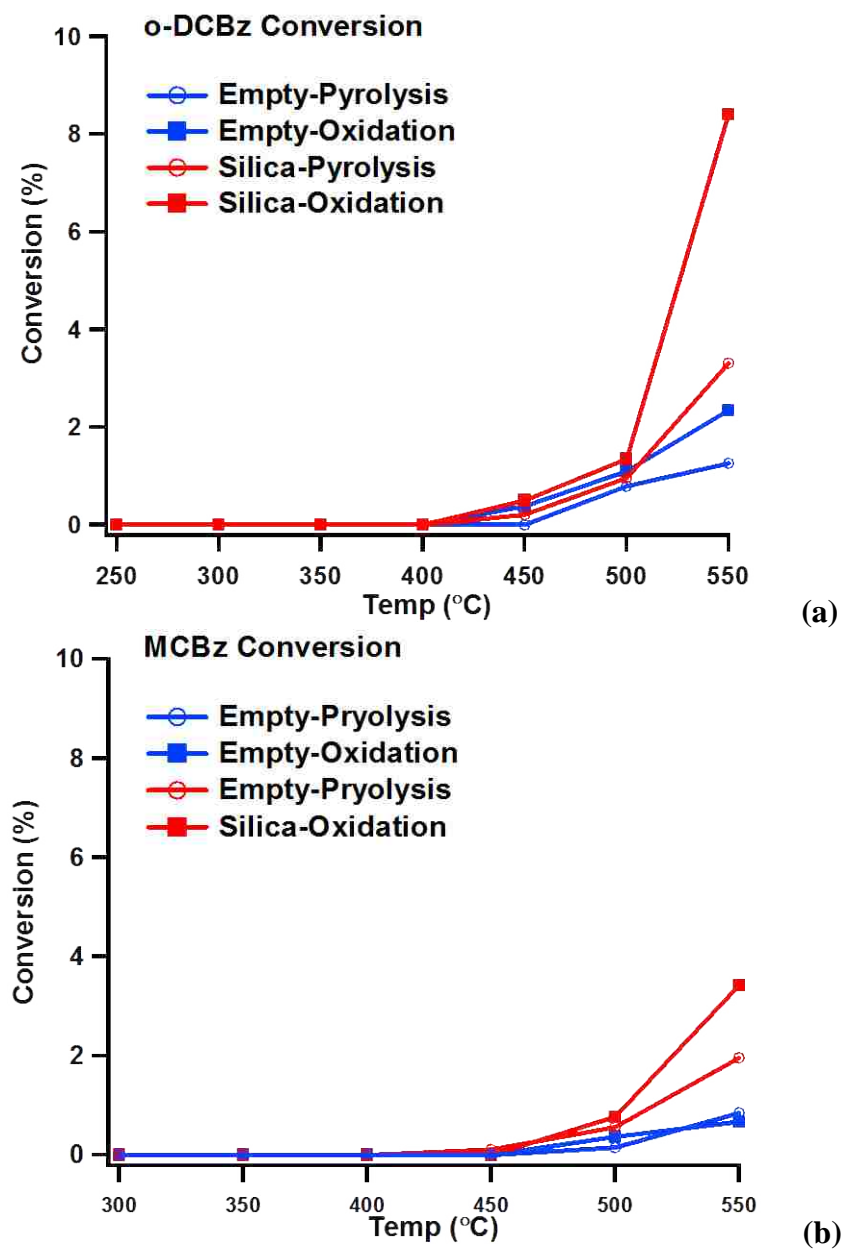
Figure 3.12 Conversion of (a) 1,2-dichlorobenzene and (b) monochlorobenzene in the blank test

3.2.2 Copper Catalyzed Decomposition (Pyrolysis) of 1,2-Dichlorobenzene

The conversion of o-DCBz over the various copper oxide catalysts (5 wt% metal oxide loading) supported on powder formed silica (Cab-O-Sil) under pyrolytic condition is depicted in **Figure 3.13** as a function of the reaction temperature. At 350 ºC more than 50% o-DCBz was

converted over calcined G4Cu(II)$_n$ catalyst while only 13% for the IMPCu sample. At 450 ºC the average conversion of o-DCBz over the G4Cu$_n$ was 88% (88.4% for G4Cu16, 94.1% for G4Cu8 and 81.4% for G4Cu4) while only 46% for IMPCu. At 550 ºC almost 100% conversion of o-DCBz was achieved in all cases.

Pyrolysis of o-DCBz produced various hydrocarbon species. **Table 3.4** summarizes the yield of each product from the reactions over two different types of catalysts: Coarse and Nano, which are referred to catalysts prepared by incipient wetness dendrimer-template method, respectively. It should be noted that the values for the Nano case were given as the average of those from all three G4Cu(II)$_n$ cases. Such averaging treatment was also employed in all other catalysis experiments. Detail information of products yield over each catalyst is presented in **Appendix 2-A.**

The formation of benzene (Bz) and monochlorobenzene (MCBz) over G4Cu$_n$ catalysts achieved their maximum yields as 1.6% at 500 ºC and 0.57% at 350ºC, respectively. In the IMPCu case, the maximum yields were 0.081% at 500ºC for Bz and 0.20% at 400ºC for MCBz. The yield of benzofuran (BF) achieved its maximum at 0.10% at 400ºC for G4Cu$_n$ and 0.023% at 450ºC for IMPCu. Phenol was formed with a maximum yield of 0.22% at 350ºC in the case of G4Cu$_n$ and 0.013% at 400ºC in the IMPCu case. The formation of trichlorobenzene (1,2,3+1,2,4-TriCBz) reached maximum yields at 350ºC in both cases of G4Cu$_n$ (0.066%) and IMPCu (0.11%). Naphthalene (NP) and biphenyl (BP) formed in the case of G4Cu$_n$ were observed with maximum yields of 0.012% at 350 ºC and 0.076%ºC at 400 ºC, respectively, in comparison to 0.0021% at 400 ºC and 0.011% at 350 ºC for IMPCu. Dibenzofuran (DF) was the only consistently observed PCDD/Fs product in this series of experiments. It was maximally formed at 0.16% at 450ºC over G4Cu$_n$ while only 0.018% at 350 ºC in the IMPCu case.
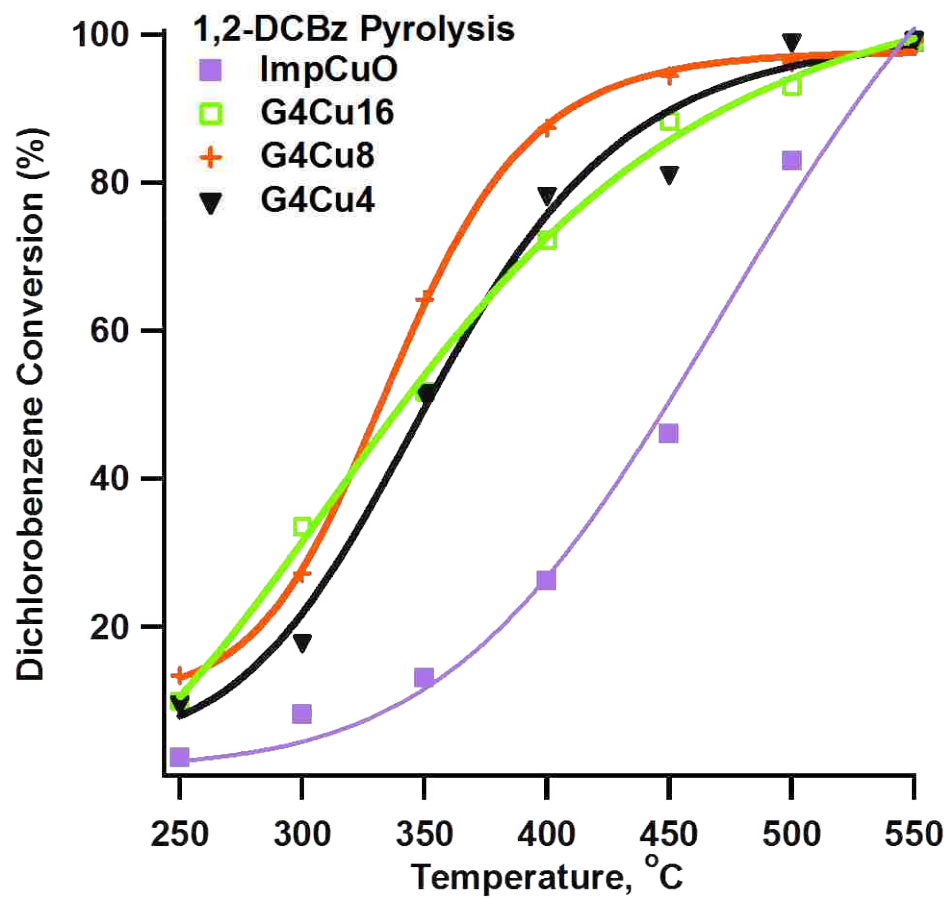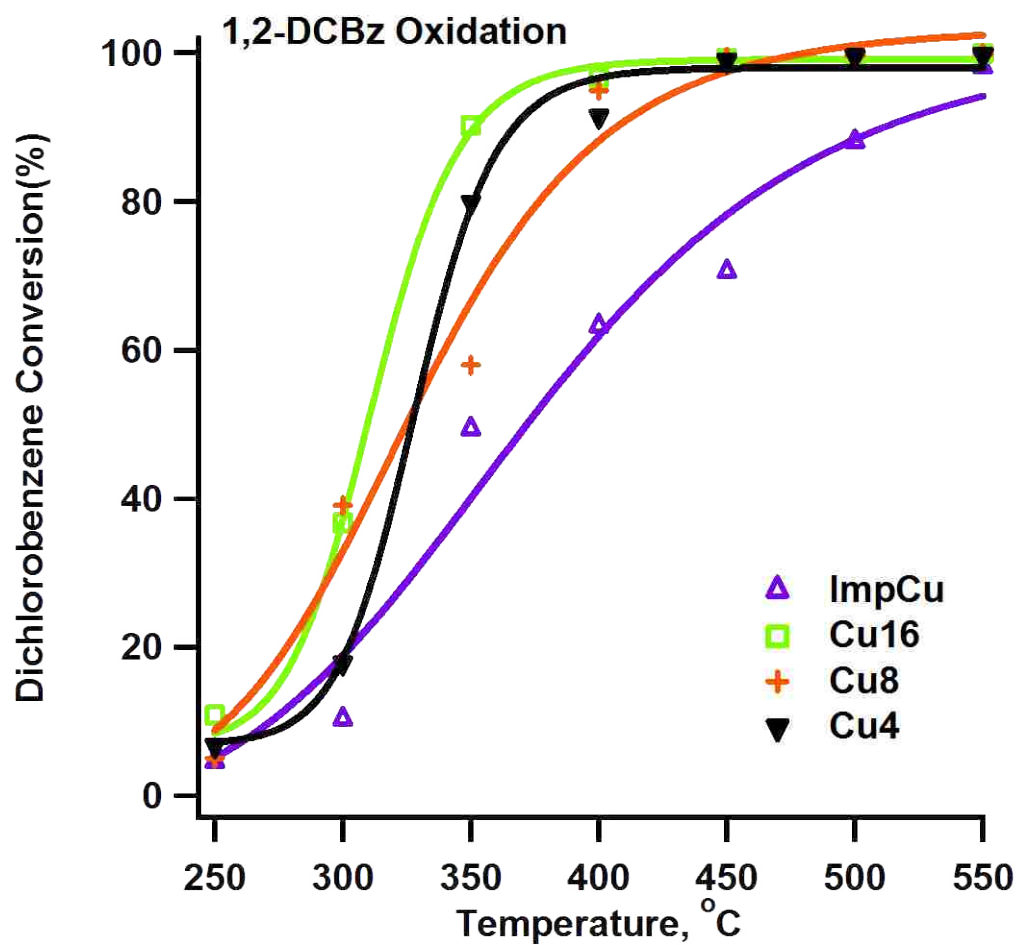
Figure 3.13 Conversion of 1,2-dichlorobenzene over
CuO/silica under pyrolytic condition

Table 3.4 Comparison of products yield (%) from the nano and coarse CuO surface-mediated pyrolysis of o-DCBz

Temperature (°C)		250	300	350	400	450	500	550	Size Effect***
Benzene	Coarse	-	0.003	0.008	0.027	0.033	**0.081****	0.062	
	Nano*	0.005	0.037	0.17	0.42	1.1	**1.6**	0.56	++
Chlorobenzene	Coarse	-	0.002	0.054	**0.20**	0.13	0.10	0.08	
	Nano	0.040	0.29	**0.57**	0.32	0.19	0.22	0.074	+
Phenol	Coarse	-	-	-	0.012	0.004	0.004	**0.016**	
	Nano	0.004	0.063	**0.22**	0.088	0.062	0.033	0.019	++
Benzofuran	Coarse	-	0.001	0.001	0.010	**0.024**	0.020	0.023	
	Nano	-	0.038	0.089	**0.10**	0.067	0.041	0.014	+
Trichlorobenzene	Coarse	-	0.033	**0.11**	0.068	0.073	0.031	0.013	
	Nano	0.010	0.026	**0.067**	0.028	0.019	0.014	0.002	-
Naphthalene	Coarse	-	-	0.001	**0.002**	0.001	0.001	0.001	
	Nano	-	0.003	0.009	**0.012**	0.001	0.001	-	+
Biphenyl	Coarse	-	-	**0.011**	0.007	-	-	-	
	Nano	0.001	0.024	**0.076**	0.036	0.026	0.014	0.011	+
Dibenzofuran	Coarse	-	-	**0.019**	0.014	0.008	0.009	0.007	
	Nano	0.025	0.041	0.072	0.075	**0.17**	0.11	0.076	++

* The data for nanoparticles are the results averaged from that of G4Cu4, G4Cu8 and G4Cu16

** Data in bold font is referred to the maximum yield obtained in the test temperature range

*** The signs of "+" and "++" indicate the products yields in Nano case is 2x~10x and >10x higher than those in Coarse case, respectively. In contrast, the signs of "-" and "--" indicate the products yields in Coarse case is 2x~10x and >10x higher than those in Nano case, respectively.

3.2.3 Copper Catalyzed Decomposition (Oxidation) of 1,2-Dichlorobenzene

The conversion of o-DCBz over the various copper oxide catalysts (5 wt.% metal loading) supported on powder formed silica (Cab-O-Sil) under oxidative condition is depicted in **Figure 3.14** as a function of the reaction temperature. The trend of conversion with respect to temperature showed a similar Sigmoid-shaped dependence as those in pyrolysis but achieved maximum conversion quicker. At 350 ºC, more than 75% o-DCBz was converted from the average results over the three $G4Cu_x$ catalysts and 49% for the IMPCu sample. More than 99% of DCBz was converted at 450 ºC in the case of $G4Cu(II)_n$, in comparison to only 70% and 98% conversion at 450 ºC and 550 ºC, respectively, for IMPCu catalyst. .

Oxidation of o-DCBz resulted in less product formation than in pyrolysis. **Table 3.5** summarized the average yield of products from nanosize catalysts, with the comparison to that of IMPCu. Detailed information of product yields over each catalyst can be found in **Appendix 2-B.**

The formation of trichloroethylene (TriCE) and tetrachloroethylene (TeCE) over $G4Cu_n$ achieved their maximum yield (average) of 0.11% and 1.2% at 400 ºC, respectively. In the case of IMPCu catalyst, the maximums were 0.022% at 450 ºC for TriCE and 0.15% at 400 ºC for TeCE. Other observed products were higher chlorinated benzenes only. The formation of trichlorobenzene (1,2,3+1,2,4-TriCBz), tetrachlorobenzene (1,2,3,4+1,2,3,5-TeCBzs), pentachlorobenzene and hexachlorobenzene were detected in maximum yields over $G4Cu_n$ as 2.9% at 350 ºC, 0.38% at 450 ºC, 0.13% at 400 ºC, and 0.21% at 350 ºC, compared with the results over IMPCu as 9.9% at 350 ºC, 2.8% at 450 ºC, 1.3% at 450 ºC, and 1.2% at 450 ºC.
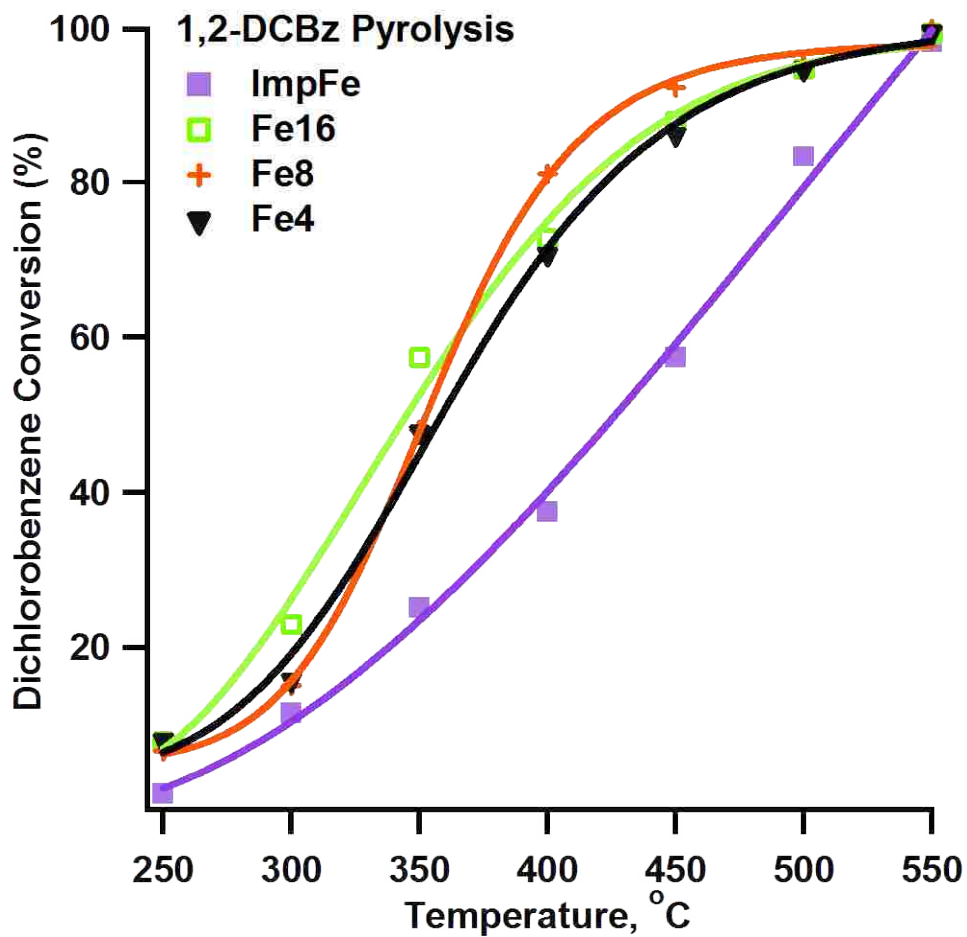
78

Figure 3.14 Conversion of 1,2-dichlorobenzene over
CuO/silica under oxidative condition

Table 3.5 Comparison of products yield (%) from the nanosize and coarse CuO surface-mediated oxidation of o-DCBz

Temperature (°C)		250	300	350	400	450	500	550	Size Effect***
Trichloroethylene	Coarse	-	-	0.001	0.015	**0.022**	0.009	0.002	
	Nano*	0.003	0.017	0.10	**0.11**	0.019	0.004	0.001	+
Tetrachloroethylene	Coarse	-	0.007	0.071	0.094	0.15	**0.32**	0.19	
	Nano	0.010	0.064	0.46	**1.1**	0.24	0.068	0.024	+
Trichlorobenzene	Coarse	0.22	5.3	**9.9**	8.2	8.8	2.6	0.22	
	Nano	0.37	1.4	**2.9**	2.2	0.72	0.21	0.057	-
Tetrachlorobenzene	Coarse	0.092	0.31	0.42	0.57	**2.8**	1.6	0.30	
	Nano	0.027	0.19	0.29	**0.38**	0.22	0.11	0.090	-
Pentachlorobenzene	Coarse	0.009	0.052	0.087	0.27	**1.3**	0.75	0.19	
	Nano	0.006	0.053	0.065	0.16	**0.32**	0.057	0.009	-
Hexachlorobenzene	Coarse	0.034	0.028	0.30	0.73	**1.2**	0.044	0.003	
	Nano	0.001	0.019	0.038	**0.082**	0.076	0.033	0.005	--

* The data for nanoparticles are the results averaged from that of G4Cu4, G4Cu8 and G4Cu16
** Data in bold font is referred to the maximum yield obtained in the test temperature range
*** The sign of "+"indicates the products yields in Nano case is 2x~10x higher than those in Coarse case. In contrast, the sign of
"-"indicates the products yields in Coarse case is 2x~10x higher than those in Nano case.

3.2.4 Iron Catalyzed Decomposition (Pyrolysis) of 1,2-Dichlorobenzene

The conversion of o-DCBz under pyrolytic conditions over various iron oxide nanoclusters $G4Fe_n$ and coarse particles of IMPFe supported on silica (Cab-O-Sil) are depicted in **Figure 3.15** as a function of the reaction temperature. At 350 ℃, more than 45% o-DCBz was converted over the $G4Fe_n$ catalysts while only 25% was converted over the IMPFe samples. At 450 ℃, the average conversion of o-DCBz over the $G4Fe_n$ was 89% (88% for G4Fe16, 92% for G4Fe8 and 86% for G4Fe4) while only 57% for the impregnated samples. At 550 ℃ almost 100% conversion of o-DCBz was achieved for each catalyst sample.

Various products were detected from the pyrolytic decomposition of o-DCBz over iron oxide catalysts. **Table 3.6** summarizes the average yield of products from nanosize catalysts, in comparison to that of the IMPFe case. Detailed information of product yield over each catalyst can be found in **Appendix 2-C.** The formation of Bz and MCBz achieved their maximum yields (average) as 4.9% at 500℃ 11.9% at 450 ℃ respectively, over the $G4Fe_n$ catalyst. In the coarse catalyst case, the maximum yields are 0.034% at 550 ℃ for Bz and 4.2% at 500 ℃ for MCBz. The yield of BF reached maxima at 0.21% at 450-500 ℃ for $G4Fe_n$ and 0.060% at 500 ℃ for IMPFe, respectively. Phenol was formed with a maximum yield of 0.56% at 500 ℃ over the catalysts of $G4Fe_n$ and 0.024% at 550 ℃ in the case of IMPFe. In addition to the formation of phenol, monochlorophenol (MCP) and dichlorophenol (DCP) were observed with a combined maximum yield of 0.28% at 450-500 ℃ from $G4Fe_n$, compared to 0.097% at 550 ℃ from IMPCu catalyst. Formation of trichlorobenzene (1,2,3+1,2,4-TriCBz) reached its maximum yield of 1.85 at 450 ℃ in the cases of $G4Cu_n$ and 5.6% at 500 ℃ for IMPFe. Formation of biphenyl (BP) was observed with a maximum yield of 0.034% at 500 ℃ over $G4Fe_n$, while undetected from the reaction using IMPFe. Dibenzofuran (DF) was the only consistently observed

PCDD/Fs product in this series of experiments. It was maximally formed 0.18% at 500 ℃ for

G4Fe$_n$ and only 0.030% at 500 ℃ for IMPFe.

Figure 3.15 Conversion of 1,2-dichlorobenzene over
Fe$_2$O$_3$/silica under pyrolytic condition

Table 3.6 Comparison of products yield (%) from the nano-size and coarse Fe_2O_3 surface-mediated pyrolysis of o-DCBz

Temperature (°C)		250	300	350	400	450	500	550	Size Effect***
Benzene	Coarse	-	0.004	0.044	0.004	0.025	0.31	**0.34**	
	Nano*	0.002	0.010	0.04	0.050	0.70	**4.9**	3.1	++
Chlorobenzene	Coarse	-	-	0.016	0.018	0.10	**4.2**	3.1	
	Nano	0.001	0.007	0.034	0.31	**11**	8.9	4.8	+
Phenol	Coarse	-	-	-	-	-	0.010	**0.024**	
	Nano	-	-	0.018	0.031	**0.34**	0.57	0.013	++
Benzofuran	Coarse	-	-	-	-	-	**0.060**	0.024	
	Nano	-	-	0.001	0.06	**0.22**	0.21	0.015	+
Trichlorobenzene	Coarse	-	0.32	0.39	1.1	3.8	**5.9**	0.47	
	Nano	-	0.28	1.3	1.6	**1.8**	0.63	0.18	-
Tetrachlorobenzene	Coarse	-	-	0.005	**0.14**	0.071	0.011	-	
	Nano	-	-	0.014	0.019	0.088	**0.18**	0.039	
Chlorophenol	Coarse	-	-	-	-	-	0.067	**0.097**	
	Nano	-	0.002	0.011	0.11	0.28	**0.29**	0.055	+
Biphenyl	Coarse	-	-	-	-	-	-	-	
	Nano	-	-	-	0.003	0.014	**0.035**	0.002	++
Dibenzofuran	Coarse	-	-	-	-	-	**0.030**	0.010	
	Nano	-	-	0.001	0.022	0.17	**0.19**	0.066	+

* The data for nanoparticles are the results averaged from that of G4Cu4, G4Cu8 and G4Cu16
** Data in bold font is referred to the maximum yield obtained in the test temperature range
*** The signs of "+" and "++" indicate the products yields in Nano case is 2x~10x and >10x higher than those in Coarse case, respectively. In contrast, the signs of "-" and "--" indicate the products yields in Coarse case is 2x~10x and >10x higher than those in Nano case, respectively.

3.2.5 Iron Catalyzed Decomposition (Oxidation) of 1,2-Dichlorobenzene

The conversion of o-DCBz over the various iron oxide catalysts (5 wt% metal loading) supported on powder formed silica (Cab-O-Sil) under oxidative condition is shown in **Figure 3.16** as a function of the reaction temperature. The trends of conversion with respect to temperature showed a similar Sigmoid-shaped dependence as those in pyrolysis but achieved maximum conversion quicker. At 350 ºC, more than 75% o-DCBz was converted from the average results over the three $G4Fe_x$ and only 19% for the impregnated samples. More than 95% of o-DCBz was converted at 450 ºC in the case of $G4Fe_n$, in comparison to only 75% and 98% conversion at 450 ºC and 550 ºC, respectively, for IMPFe catalyst.

Similar to the decomposition of o-DCBz over copper oxide catalysts, fewer products were formed than from pyrolytic conditions. **Table 3.7** summarizes the average yield of products from all three nanosize catalysts, with the comparison to that of IMPFe case. Detailed information of products yield over each catalyst can be found in **Appendix 2-D.**

The formation of trichloroethylene (TriCE) and tetrachloroethylene (TeCE) achieved their maximum yields of 0.31% and 0.72% at 400 ºC for $G4Fe_n$. In the impregnated catalyst case, the maximum yields were 0.057% at 500 ºC for TriCE and 0.11% at 450 ºC for TeCE. Other observed major products are higher chlorinated benzenes. The formation of trichlorobenzene (1,2,3+1,2,4-TriCBz), tetrachlorobenzene (1,2,3,4+1,2,3,5-TeCBzs), pentachlorobenzene and hexachlorobenzene were detected in maximum yields over $G4Fe_n$ as 1.1% at 400 ºC, 0.40% at 400 ºC, 0.057% at 400 ºC, and 0.10% at 400 ºC, compared with the results over IMPFe as 1.5% at 450 ºC, 0.15% at 450 ºC, 0.066% at 400 ºC, and 0.022% at 400 ºC.
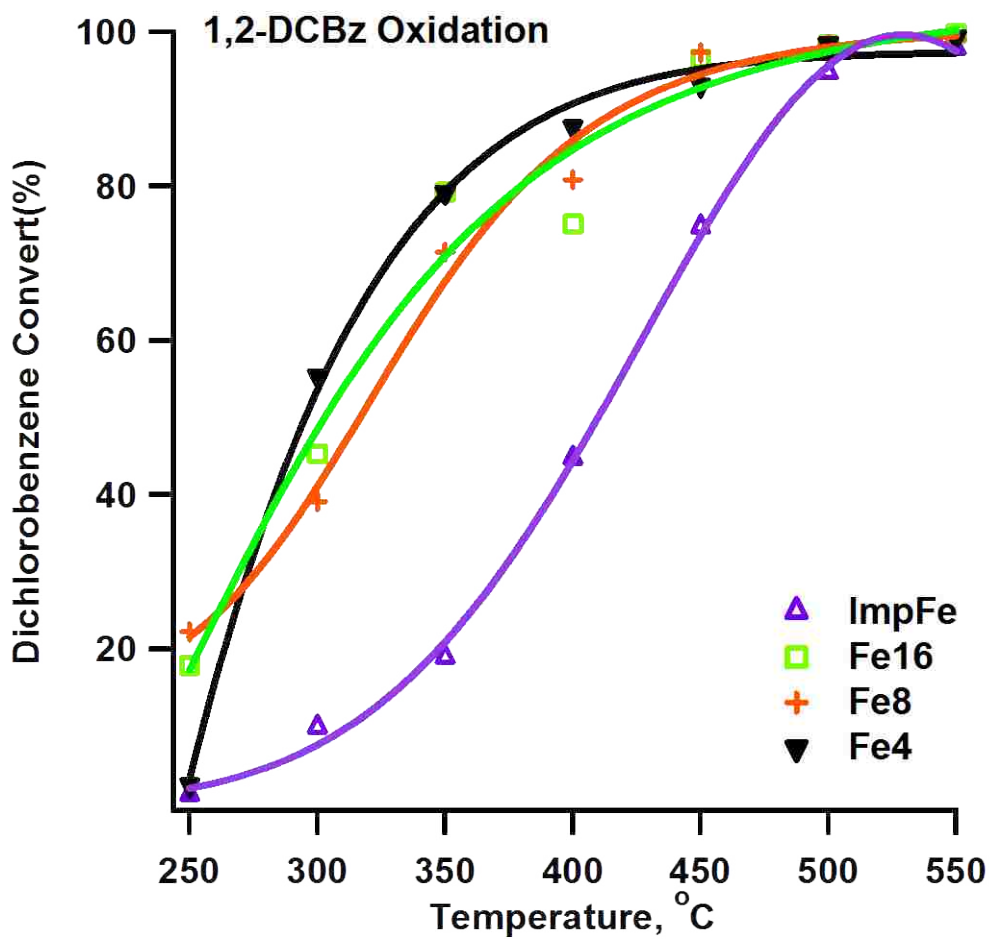
Figure 3.16 Conversion of 1,2-dichlorobenzene over
Fe$_2$O$_3$/silica under oxidative condition

.

Table 3.7 Comparison of products yield (%) from the nanosize and coarse Fe_2O_3 surface-mediated oxidation of o-DCBz

Temperature (°C)		250	300	350	400	450	500	550	Significant Change***
Trichloroethylene	Coarse	-	-	0.013	0.023	0.027	**0.057****	-	
	Nano*	0.011	0.049	0.12	**0.31**	0.093	0.045	-	+
Tetrachloroethylene	Coarse	-	-	0.035	0.018	0.11	0.038	-	
	Nano	0.001	0.013	0.12	**0.72**	0.15	0.15	-	++
Trichlorobenzene	Coarse	0.085	-	0.40	1.1	**1.5**	1.0	-	
	Nano	0.36	0.56	0.52	**1.1**	0.68	0.34	-	-
Tetrachlorobenzene	Coarse	-	-	-	0.066	**0.15**	0.007	-	
	Nano	0.027	0.079	0.11	**0.40**	0.13	0.045	-	+
Pentachlorobenzene	Coarse	-	-	0.004	**0.066**	-	0.014	-	
	Nano	0.010	0.019	0.029	**0.057**	0.007	0.007	-	
Hexachlorobenzene	Coarse	-	-	-	**0.022**	0.005	-	-	
	Nano	-	-	0.053	**0.010**	0.025	0.01	-	-

* The data for nanoparticles are the results averaged from that of G4Cu4, G4Cu8 and G4Cu16
** Data in bold font is referred to the maximum yield obtained in the test temperature range
*** The signs of "+" and "++" indicate the products yields in Nano case is 2x~10x and >10x higher than those in Coarse case, respectively. In contrast, the signs of "-" and "--" indicate the products yields in Coarse case is 2x~10x and >10x higher than those in Nano case, respectively.

3.2.6 Iron Catalyzed Decomposition (Pyrolysis) of Chlorobenzene

The conversion of MCBz under pyrolytic conditions over $G4Fe_n$ and IMPFe catalysts are depicted in **Figure 3.17** as a function of the reaction temperature.   Compared to o-DCBz, MCBz is harder to decompose as indicated by the trend of its conversion.   At 400 ºC there was only ~30% (average) MCBz converted over $G4Fe_n$ catalysts and only 11% for IMPFe. However, about 90% of MCBz was converted over $G4Fe_n$ when temperature increased to 450 °C, and 42% conversion for IMPFe. At 550 ºC the conversion of MCBz was >99% for all $G4Fe_n$ catalysts and 91% for IMPFe.

Various products were detected from the pyrolytic decomposition of MCBz over iron oxide catalysts. **Table 3.8** summarized the average yield of products from all three nanosized catalysts, with the comparison to that of IMPFe. Detailed information of product yield over each catalyst can be found in **Appendix 2-E.**

Significant yields of Bz were observed over both $G4Fe_n$ and IMPFe catalysts.   The maximum yields of Bz was 44% at 500 °C for $G4Fe_n$ and 15% at 550 °C for IMPFe. The yield of BF reached a maximum of 0.31% at 500 ºC for $G4Fe_n$ and 0.15% at 500 ºC for IMPFe. Maximum Phenol yield was 0.27% at 500 ºC over $G4Fe_n$ catalyst and 0.19% at 550 ºC over IMPFe. Non-chlorinated phenols were detected. Dichlorobenzene was formed with a maximum yield of 0.39% at 400ºC for IMPFe and less than 0.1% at all temperatures for $G4Fe_n$. Biphenyl (BP) was observed with a maximum yield of 0.02% at 500 ºC over $G4Fe_n$, and 0.24% at 550 ºC from the reaction over IMPFe. The only observed PCDD/Fs product, Dibenzofuran (DF), was maximally formed at 0.62% at 500 ºC in $G4Fe_n$ case and 0.77% at 550 ºC in IMPFe case.
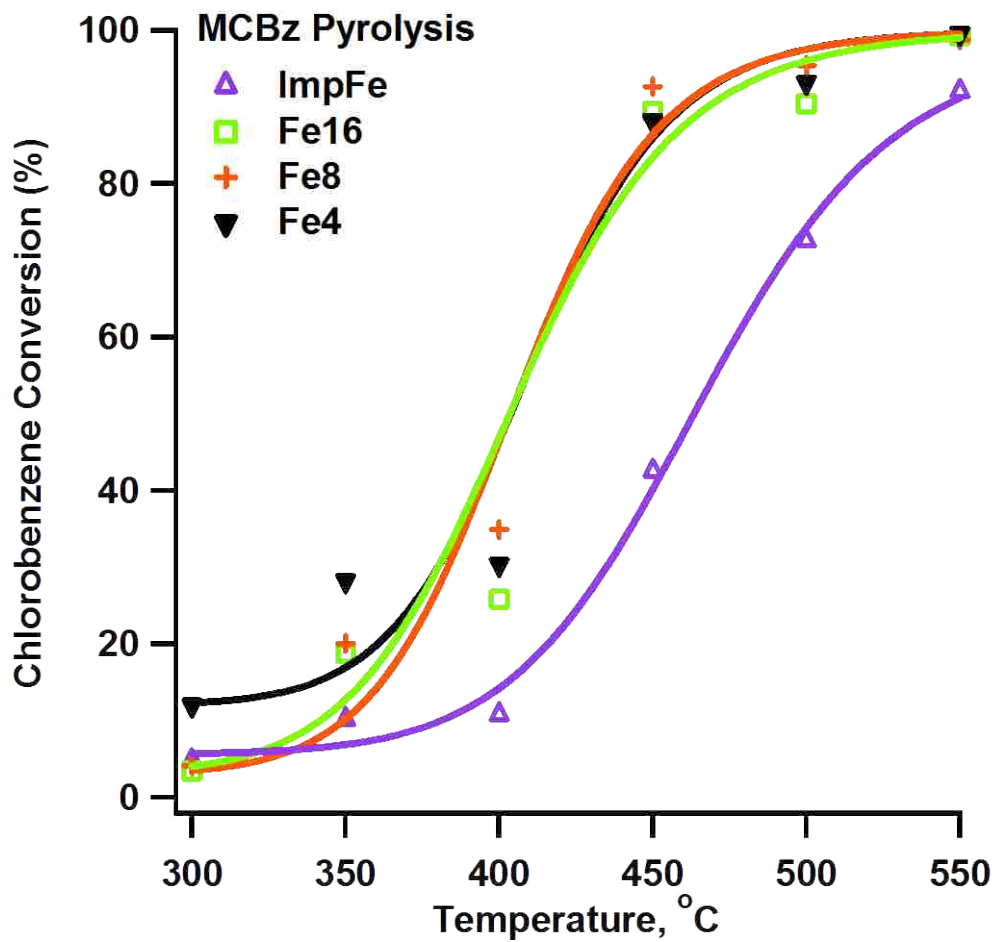
Figure 3.17 Conversion of monochlorobenzene over Fe$_2$O$_3$/silica under pyrolytic condition

Table 3.8 Comparison of products yield (%) from the nanosize and coarse Fe_2O_3 surface-mediated pyrolysis of MCBz

Temperature (°C)	300	350	400	450	500	550	SizeEffect*
Benzene	0.005	0.13	0.75	3.7	6.6	**15**	
	0.036	1.1	4.6	22	**44**	30	+
Toluene	-	-	-	-	-	**0.010**	
	-	0.001	0.005	0.012	**0.022**	0.005	+
Phenol	-	-	-	0.27	0.13	**0.19**	
	-	-	0.004	0.066	**0.27**	-	
Benzofuran	-	-	-	0.053	0.069	**0.15**	
	-	0.004	0.045	0.19	**0.31**	0.14	+
Dichlorobenzene	0.067	0.081	**0.39**	0.27	0.10	0.18	
	0.029	0.066	**0.075**	0.027	0.044	0.005	-
Naphthalene	-	-	-	-	-	**0.026**	
	-	-	-	0.010	**0.022**	0.012	
Biphenyl	-	-	-	-	0.038	**0.24**	
	-	0.003	0.004	0.022	**0.12**	0.080	-
DiPhenyl-Ether	-	-	-	-	0.023	**0.041**	
	-	-	0.003	0.025	**0.042**	0.012	
Dibenzofuran	-	-	-	0.014	0.14	**0.77**	
	-	0.016	0.011	0.14	**0.62**	0.32	

* The data for nanoparticles are the results averaged from that of G4Cu4, G4Cu8 and G4Cu16
** Data in bold font is referred to the maximum yield obtained in the test temperature range
*** The signs of "+"indicates the products yields in Nano case is 2x~10x higher than those in Coarse case. In contrast, the signs of "-"indicates the products yields in Coarse case is 2x~10x higher than those in Nano case.

3.2.7   Iron Catalyzed Thermal Degradation (Oxidation) of Chlorobenzene

The conversion of MCBz under oxidative conditions over G4Fe$_n$ and IMPFe catalysts is shown in **Figure 3.18** as a function of the reaction temperature. The trends of conversion with respect to temperature showed a similar Sigmoid-shaped dependence as those in pyrolysis but achieved the same conversion ratio at lower temperature. At 400ºC ~70% MCBz was converted from the average results over the three G4Fe$_n$ and only 37% for the impregnated samples. About 90% of MCBz was converted at 450 ºC in reaction with G4Fe$_n$, in comparison with only 64% conversion at 450 ºC in the reaction over IMPFe.

Very few products were observed from the oxidative reaction of MCBz over iron oxide catalysts. **Table 3.9** summarizes the average yield of products from all three nanosized catalysts, with the comparison to that of the IMPFe case. Detailed information of product yield over each catalyst can be found in **Appendix 2-F.**

The formation of trichloroethylene (TriCE) achieved a maximum yield of 0.1% at 400 ºC over G4Fe$_n$. No TriCe was detected in reaction over IMPFe. DCBz was detected maximally in a wide temperature range for both G4Fe$_n$ and IMPFe. Specifically, there was 0.74 to 1.0% yield of DCBz for G4Fe$_n$ at temperatures of 350-450 ºC, and 0.51 to 0.61% for IMPFe at temperatures of 350-500 ºC.

3.3   Flow Reactor Studies of Soot Formation Mediated by Metal Oxide Nanoparticles

3.3.1   Generation of Gas-Suspended Metal Oxide Nanoparticles

Using a thermoelectric flow reactor (particle generator), methanolic solutions of dendrimer-metal complexes were used to produce gas-suspended metal oxide nanoparticles at temperatures from 500 to 900 °C under oxidative conditions. Initial efforts to explore the optimized conditions for the formation of metal oxide nanoparticles were performed by using
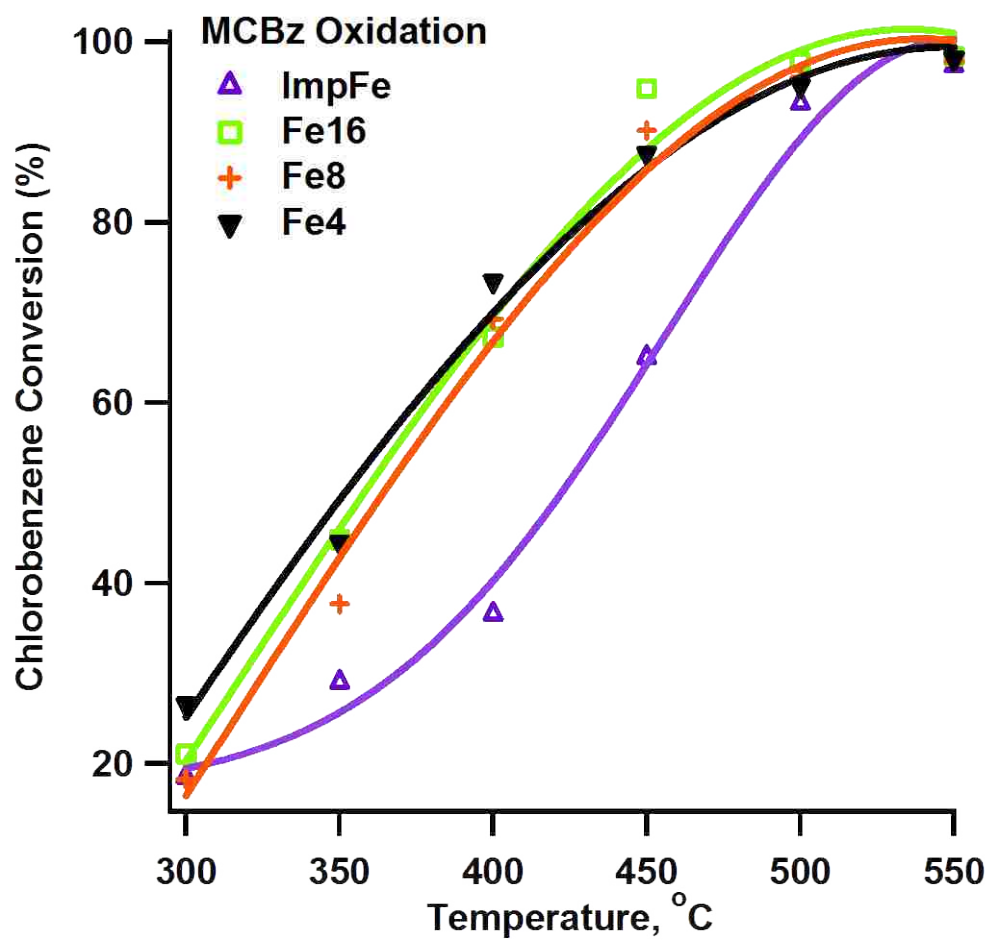
Figure 3.18 Conversion of monochlorobenzene over Fe$_2$O$_3$/silica under oxidative condition

Table 3.9 Comparison of products yield (%) from the nanosize and coarse Fe_2O_3 surface-mediated oxidation of MCBz

Temperature (°C)		300	350	400	450	500	550	Size Effect***
Trichloroethylene	Coarse	ND.	ND.	ND.	ND.	ND.	ND.	
	Nano*	0.003	0.036	0.10	0.034	0.007	ND.	++
Dichlorobenzene	Coarse	0.12	0.51	0.60	0.55	0.59	0.10	
	Nano	0.35	0.74	1.0	0.86	0.49	0.19	

* The data for nanoparticles are the results averaged from that of G4Cu4, G4Cu8 and G4Cu16
** Data in bold font is referred to the maximum yield obtained in the test temperature range
*** The signs of "+" and "++" indicate the products yields in Nano case is 2x~10x and >10x higher than those in Coarse case, respectively. In contrast, the signs of "-" and "--" indicate the products yields in Coarse case is 2x~10x and >10x higher than those in Nano case, respectively.

G4Cu(II)$_{16}$ methanolic solution (2mM equivalent concentration of Cu) as a precursor. Though the formation of copper oxide nanoparticles was observed in all tested temperatures using TEM and EDS, carbonaceous materials due to the incomplete combustion were also observed for the relative low temperatures cases (500 and 600 °C). **Figure 3.19** shows the TEM micrograph of samples collected in the 500 °C experiment. Carbonaceous materials were observed with sizes from several nanometers to several hundred nanometers (in the form of agglomeration). The inset image taken at the central part of the figure indicated the presence of higher density nanoparticles (ave. 2.03±0.35 nm) on or in the carbonaceous materials. Results of EDS spectra indicated these darker nanoparticles were copper oxide.
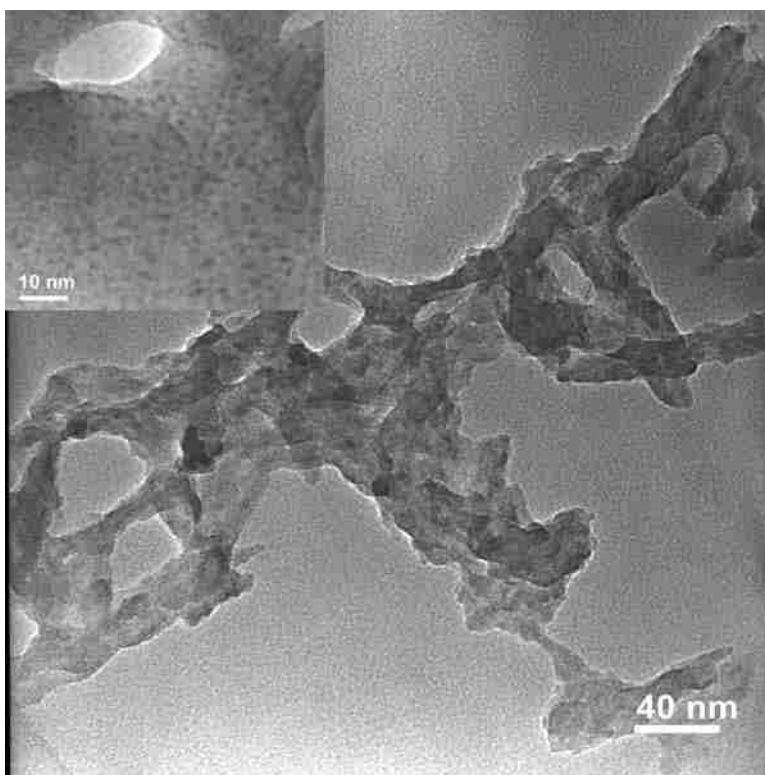
Figure 3.19 HRTEM micrograph of the particulate matter produced by the combustion of G4Cu(II)$_{16}$/methanol precursor at 500 °C. The agglomerated carbonaceous particles were the products of incomplete combustion due to low reactor temperature. Copper oxide nanoparticles with size 1-2nm were embedded in the carbonaceous residuals, as shown in the inset

Compared to the 500 °C case, less carbonaceous material was observed on the TEM grid sample used in the 600 °C experiments. Meanwhile, most copper oxide nanoparticles were found in areas free of such carbonaceous particulate matters. **Figure 3.20a** presents the TEM micrograph of these copper oxide nanoparticles and their size distribution, with an average of 2.35±0.44 nm. Experiments performed at a temperature of 700 °C also produced carbon-free copper oxide nanoparticles with rather uniform size of 2.85±0.40 nm (c.f. **Figure 3.20b**). However, no carbonaceous particulate matter was observed using TEM imaging. When the temperature was increased to 900 °C, larger crystalline copper oxide particles with sizes of 40 to 80 nm were observed due to the thermal aggregation (c.f.**Figure 3.21**).
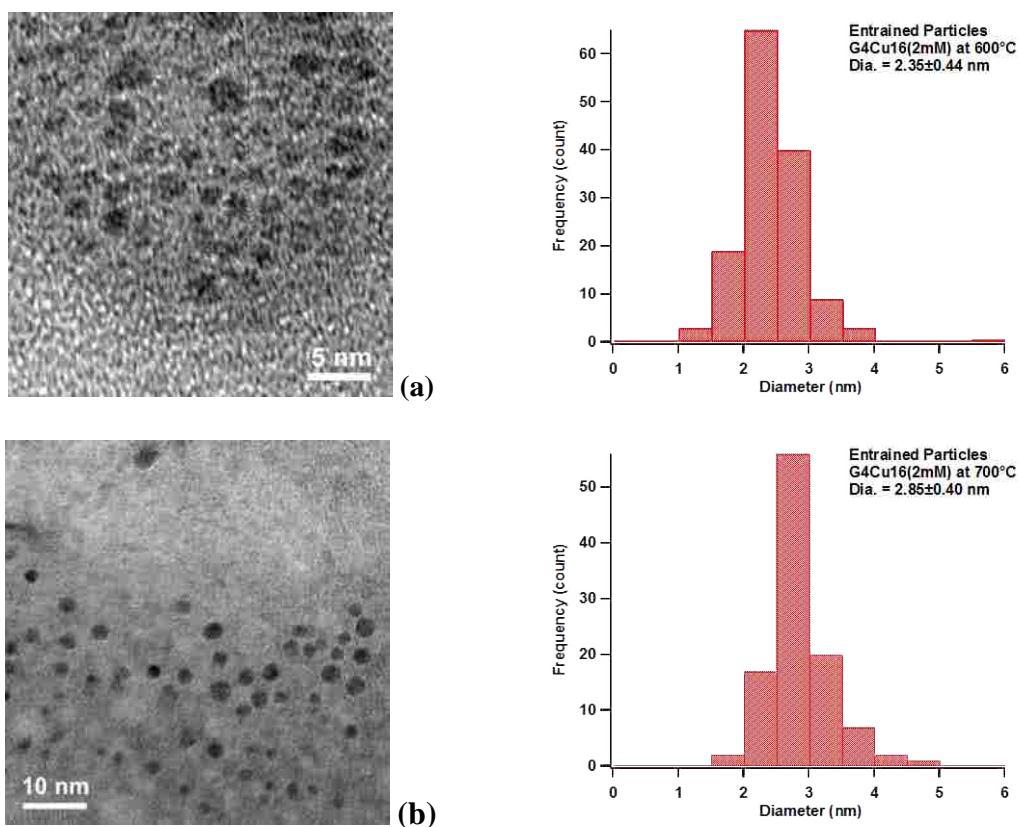
Figure 3.20 HRTEM micrographs of the particulate matter produced by the combustion of G4Cu(II)$_{16}$/methanol precursor at 600 **(a)** and 700 °C **(b)**. Uniformed size copper (oxide) nanoparticles were observed. However, there is still some carbonaceous residuals found for sample collected at 600°C, but not the case for 700 °C.
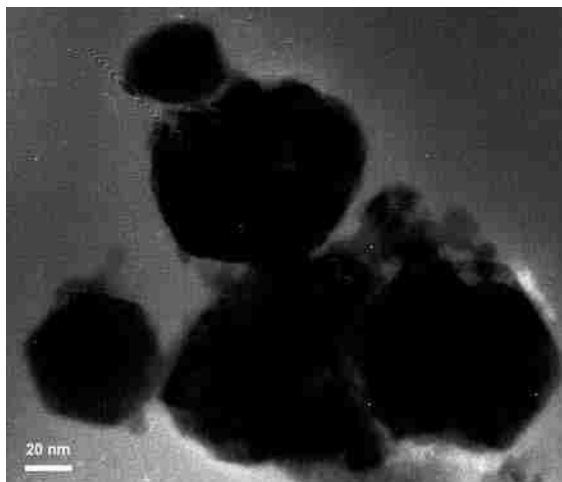
Figure 3.21 HRTEM micrograph of the particulate matter produced by the combustion of G4Cu(II)$_{16}$/methanol precursor at 900 °C. Large crystalline copper (oxide) nanoparticles (40-80 nm) were observed

The generation of iron oxide nanoparticles was obtained using G4Fe(III)$_{16}$ methanolic solution (2mM equivalent concentration of Fe) as a precursor. With the same experimental setting as those for copper, carbon-free iron oxide nanoparticles were observed at temperatures of 600 and 700 °C, though there was still some carbonaceous residue in the former. **Figure 3.22** presents the TEM micrograph of sample collected in the 700 °C experiments which show the formation of iron oxide nanoparticles with a size of 3.19±0.41 nm.
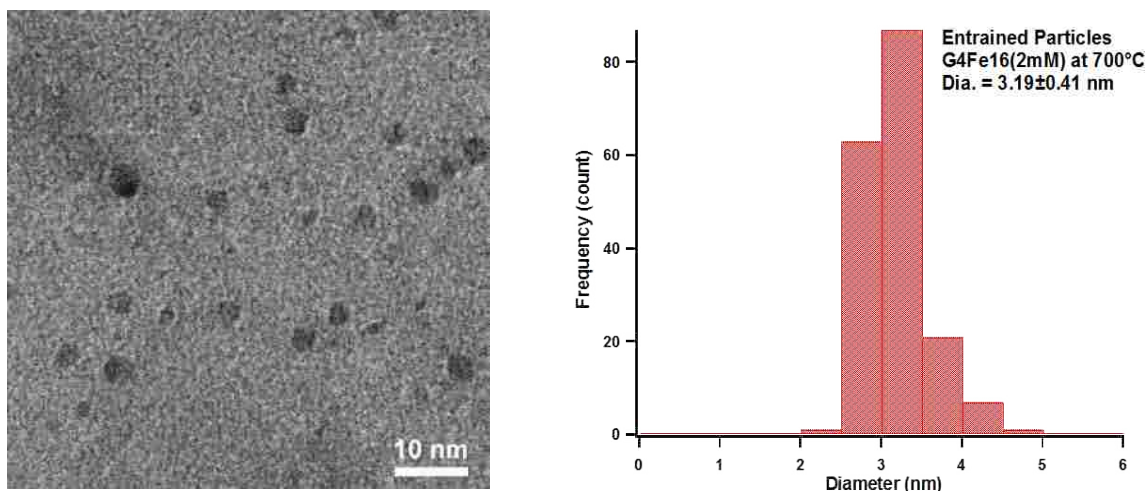
Figure 3.22 HRTEM picture of the particulate matter produced by the combustion of G4Fe(II)$_{16}$/methanol precursor at 700 °C

95

3.3.2 Morphology Studies of Soot Formation

Soot-like particulate matter could be produced in this custom designed flow reactor with the appropriate setting of temperature and fuel-to-air equivalent ratio C/O. **Figure 3.23a** is a bright field TEM micrograph of soot particles collected at the flow reactor outlet when burning methylnaphthalene at 1100 °C (C/O = 5) with the presence of iron oxide nanoparticles. These soot particles were composed of carbonaceous materials and in spherical shape with an average diameter of 33.7 nm. **Figure 3.23b** is a high resolution lattice image of a methylnaphthalene soot particle. The graphic ordered domains indicated by the layered structures can be observed in regions (I) and (II). The lattice fringes from (I) and (II) corresponded to the interlayer spacing (d_{002}) between the graphitic layers and typically measured at 0.43nm, in contrast to the d_{002} spacing of standard graphite which being reported as 0.34 nm.[3]

The addition of iron oxide nanoparticles to the pyrolytic combustion of 1-methylnaphthalene did not result in a noticeable difference on the morphology of soot particles. **Figure 3.24** HRTEM image of soot produced by burning methylnaphthaleneshows the HRTEM micrographs of a methylnaphthalene soot particle produced without the additions of metal oxide nanoparticles. However, the threshold of C/O for soot particle detection in experiments with addition of iron oxide nanoparticles did drop to a lower value in comparison to that for the non-metal experiments. **Figure 3.25** HRTEM image of soot produced by burning methylnaphthaleneshows HR-TEM images of a series of carbonaceous products collected from experiments using different C/O values (1.4, 1.6, 2.0, 2.5, 5.0). In the non-metal experiments, irregular shaped carbonaceous materials were dominant at a low C/O value (1.4-2.0) conditions. When C/O value was increased to 2.5, chain-like soot particles were observed as well as carbonaceous particulate matter. For C/O = 5.0, the only observed carbonaceous particulate matter was soot, which is in the form of larger agglomeration than those of C/O = 2.5. With the

(a)

(b)
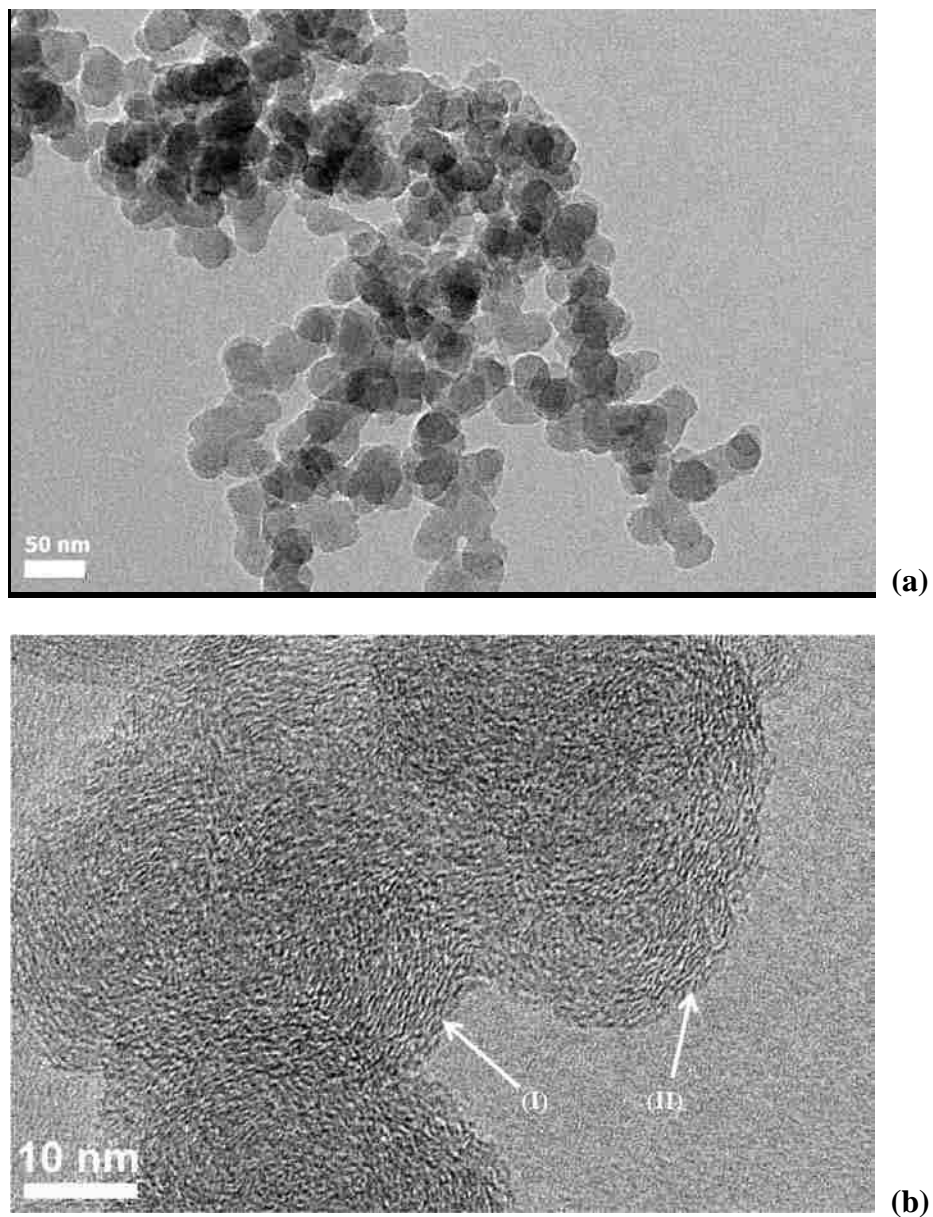
Figure 3.23 HRTEM image of soot produced by burning methylnaphthalene
at 1100 °C in the flow reactor with addition of iron oxide nanoparticles, C/O = 5

addition of iron oxide nanoparticles, the carbonaceous products due to the incomplete
combustion show more structural features than those formed in non-metal experiments. For C/O
= 1.4 and 1.6, though no onion-like soot particles were observed, the agglomeration of
carbonaceous materials were denser and particle-like than those formed in non-metal
experiments. Increasing C/O ratios to 2.0-5.0 resulted in the formation of soot particles. Similar

to the non-metal case, the observed population of soot particles and their size of agglomeration also increased with C/O values. In a side-by-side comparison between iron-oxide-addition and non-metal experiments (C/O = 5.0), the observed population of soot particles was much higher in the former case.
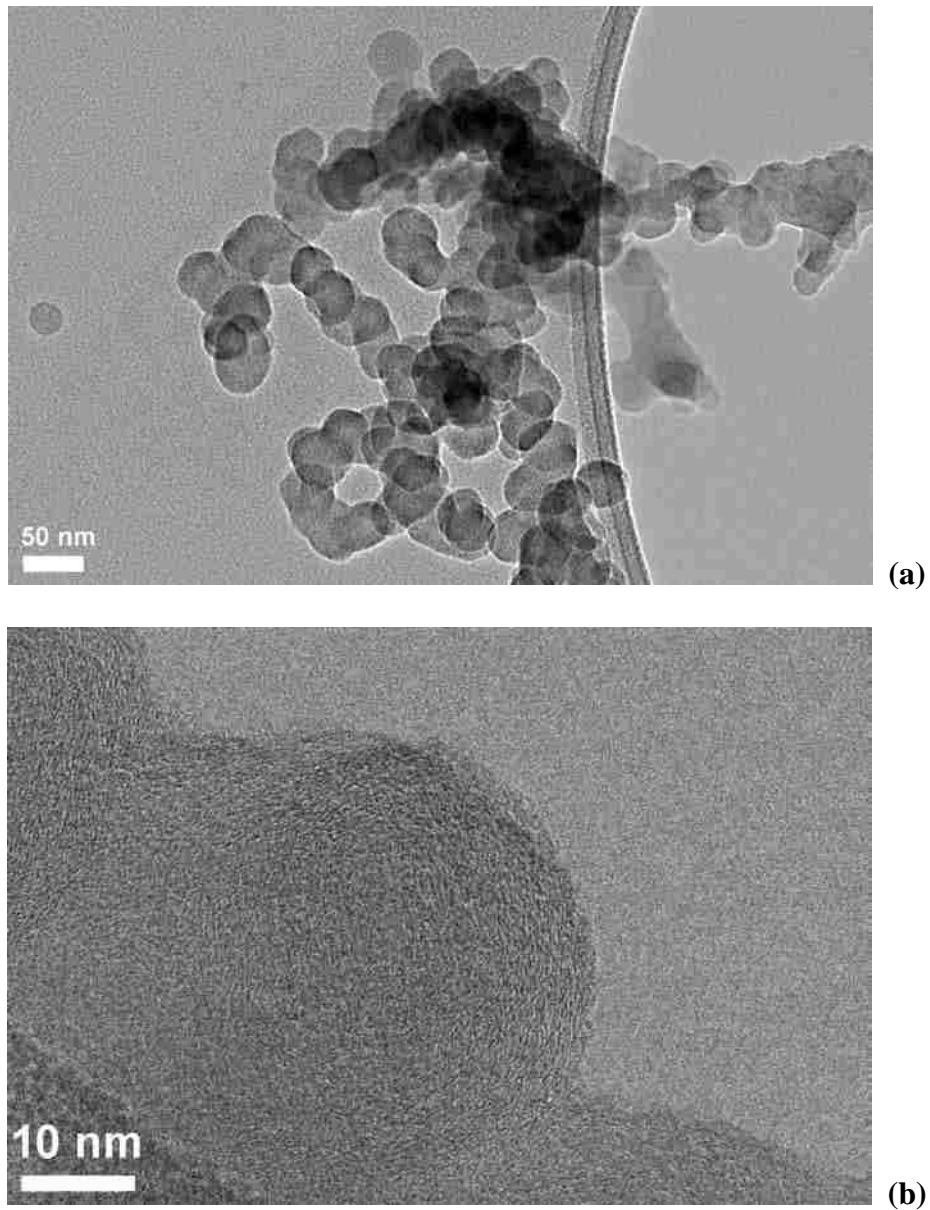
(a)

(b)

Figure 3.24 HRTEM image of soot produced by burning methylnaphthalene
at 1100 °C in the flow reactor, C/O = 5
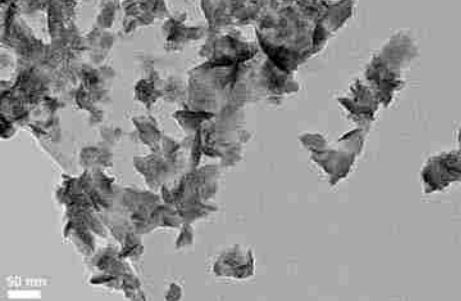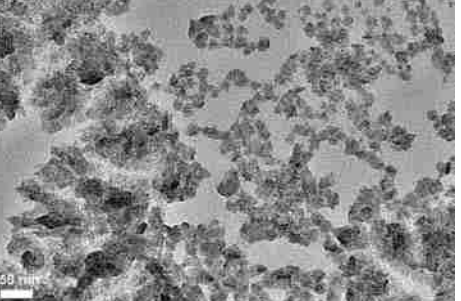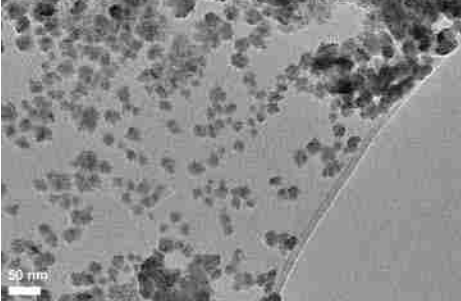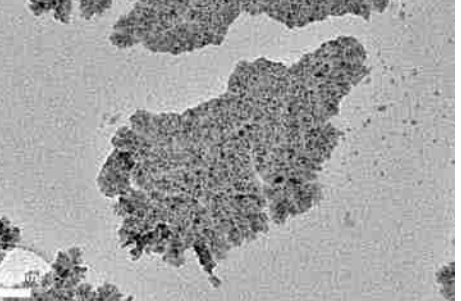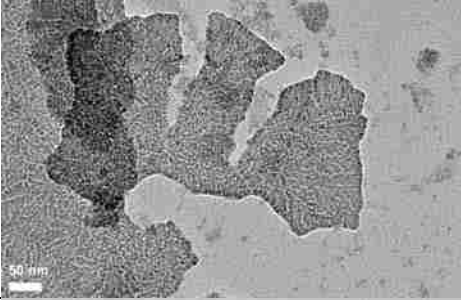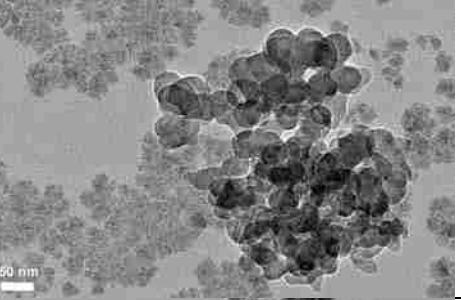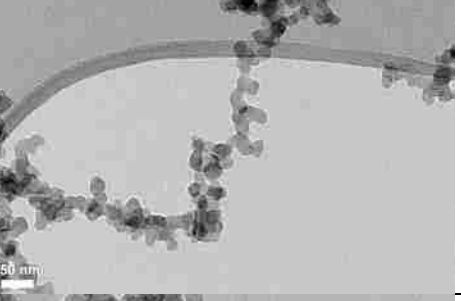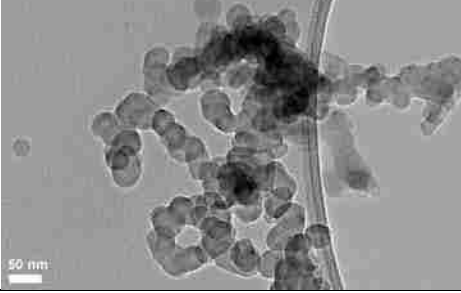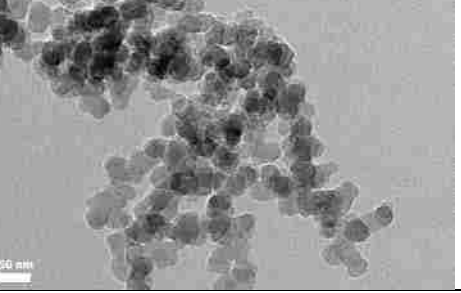
C/O	Methylnaphthalene Only	Methylnaphthalene + iron (oxide) nanoparticles
1.4		
1.6		
2.0		
2.5		
5.0		

Figure 3.25 HRTEM image of soot produced by burning methylnaphthalene
at 1100 °C in the flow reactor, C/O = 1.4, 1.6, 2, 2.5 and 5

3.3.3 PAH Analysis of Extractable Organic Material from Soot

Various organic solvents could be used for extraction of organic materials from soot. [4-6] In this experiment, chloroform was determined to be the most powerful solvent for soot extraction as more PAH species were found in its extractable material than those using other solvents (methanol, ethanol, dichloromethane, and hexane). **Figure 3.26** shows a typical GC/MS spectra of samples collected from the under-stoichiometric combustion (C/O = 2.5) of methylnaphthalene at 1000 °C with the presence of iron oxide nanoparticles. Though more than 30 PAH peaks were presented in all chromatogram spectra, we only monitored those species with carbon number >11 and appear consistently in spectra.
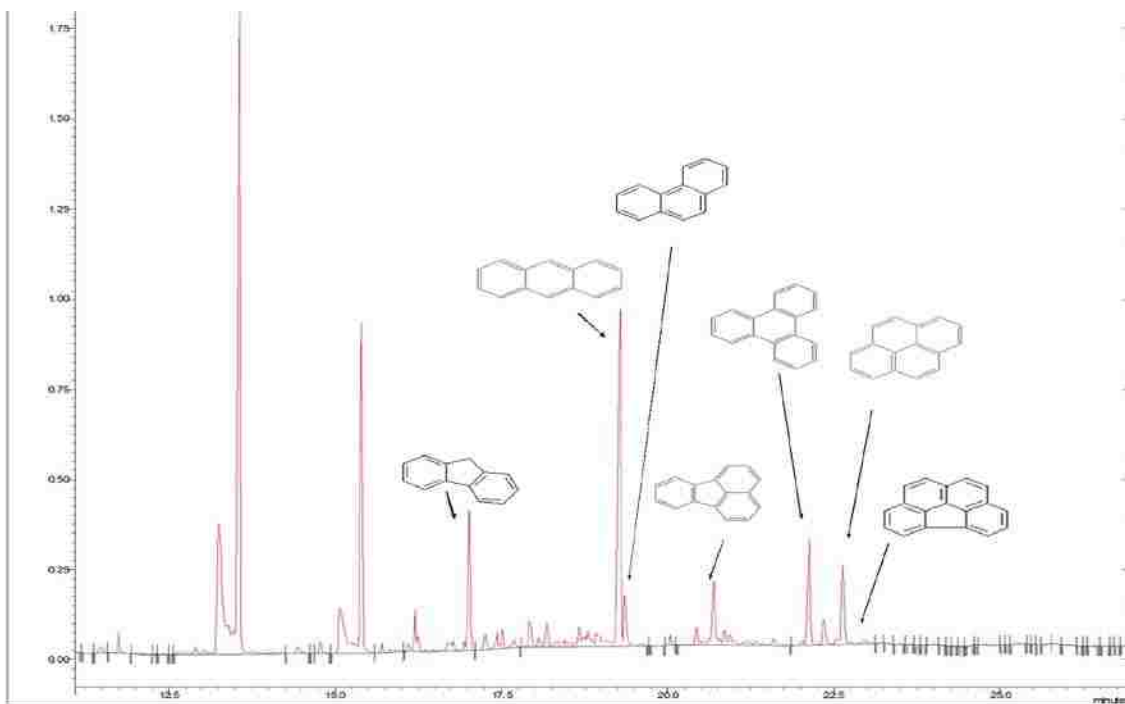
Figure 3.26 Gas chromatograph of extractable PAH from particulate matter obtained under-stoichiometric combustion (C/O = 2.5) of methylnaphthalene at 1000°C with the presence of iron (oxide) nanoparticles

Figure 3.27 presents the results of the extraction of condensable materials collected from combustion with and without metal addition, respectively. 8 PAH species (C12-C20) were

100

considered for relative total carbon calculation for evaluating the formation of soot. The relative

yield of each PAH was calculated based on the total carbon value.
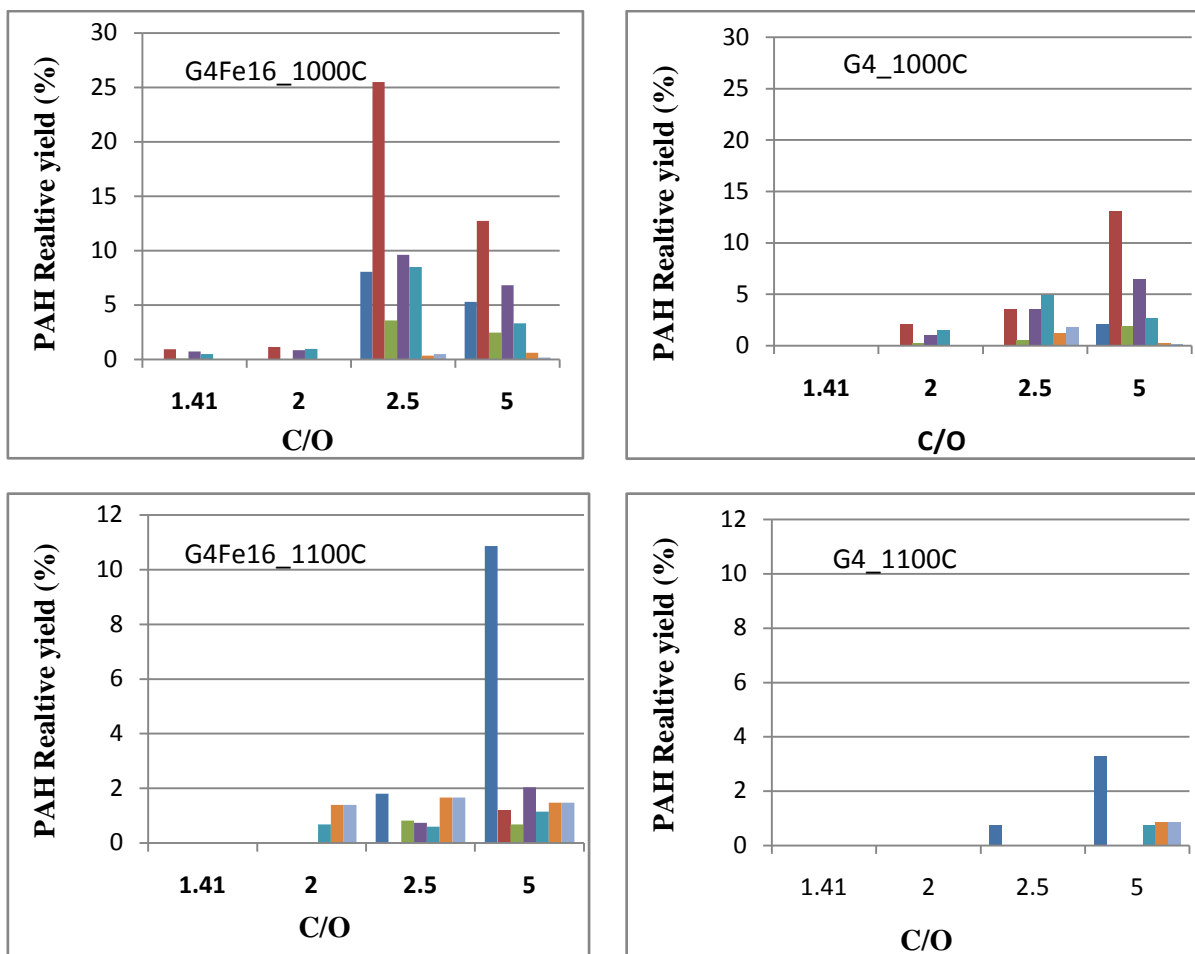
Figure 3.27 Relative concentration of
PAH products from extraction
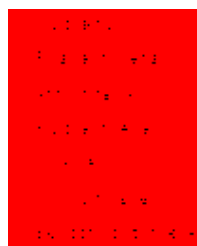
3.4   References

1.   Grosvenor, A. P.; Kobe, B. A.; McIntyre, N. S.; Tougaard, S.; Lennard, W. N., Use of
QUASIES (TM)/XPS measurements to determine the oxide composition and thickness on an
iron substrate. *Surf Interface Anal* **2004,** 36, (7), 632-639.

2.   Bosman, A. W.; Schenning, A. P. H. J.; Janssen, R. A. J.; Meijer, E. W., Well-defined
metallodendrimers by site-specific complexation. *Chem Ber-Recl* **1997,** 130, (6), 725-728.

3.   Falke, U.; Weber, A. K.; Ullmann, J., Dispersion of the Valence Electron-Energy-Loss in Thin Amorphous-Carbon Films Deposited by Ion-Assisted Evaporation of Graphite. *Microsc Microanal M* **1995,** 6, (1), 113-120.

4.   Santamaria, A.; Mondragon, F.; Quinonez, W.; Eddings, E. G.; Sarofim, A. F., Average structural analysis of the extractable material of young soot gathered in an ethylene inverse diffusion flame. *Fuel* **2007,** 86, (12-13), 1908-1917.

5.   Gao, S. K.; Zhang, Y.; Meng, J. W.; Shu, J. A., Real-time analysis of soot emissions from bituminous coal pyrolysis and combustion with a vacuum ultraviolet photoionization aerosol time-of-flight mass spectrometer. *Sci Total Environ* **2009,** 407, (3), 1193-1199.

6.   Jonker, M. T. O.; Koelmans, A. A., Extraction of polycyclic aromatic hydrocarbons from soot and sediment: Solvent evaluation and implications for sorption mechanism. *Environ Sci Technol* **2002,** 36, (19), 4107-4113.

CHAPTER IV: DISCUSSION

4.1   Synthesis of Supported Metal Oxide Nanoclusters with Size-Controlled Approach

This study was to develop a synthetic route which can control the cluster size for metal oxide nanoparticles tethered to silica substrate (amorphous). The procedure was to prepare solutions of functionalized dendrimers with metal ions complexed in the interior of the dendrimers via the dendrimeric amine groups. The organic backbone of the dendrimers was then removed through high temperature oxidation, leaving the metal oxide nanoclusters chemisorbed on the silica surface. Several spectroscopic techniques, including transmission electron microscopy (TEM), X-ray photoelectron spectroscopy (XPS), X-ray absorption near edge structure spectroscopy (XANES), were used for the characterization of the materials. By changing the experimental parameters, a series of nearly monodispersed copper oxide nanoclusters were successfully prepared with tunable sizes ranging from 1-5 nm. This method was also experimentally proven to be valid in the preparation of other metal oxide nanoparticles, e.g., Ni and Fe, and with other oxide substrates, e.g., titanium oxide.

4.1.1   Determination of Calcination Temperature

In the synthesis of metal (oxide) nanoparticles via dendrimer-assisted technique, chemical reduction was commonly used to produce metal clusters with specific size depending upon the selected generation or substitution ratio of the dendrimer.[1-2] However, one of the disadvantages of the reduction method for nanocluster synthesis is the inability to completely remove the carbon skeleton from the nanoclusters. In some case, the uncoated metal oxide particulate matrix is necessary so that the presence of dendrimeric back-bone have to be avoided. For example, dendrimer-encapsulated metal particles supported on solid substrate shown no catalytic activity to bind CO molecules, as the dendrimer collapsed on nanoparticles and poisoned the metal surface.[3-4] In the study described here, oxidative thermolysis was used to

remove the dendrimer from substrate surface. Although high temperature can promote the carbon burn-off process, increasing temperature may also result in the increased mobility of the metal oxide nanoclusters and the consequently uncontrollable "growth" of particles. Therefore, it is critical to establish the preparative conditions at which all the material of dendrimer skeleton is being removed from the deposited nanoclusters. The temperature profile of the elemental composition of the 5 wt.% G4Cu16(II)/silica was obtained by XPS analysis, which was shown in **Table 3.1**. By 450 °C complete decomposition of the dendrimer structure occurred, as indicated by the disappearance of nitrogen and carbon peaks by temperature of 350 °C and 450 °C, respectively.

During calcination, the oxidation state of the copper cations could change as a result of possible reduction by reaction with carbonaceous species. However, analysis of the calcined CuO/silica nanoclusters using XANES and XPS indicated that the copper ions were in the oxidized form (cf. **Figure 3.1** and **Figure 3.2**). In the XANES spectra, both Cu(II)O standard and calcinated $G4Cu_{16}$ sample shown very weak or negligible peaks in the pre-edge zone (<8.99 keV), compared to Cu(I)O standard sample which shown prominent peak at 8.980 keV. Furthermore, the edge-energy of $G4Cu_{16}$ was the same to that of Cu(II)O at 8.999 keV, but significantly different from that of Cu(I) at 8.996 keV. The peaks positions read from the spectra of Cu(II)O and Cu(I)O standard samples were consistent to those reported results.[5] The similarity between the spectra of $G4Cu_{16}$ and Cu(II)O standard samples strongly suggests Cu(II)O is the dominant constituent of the nanoclusters present on the silica support. However, there were small differences between the spectra of Cu(II)O and $G4Cu_{16}$ when compared their "post-edge" region (> 9 keV). A broad peak at ~9.020 keV was present in the spectra of CuO standards, but not in the calcined $G4Cu(II)_{16}$ case. This result may indicate the existence of structural differences between the calcined $G4Cu_{16}$ materials and bulk CuO that may be due to

the size of the copper oxide clusters and/or interactions between copper and the silica support in calcined samples.

XPS supports the data obtained from XANES experiment. The presence of the $2p_{1/2}$ at 933.7-933.8 eV and the $2p_{3/2}$ peak 954 eV is characteristic of the copper (II).[6] Spectra of both samples prepared from the dendrimer-copper complex with n = 16 and n = 8 are indicative of the presence of Cu(II). However, the spectra of the sample obtained from the dendrimer-copper complex with n = 4 is indicative of presence of a mixture of Cu(II) and Cu(I). In this case, the $2p_{1/2}$ peak is broader and shifted towards lower binding energies (932.3 eV) typical of that of Cu(I).[7] The presence of the satellite peaks at 940.3 and 943.1 eV are uniquely characteristic for partially filled d^9 shell configuration in the ground state of Cu(II) ions. The peaks representative of the d^{10} configuration of reduced forms of copper were not present in the XPS spectra.[8] It is possible that Cu(I) exists in the calcined samples, as the $2p_{3/2}$ transition is broad; however, it is difficult to ascertain if any Cu(I) present in the calcined samples comes about from the synthetic process or from X-ray-induced reduction, as previously observed for Cu_2O particles.[7]

Based on the XPS and XANES results of copper oxide/silica samples, in addition with the referential consideration of the preparation procedure of impregnated copper oxide on silica in previous reported studies,[9-10] 450 °C was determined as the calcination temperature which not only served to completely remove the carbon backbone of dendrimer from the supporting surface, but also resulted the formation of copper oxide nanoclusters in the stable Cu(II) chemical states dominantly.

This thermal profile of calcination was also applied into all other preparation series of nanoclusters, including nickel and iron based nanocatalyst. XPS analysis confirmed that, similarly as in the case of G4Cu(II)$_n$/silica, the dominant composition in calcined G4Ni(II)$_n$/silica was NiO. Due to the low concentration of surface NiO of the nanoclusters samples, the $2p_{3/2}$

peaks 854.1~856.2 eV were not split as that observed in the NiO reference spectrum.[11] Similarly, XPS data indicated that the dominant form of iron was Fe_2O_3 in the nanoclusters samples.

4.1.2 Size Selected Manipulation of Metal Oxide Nanoclusters

The selection of Cab-O-Sil silica as the supporting substrate of metal oxide nanoclusters was based on the following concerns. Firstly, as the expected sizes of metal oxide nanoclusters were extremely small (1~3 nm), the supporting material need to be very thin and light dense to achieve an optimized contrast in TEM imaging. Cab-O-Sil meets both requirement. It should be noted that a non-aggregated, single Cab-O-Sil particle size is only 20~50 nm, which corresponding to the thinnest thickness of the substrate. Secondly, it was reported that dendrimers can be immobilized on the solid support including Si, Ti, and SiO2.[12-13] Therefore the use of Cab-O-Sil (amorphous silica) as support can minimize the agglomeration of dendrimer-metal complex in solution by the surface-precursor interaction (adsorption) and in later immobilize the metal oxide nanoparticles during calcination process due to its high surface/volume ratio (380 m^2/g). Thirdly, the chemical stability and inertia of Cab-O-Sil makes it suitable for calcination and catalytic test under high temperature. Furthermore, Cab-O-Sil silica was used previously as a surrogate of fly ash in the laboratorial combustion studies, which is also the proposed research field of making supported metal oxide nanoclusters.

The dendrimer-template synthesis method provided a unique opportunity to control the number of metal ions in one substituted dendrimer molecule. DAB dendrimers could form well-defined, stoichiometric complexes with various ionic metals, including Cu, Zn, Ni, Co.[14-15] As sub-stoichiometric ratios of the dendrimer substitution by metal ions also results in a uniform distribution of metal among precursor molecules in the solution, it is possible to tune the

nanoparticles size by using different substituted level dendrimer-metal complexes as precursors, assuming each single nanocluster was derived from a single substituted dendrimer molecule.

Initially, 4th generation DAB dendrimer substituted with copper was used as the precursor for the synthesis of CuO nanoclusters supported on silica. TEM images and statistical results of the size distribution shown in **Figure 3.6** of the CuO/silica system indicate size selective nanoclusters with low size dispersity (8-15% standard deviation) were synthesized successfully. The particle size distributions obtained from calcined $G4Cu_n$ samples with the dendrimer being fully (n = 16), half (n = 8) and quarterly (n = 4) substituted were compared in **Figure 4.1**. The most indicative conclusion from this comparison was the mean size of synthetic CuO nanoclusters is proportional to the copper substitution stoichiometry in precursor.

These measurements are consistent with the initial hypothesis that deposition of the dendrimer-copper complexes on silica followed by calcination will form monodispersed nanoclusters of copper oxide where the number of copper ions per dendrimer controls the size of the clusters. The 4th generation DAB dendrimer, with 32 terminal amino groups, can complex up to a maximum of 16 copper ions (2:1 ratio). Thus for the fully, half and quarter substituted dendrimers, one dendrimer–copper complex contains 16, 8, and 4 copper ions, respectively, and a single nanocluster on silica should also contain 16, 8 or 4 copper atoms depending on the stoichiometry of the dendrimer. However, the sizes of the nanoclusters are larger than anticipated. The Cu-O bond length in copper (II) oxide ranges from 0.195 to 0.216 nm.[16] Thus, a cluster of $[Cu_4O_4]$ should have a diameter in the order of 0.5 nm and, depending upon the geometry of the clusters, certainly no greater than 1 nm. The mean diameters of our $G4Cu(II)_4$/silica that theoretically contain 4 copper ions is 1.68 nm, which indicates that some aggregation is occurring. A similar conclusion can be reached for the theoretical 8 and 16

copper ion clusters. However, the extent of aggregation is small enough that narrow size distributions are still observed.
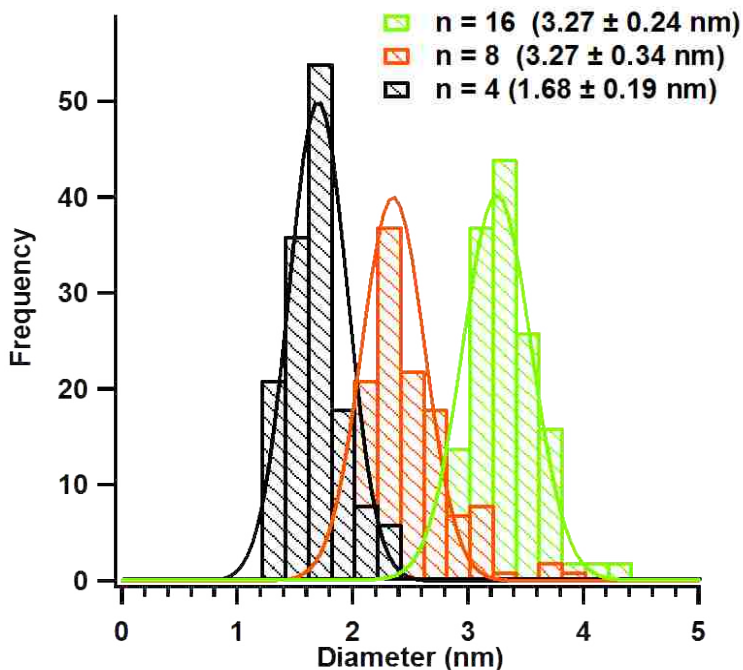
Figure 4.1 Size distribution of CuO nanoclusters derived from thermally treated (450 ºC, 5hours) DAB-Am32-Cu(II)$_n$/silica (n=16, 8, 4)

The deviation of the CuO cluster size from the theoretical assumptions indicated aggregation of the nanoclusters or dendrimer-Cu(II) precursor complexes. This could occur in solution, especially when the concentration of the dendrimer-Cu(II) complex was high, due to the evaporation of solvent. Another possibility was the aggregation of clusters on surface, as the mobility of adsorbed species was enhanced at elevated temperature.[17] In the traditional incipient-wetness method, the precursor is deposited on the substrate surface through the evaporation of solvent without further control. In contrast, the dendrimer-assisted formation of nanoclusters presumes adsorption of the dendrimer-copper complexes to the substrate surface is strong enough to immobilize the precursor until the calcination process is completed. Though the formation of CuO nanoclusters from a single dendrimer-copper complex molecule was

expected, the roughly 1.5-2 fold difference between theoretical and observed sizes indicates that either some aggregation of dendrimer-Cu occurred during the synthetic process or that some limited diffusion of Cu ions/CuO nuclei took place during calcination. In the case of nickel and iron oxide nanoclusters, we have obtained supporting evidence for the conclusion rooted on the results of copper. As seen in **Appendix 1-A and B,** both Ni and Fe nanoclusters show a positive relationship between the mean diameter and the metal ion number in substituted dendrimer precursor. The size distribution of iron oxide nanoclusters using $G4Fe(III)_{11}$ as the precursor is not a single peak. In fact, the two-peak size distribution seems to be a combination of the result of those of G4Fe(III)16 and G4Fe(III)8. This may imply that Fe^{3+} ions complexed with DAB dendrimer molecule in the same ratio as Cu and Ni, which is 1:2 for the number of metal ions to the number of amino ending groups.

To study the influence of metal loading on the sizes of metal oxide nanoclusters, $G4Cu_{16}$/silica samples corresponding to the copper oxide loading of 1 and 2 wt.% on silica were prepared. Compared to the 5 wt.% CuO sample, the sizes of CuO clusters had a noticeable 21% and 31% reduction for 2 wt.% and 1 wt.% samples, respectively. These results suggest that the surface concentration of particle precursors is one of the critical factors that influence the final size of the copper oxide nanoparticles. Higher surface concentration of Cu(II)-dendrimer that resulted in close proximities of adsorbed dendrimer-Cu(II) complexes appears to enhance the migration of copper species that resulted in larger CuO particles during calcination. However, these results indicate that this phenomenon could be limited if the surface concentration of the Cu(II)-dendrimer precursor is lowered.

As the formation of metal oxide nanoclusters is rooted from the decomposition of absorbed dendrimer-metal complex, it is essential to understand the interaction between dendrimers with supporting surface which greatly affect the size and shape of the clusters that

formed.[18] By impregnating the silica powder in the precursor solution, the individual dendrimer molecule can adhere to the silica surface and immobilize during the evaporation process and thermally heating. According to the report by Sun and Crooks,[19] there are two possible sources of strong interaction energies between the dendrimers and the silica surface. One of them is the electrostatic attraction between positively charged dendrimers (at neutral PH) and the negatively charged silica surface.[20] Another interaction source may arise from the hydrogen bonding of dendrimer onto the silica surface.[21] Due to the abundance of hydrogen atoms available at the peripheral of dendrimer, this type of interaction can be strong enough to force the spherical dendrimer structure to adopt an oblate shape when it is adsorbed. In this study we chose low concentration of metal oxide on surface from 1 wt.% to 5 wt.% so that a monolayer of metal oxide coverage was expected. However, the evaporation of solvent in preparation process has increased the concentration of dendrimer-metal precursor in solution and thus the agglomeration of dendrimer prior to their adsorption on solid substrate could not be avoided. Furthermore, the limited surface area of solid substrate (in silica case, 380 m^2/g) may incur a secondary agglomeration in which the absorbed dendrimer of surface may aggregate due to close space and weak interaction with solid support. The postulation of overlapped dendrimer as absorbate can explain the greater clusters size obtained from sample with higher percentage loading which means higher ratio of dendrimer-metal precursor to silica.

To enhance the adsorption of the precursor to the silica, a "pre-adsorption" procedure, adding a 24 hrs interaction of the precursor solution with the substrate prior to the evaporation process, was employed to allow the diffusion and equilibration of adsorption of the dendrimer-metal complexes on the silica surface. This procedure resulted a significant, 22 to 38% size reduction of nanocluster in the case of 5 wt.% CuO nanoclusters. (c.f. **Figure 3.8**). Considering the detection limit of instrument, the fact that no clusters were found in the case of

G4Cu4(II)/silica suggests that CuO nanoclusters were formed at a diameter below the 0.9 nm resolution of TEM.

Decreasing the concentration of $G4Cu(II)_n$ precursors on the surface of silica particles further decreases the size of the nanoclusters. For n = 16, reducing the dendrimer-Cu(II) complex loading corresponding to 1 wt.% CuO on the silica surface in conjunction with the pre-adsorption deposition method resulted in the formation of nanoclusters with a mean diameter of 1.55 nm. When applying this 1 wt.% concentration policy to the n = 8 and n = 4 substitution stoichiometries, the nanoclusters being produced were both below the 0.9 nm resolution of the TEM. These results suggested that both solution agglomeration of the dendrimer-Cu(II) complex in the final stages of impregnation and the surface concentrations of cluster precursors are critical factors that influence the final size of the copper oxide nanoclusters. Higher surface concentrations consequently resulting short separations between adsorbed dendrimer-Cu(II) complexes enhances the migration of copper and formation of larger clusters during calcination. This phenomenon can be limited if the surface concentration of the precursor is lowered. Similarly, avoiding a fast solvent removal during deposition of the dendrimer-Cu(II) complex on the surface matrix and allowing sufficient time for diffusion and pre-adsorption of the complexes on the matrix reduces the final size of the oxide clusters. As the bond of Cu-O of copper(II) oxide compounds range from 1.95-2.16 Å,[22] the 1.55 nm clusters size may be close to a 16 Cu ions structure, assuming a flat, "pancake-like" 3D shape of the cluster.

Increasing the calcination temperature resulted in a progressive disentanglement of the small metal oxide nanoclusters from the silica surface. As seen in **Figure 3.9a**, using 5 wt.% $G4Cu(II)_{16}$ as precursor, the higher the temperature, the greater the mean size of CuO clusters. This cluster "growth" approach was based on the fact that high temperature increases the mobility of nanoclusters which cause particle coalescence and growth.[23] Diffraction pattern

image of the large CuO clusters (> 5nm) indicated a polycrystalline structure, which was not observed on those samples calcined at 450 ºC. However, the increasing temperature of thermal treatment results in broader size distribution, though narrow distribution of cluster size is desired. With the temperature elevated, more crystal-like large clusters appear, suggesting more disordered clusters were replaced by ordered clusters (c.f. **Figure 3.9b**).

Two common mechanisms are known for the particle growth through sintering: Oswald ripening and particle migration and coalescence.[23] Particle migration/coalescence involves migration of multiple particles, while in Oswald ripening, molecules and atoms migrate along the surface to the immobile particle. The mechanism by which growth occurs can be distinguished by the shape of the particle size distribution. As depicted in **Figure 3.9a**, although most of the nanoclusters were 2-4 nm in diameter, the size distribution became broader and the percentage of larger particles increased. The positively skewed size distribution is characteristic for the particle migration and coalescence mechanism of growth.

Though most of the size-controlled preparations of the supported metal oxide nanoclusters were done on the ambient silica substrate, it is valuable to test the validity of this dendrimer-based synthesis of metal oxide nanoclusters on other supporting matrix. Titanium dioxide (titania) was initially chosen as another supporting substrate due to its wide application in catalysis industry. titania is well known as the support for the strong metal-support interaction. Compared to silica with inert properties as catalyst support, titania plays a more active role in catalyst system. Comparing the clusters size (5 wt.% CuO, "pre-adsorption", cal. at 450°C for 5 hrs) on two different substrate, silica (cf. **Figure 3.8a**) and titania (cf. **Figure 3.10**), it is evident that the type of the support used does not affect the size of the supported CuO nanoclusters. The slightly greater CuO cluster size (2.20 nm) of titania sample than that of silica sample may result from the smaller surface area of titania.

4.2 Comparison of Chlorinated Benzenes Reactions with Metal Oxide Catalyst Prepared by Dendrimer-Templated Method and by Incipient Wetness Impregnation

In order to address the issues of how the size of metal oxide clusters might affect the surface-mediated thermal degradation of hydrocarbons, silica supported metal oxide (CuO and Fe_2O_3) samples prepared in two different methods, dendrimer-based impregnation and incipient wetness, were used as the representatives of nano-size catalysts and coarse catalysts, respectively. Monochlorobenzene and dichlorobenzene were chosen as the model compounds for studies due to their presence in incinerators and similar structure to most toxic polychlorinated aromatic compounds, PCDD/Fs. All thermal reactions were conducted in a high temperature reactor under pyrolytic and oxidative conditions. Analysis of the reaction products using GC-MS indicated all the nano-size catalysts showed superior catalytic activity than their coarse analogues on the conversion of chlorinated benzenes under both pyrolytic and oxidative thermal condition. Furthermore, such catalytic size effect was also observed on the selectivity of products yields.

4.2.1 Copper Oxide Mediated Degradation of 1,2-Dichlorobenzene

It is known that transition metal or metal oxide could mediate the decomposition of hydrocarbon under thermal condition.[24-26] In the studies described here, using CuO/silica as the reaction bed resulted in the ~100% conversion of o-DCBz at temperatures of 450 to 550 °C, compared to only 8% and 2% conversions at 550°C when using only silica as the reaction bed and empty quartz tube, respectively. Surface-mediated oxidation of o-DCBz or further reaction to form other products could have been initiated by the chemisorption of o-DCBz at copper hydroxide or copper oxide sites through the elimination of one or two HCl molecules (cf. **Figure 4.2**).[27] This process resulted in a surface-adsorbed chlorophenolate or bidentate which was chemically bound to a Cu(II) site.
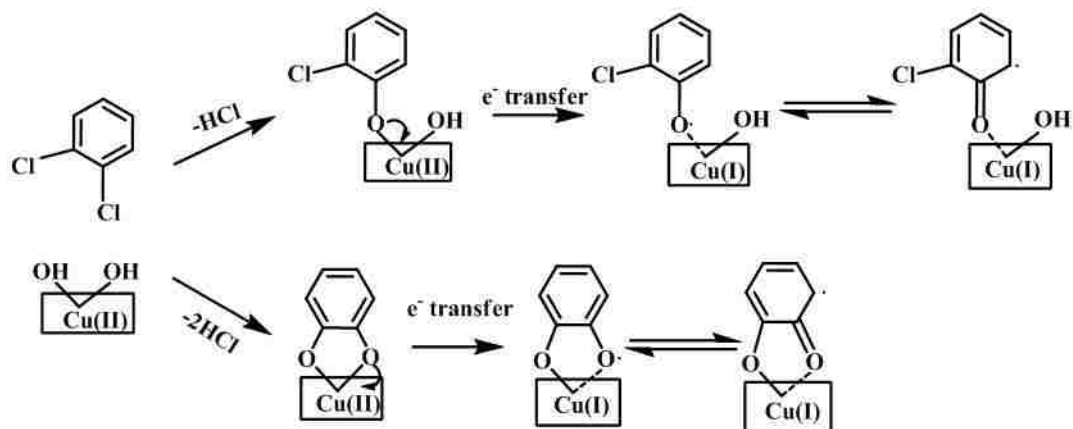
Figure 4.2 Scheme for chemisorption of o-DCBz on CuO/Silica

In the pyrolytic reaction of o-DCBz with copper oxide catalysts, a typical sigmoid shaped dependence for the conversion with respect to temperature was observed (cf. **Figure 3.11**). Much higher conversions of o-DCBz were observed for the nano-size copper oxide catalysts, G4Cu$_{16}$, G4Cu$_8$, and G4Cu$_4$, than for IMPCu. However, no conclusive correlation between activity and particle size can be drawn from the conversion and product yields of these three nano-size samples. Deviations in their cluster sizes (~1-4nm) may affect the results. Because no conclusive correlation can be determined, the following discussions about the activity of nano-size catalysts are based on the average of these three G4Cu$_n$ samples. Since all experiments for each of the catalysts were performed using identical conditions, the observed difference in activity is attributed to the properties of the catalyst itself. Three potential that may influence the difference in activity are: 1) availability of active sites on the catalyst surface, 2) activation energy for transformation of adsorbed organic species and subsequent reactions, and 3) rate of oxygen diffusion from the interior layer to the catalyst surface.

As Cu-O is the active site in the reaction with o-DCBz, the more Cu-O sites present on the catalyst surface, the more o-DCBz can be adsorbed for decomposition or further reactions. Therefore, for the same amount of copper oxide loading, G4Cu$_n$ catalysts naturally have higher

114

surface density of Cu-O sites than that of IMPCu, the former having a smaller average cluster size of copper oxide. Furthermore, the difference of catalyst structure properties may also affect the reactivity of copper oxide catalysts. According to the Mars-van Krevelen (MvK) mechanism and other preceding studies,[10, 26] surface-bound oxygen may play a key role in the surface-mediated degradation of o-DCBz. The formation and desorption of phenoxyl radicals and their derivatives through select pathways caused the depletion of surface-bound oxygen. As indicated by the XRD results (**Appendix 3**), the only dominant form of CuO in G4Cu$_n$ samples was amorphous dispersed nano-size metal oxide clusters (< 5 nm), in contrast to the presence of large (~50-1000nm) CuO crystalline particles in the IMPCu sample. It is known that the diffusion of oxygen is limited in a solid with crystalline structure due to its ordered structure.[28] Therefore the rate of replacing consumed oxygen on surface is lower in IMPCu catalyst, and so is the activity of o-DCBz decomposition. Although it was reported that subsurface oxygen ions from up to 500 monolayers could participate in the reaction occurring on the surface,[29] the movement of internal atoms/ions from a deeper layer to the surface is always more difficult because this process is energy driven. Therefore, the smaller the clusters (shorter average distance from cluster inner to surface), the less energy (lower reaction temperature) is required for transporting internal oxygen to surface. This size effect makes G4Cu$_n$ more active in the surface-mediated reaction because the extremely small cluster dimensions ensure the easy replacement of oxygen on the surface at relatively low temperatures (250 to 450 °C). This hypothesis is supported by the higher yield of oxygenated hydrocarbon, including phenols, benzofuran and dibenzofuran, from the reaction over G4Cu$_n$ than from the reaction over IMPCu.

Reactions conducted at higher temperatures from 500 to 550 °C indicated that the degradation of o-DCBz on IMPCu was significantly more complete than reactions conducted at lower temperatures, with 99% conversion at 550 °C. Higher temperature reactions showed no

observable difference between reactions over G4Cu$_n$ and reactions over IMPCu. This can be attributed to two effects: the increased turnover frequencies (TOFs) of surface-mediated reactions and the involvement of larger particles for reactions that are not activated at low temperatures. At lower reaction temperatures (250 to 450 °C) where low TOFs are dominant, the limited reagent is the copper oxide catalyst. Under these conditions, the conversion of o-DCBz over G4Cu$_n$ was significantly higher than that over IMPCu catalyst. At higher reaction temperatures (500 to 550 °C), high TOFs of catalysts make o-DCBz a relatively limited reagent in reactions with both G4Cu$_n$ and IMPCu. In this case, all of the injected o-DCBz decomposed in the given contact time (~0.01 s). This assumption is supported by the study using FTIR spectroscopy to investigate the adsorption of chlorophenol on silica. This study indicated that the rate of chlorophenol chemisorption on the surface increased as temperature increased.[9] Furthermore, as IMPCu catalyst was composed of various size particles from 1 to 1000 nm, its large crystalline CuO clusters may not be as active as smaller clusters due to the higher activation energy required for low temperature reactions. However, as the temperature was increased to 500 °C or higher, these large CuO clusters could be activated to mediate the decomposition of o-DCBz.

Various hydrocarbon products were formed from the surface-mediated decomposition of o-DCBz. Among these products, benzene was produced with the highest yield (~1.6% on G4Cu$_n$ catalysts), and was significantly greater over G4Cu$_n$ (>10x) than the benzene produced from IMPCu. The formation of benzene at temperatures as low as 250 °C indicates that the bidentate species was already formed below this temperature. The cleavage of two C-O bonds followed by scavenging of two H· led to the release of benzene with a maximum yield at 500 °C. Meanwhile, the cleavage of one C-O bond and one Cu-O bond followed by scavenging of one H· formed phenol.[30] **Figure 4.3** depicts the purposed mechanism for formation of benzene and phenol.

The higher yields of both benzene and phenol from reactions with nano-size CuO of G4Cu$_n$ than those from coarse particle surrogates of IMPCu can also be attributed to the greater number of active sites (Cu-OH) for o-DCBz absorption presented in nano catalysts. Furthermore, though the formation of benzene and phenol is competitive, the higher yield of the benzene indicates that C-O bond cleavage is more likely to occur than Cu-O bond cleavage due to the relatively stronger Cu-O bond.[31] This assumption is also supported by the non-detection of catechol, the formation of which requires the cleavage of both Cu-O bonds.
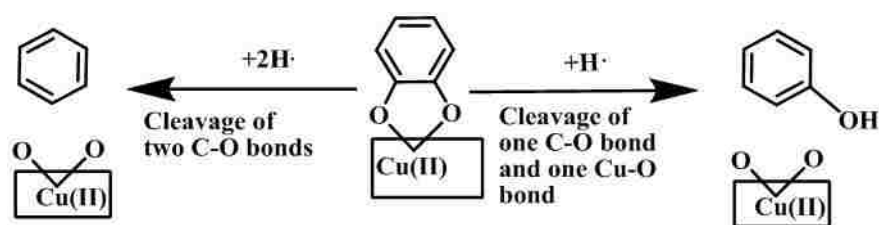
Figure 4.3 Schematic formation of benzene and phenol on CuO/silica

Chlorobenzene formation can be initiated through the formation of surface-bound chlorophenolate which is shown in the upper pathway in **Figure 4.2**. Though it is similar to the formation of benzene in its cleavage of C-O bond and scavenging of H·, chlorobenzene is formed and dissociated from the surface with a maximum yield at a significantly lower temperature (350°C) than that of benzene. This may correlate to the ease of formation of chlorophenolate which only needs single HCl elimination, as opposed to the formation of phenolate which needs double HCl elimination.   It is noteworthy that the maximum yield of chlorobenzene from G4Cu$_n$ is only 2.8x the yield from IMPCu, compared to > 10x difference in the benzene yields between these two types of catalysts.   This less significant size effect of chlorobenzene formation indicates that other mechanisms may be involved, counteracting the influence of the availability of active sites.   One possibility is that the surface hypochlorite species may increase the chlorination of adsorbed phenoxyl radicals.[32]   This increased chlorination is due to surface

117

chloride ions acting as highly effective chlorinating agents, and the rapid exchange between the organic phase and surface chlorides.[33] The result suggests that the chlorinating surface-bound organic species may give larger Cu-O particles an advantage over their smaller analogues, which to some degree offsets the size effect on product formation. This argument is rational because this surface-mediated chlorination is a multiple-step reaction involving multiple active Cu-O sites, and therefore needs a larger functioning active center than reactions for simple adsorption and desorption only. Consequently, not all of the nanoclusters have enough Cu-O sites to be functioning active centers for this chlorination process.[34] Larger clusters, which have relatively infinite Cu-O sites on surface, are more likely to possess these functioning centers for chlorination. This hypothesis is supported by the higher yield of polychlorinated benzene on the IMPCu catalyst. **Figure 4.4** shows the potential mechanism of chlorobenzene and polychlorinated benzene formation adapted from previous studies of 2-chlorophenol which is structurally similar to o-DCBz.[30, 32]
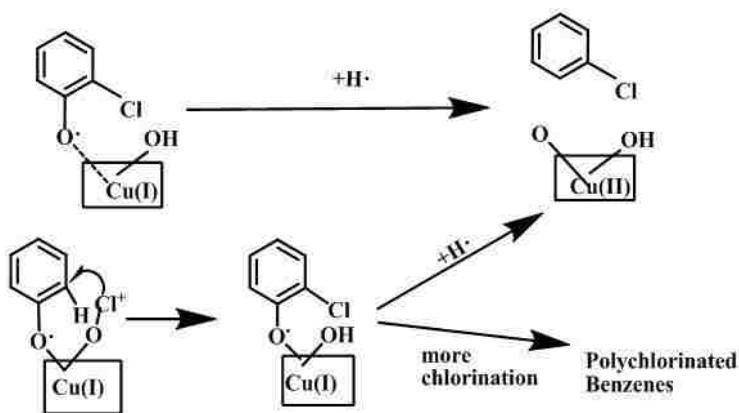
Figure 4.4 Schematic formation of chlorobenzene and
polychlorinated benzenes on CuO/Silica

Dibenzofuran (DF) is the only detectable PCDD/Fs products from the reaction between o-DCBz and CuO catalyst. **Figure 4.5** illustrates the proposed Langmuir-Hinshelwood mechanism for DF formation, adapted from a previously proposed mechanism for the formation

of DCDF and MBDF.[26, 32] Since DF formation is derived from the condensation reaction of surface-bound phenoxyl radicals (or keto mesomers), it is logical that a higher yield of DF was observed in the catalytic reaction of G4Cu$_n$, and the yield of DF appears to be consistent with the cases of benzene and phenol formation as discussed previously.
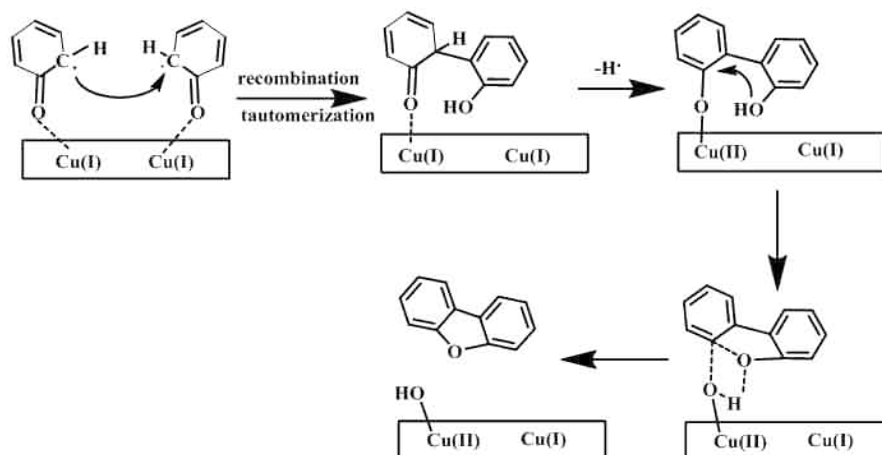
Figure 4.5 Schematic formation of Dibenzofuran on CuO/Silica

Fewer products were observed in the oxidative reactions, as the presence of oxygen in carrier gas promoted the degradation of o-DCBz more completely than did pure helium in pyrolytic conditions. Though the trend of o-DCBz conversion as it relates to temperature shows a similar sigmoid shape, the addition of oxygen did cause these conversion plots to shift ~50°C to lower temperature compared to their pyrolytic analogues. This observation indicates that supplying gas phase oxygen lowered the energy onset of o-DCBz conversion. Copper oxide sites on silica surface can be regenerated by O$_2$ after the consumption of oxygen from previous reactions. This regeneration by O$_2$ occurs more readily than the transfer of oxygen from internal layers of particles to particle surface.

Compared to the pyrolytic condition, the yields of polychlorinated benzenes and the degree of chlorination were both increased under oxidative conditions, suggesting that oxygen

plays an important role in the chlorination process. The effect of oxygen is evident in the promotion of the formation of surface hypochlorite species and the subsequent increase of chlorinated products in the presence of gaseous oxygen.[32] As in the pyrolysis results, oxidative conditions also exhibited a higher yield of polychlorinated benzene on the IMPCu catalyst. Again, these results can be directly related to larger clusters that have more functioning center for the multi-step reaction of chlorination.

It is remarkable to note that the products of incomplete oxidation, tri- and tetra-chloroethylene, were found with significantly greater yields ($> 5x$) over G4Cu$_n$ (max. 0.11% and 1.1%, respectively) than over IMPCu (max. 0.022% and 0.32%, respectively). This phenomenon can be attributed to the availability of individual Cu-O cluster active sites. Because degradation of hydrocarbon on catalytic surface is generally a multi-step reaction, the availability of active sites in a single cluster may determine the extent of decomposition. For micron or submicron particles with thousands of active sites on the surface, complete decomposition of adsorbed hydrocarbon molecule is likely. However, when the particle size is reduced to only a few nanometers, availability of active sites of an individual particle may be very limited, and the decomposition of hydrocarbon may end with the formation of incomplete oxidation products. As ethylene is one of the typical products from the oxidative decomposition of benzene or chlorobenzene[35-36], it is reasonable to propose that o-DCBz oxidized by G4Cu$_n$ catalysts may initially form partial decomposition products such as ethylene or chlorinated ethylene. Before further oxidation as CO, CO_2 and H_2O on the same nanocluster, these ethylenes can be desorbed from surface to gas phase. Due to the detection limitations of the GC/MS (min. amu. 40), ethylene and other small fragments, such as methane and acetylene, were not monitored in the GC/MS analysis.

4.2.2 Iron Oxide-Mediated Degradation of 1,2-Dichlorobenzene

Since iron is similar to copper as redox transition metal, its hydroxide or oxide compounds were also expected as the active chemisorption sites for o-DCBz with similar proposed mechanism (cf. **Figure 4.6**).
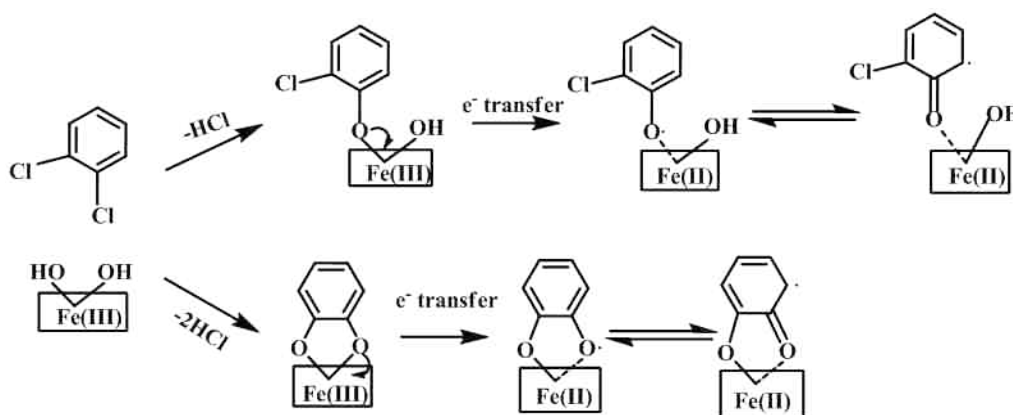
Figure 4.6 Scheme for chemisorption of o-DCBz on Fe_2O_3/silica

The activity performance of iron oxide catalysts was similar to that of copper oxide in the reaction with o-DCBz. Under pyrolytic condition, more than 90% of o-DCBz was decomposed over all three $G4Fe_n$ catalysts at temperature 450 to 500 °C, which was ~50 to 100 °C lower than that on IMPFe sample. This result was expected as the iron oxide clusters sizes of $G4Fe_n$ were 1~4 nm, which is comparable to those of $G4Cu_n$. Since coarse iron oxide particles IMPFe were prepared by the same impregnation method as that for copper oxide analogue, its average size was believed to be the same scale as IMPCu.   Therefore the particle-size effect of o-DCBz decomposition over iron oxide samples can be explained by the same reaction proposed for copper oxide.

Formation of benzene over iron oxide catalysts can be proposed with the same mechanism depicted in **Figure 4.3**, except replacing Cu(II) as Fe(III). Similar to the reaction over copper oxide catalyst, the yield of benzene over nano-size catalysts of $G4Fe_n$ is significantly

higher (10x) than that from IMPFe. Combined to the high yield of chlorobenzene, it is evident that the chemisorption of o-DCBz on iron oxide surface undergoes two pathways shown in **Figure 4.6**: (1) formation of 2-chlorophenoxyl via single HCl elimination, and (2) formation of bidentate species via double HCl elimination. Though both iron and copper oxide catalysts exhibited higher benzene yields over their nano-size catalysts than their coarse analogues, in general iron oxide was more favored by the formation of benzene, especially under high reaction temperature (500~550 °C) conditions. **Figure 4.7(a)** compares the benzene yield between these two different metal-based catalysis cases. The maximum yield of benzene from reaction over iron oxide at temperature 500~550 °C is 3x higher than that over copper oxide for both nano-size and impregnation catalysts cases, in contrast to their smaller differences from 250~450 °C. The significant formation of benzene over iron oxide suggested the ease of scission of C-O bonds of the absorbed phenoxide, which can be correlated to the stronger oxidative properties of Fe_2O_3 than CuO.
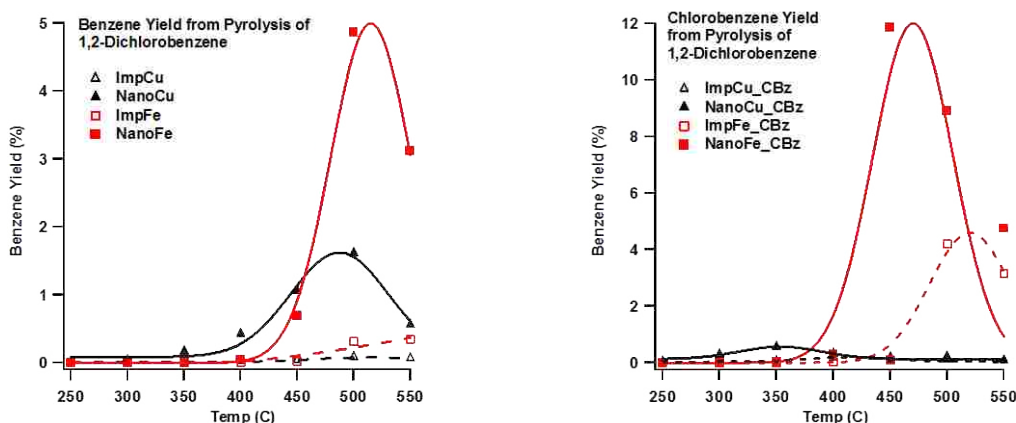
Figure 4.7 Comparison of **(a)** benzene and **(b)** chlorobenzene yields from pyrolysis of o-DCBz over Fe_2O_3/silica and CuO/silica surfaces

Furthermore, iron oxide catalysts were found to be more favored by the chlorobenzene formation than copper oxide catalysts, as indicated by **Figure 4.7(b)**. The yields of

chlorobenzene over G4Fe$_n$ and IMPFe catalysts were 10x greater than that over their copper based analogues. This result is in contrast to the benzene case, in which the yield of benzene is more comparable (3x) between reactions over iron and copper based catalysts. According to the discussion for copper oxide catalysts, the surface-mediated formation of chlorobenzene can be contributed by two proposed pathways: 1) formation and desorption of chlorophenoxide absorbate, 2) chlorination of surface bound phenoxide. These two mechanisms, as well as a pathway for formation of polychlorinated benzenes which is similar to that for copper oxide catalysts, are depicted in **Figure 4.8**.
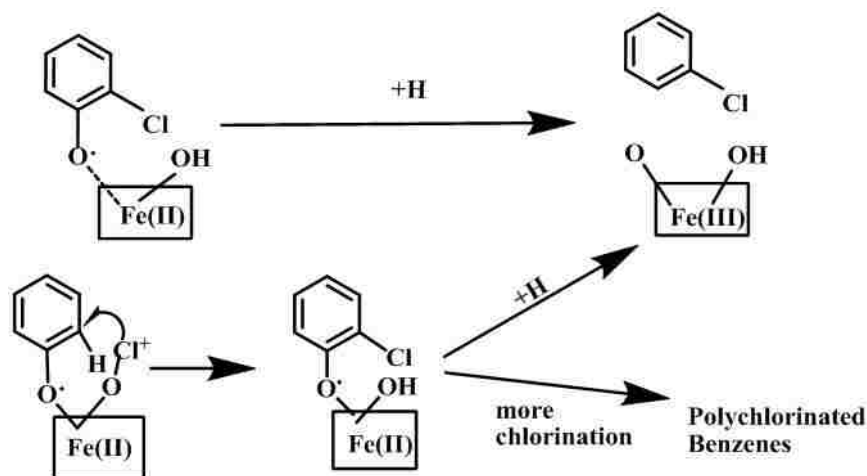
Figure 4.8 Schematic formation of chlorobenzene and polychlorinated benzenes over Fe$_2$O$_3$/silica

However, when considering the results of polychlorinated (Cl > 2) benzenes yields, which was >10x greater over iron oxide catalysts than those over copper oxide, the chlorination mechanism seems more dominant. The extraordinary chlorination ability of Fe$_2$O$_3$/silica can be correlated to its stronger oxidative properties than CuO/silica at high temperature range >500 °C. Observation of chlorophenol and 2,6-dichlorophenol as products in the reaction of o-DCBz with

123

iron oxide also adds evidence of the superior chlorination capability of iron oxide, as no chlorinated phenols were detected in the copper catalysis case.

Similar to reaction over copper oxide catalysts, the addition of oxygen in carrier gas did promote the decomposition of o-DCBz over iron oxide catalysts in comparison with those under pyrolytic condition. At 450 °C, the conversion of o-DCBz gain 8% and 31% increase for G4Fe$_n$ and IMPFe, respectively. Chlorinated ethylenes and benzenes were the only products detected by GC/MS. The fewer productions formation than those formed in pyrolytic reaction indicated the decomposition of o-DCBz was more complete when gaseous oxygen was presented. Although the interpretation to products formation over iron oxide mediated oxidation is very similar to those for copper oxide, the remarkable difference is the yield of chlorinated benzenes is much less in the iron case for oxidative conditions, in contrast to the results obtained from pyrolytic condition. This discrepancy can be explained that the presence of gaseous oxygen enhanced the oxidative properties of iron and resulted in the readily decomposition of chlorinated products, which are difficult to degrade generally.

4.2.3   Iron Oxide-Mediated Degradation of Monochlorobenzene

MCBz is structurally similar to o-DCBz but with only one chlorine substituent. It is reasonable to propose a similar mechanistic chemisorption of MCBz at iron hydroxide sites through elimination of HCl and the sequent formation of surface bound phenolate (cf. **Figure 4.9**). Decomposition of MCBz over iron oxide catalysts under pyrolytic condition showed Sigmoid shape temperature dependence which is similar to that of o-DCBz decomposition. The result of MCBz conversion depicted in **Figure 3.15** indicated the nano-size catalyst was more active in MCBz degradation as the overall conversion trends of G4Fe$_n$ is about -50 °C lower than that of IMPFe. This superior activity of G4Fe$_n$ is attributed to its larger number of available copper hydroxide, lower active energy and higher TOFs as discussed in **section 4.2-1**.
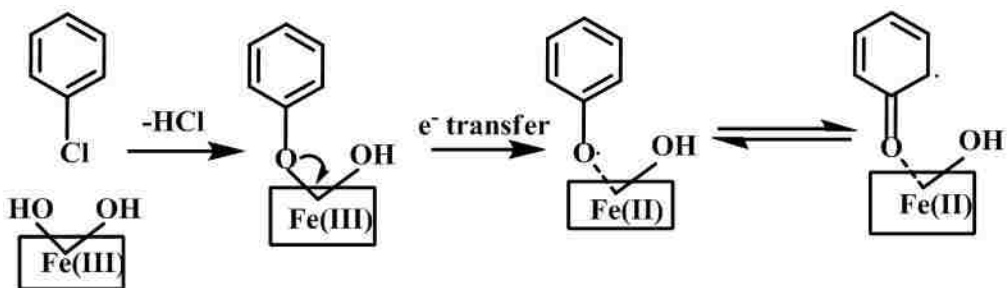
Figure 4.9 Scheme for chemisorption of CBz over Fe_2O_3/silica

Benzene is the most dominant products with maximum yield 44% at 500 °C in $G4Fe_n$ case and 15% at 550 °C in IMPFe case. Compared to its formation from reaction of o-DCBz which required double cleavage of C-O bond from the surface bound bidentate, the formation of benzene is much easier as the surface bound phenolate resulted from the chemisorption of MCBz on surface required only single cleavage of C-O bond following by scavenging of H (cf. **Figure 4.10**). As phenolate is the only surface bound species resulting from MCBz chemisorption, and benzene is the only product resulting from the cleavage of C-O bond of phenolate, the formation of benzene was therefore observed with such prominent yield. Consistent to the observation of o-DCBz reaction over iron oxide, the nano-size iron oxide clusters, $G4Fe_n$, exhibited higher activity in the formation of benzene than IMPFe did.
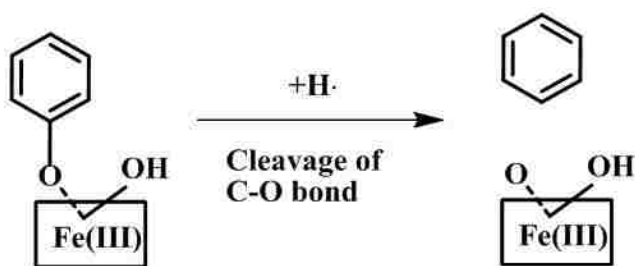
Figure 4.10 Schematic formation of benzene from CBz reaction over Fe_2O_3/silica

125

Phenol was observed as products in the reaction of MCBz over iron oxide catalysts. Its formation was proposed through a similar mechanism as discussed in o-DCBz cases. Surface bound phenolate was transformed to be gas phase phenol through the cleavage of its Fe-O bond followed be scavenging of one H·. Similar to benzene, phenol is also the direct product from the desorption of surface bound phenolate. Therefore, it was expected that the yield of phenol would be similar to benzene which was significantly higher in MCBz reaction than in o-DCBz reaction. However, this was not the case for phenol. The maximum yield of phenol formation was only ~0.3% from MCBz reaction, compared to as high as ~1.5% from o-DCBz reaction. This may be caused by the dominant formation of benzene which was directly competed to the formation of phenol. Such competition also reduced the significance of size dependence of catalysts on phenol formation, which was not as distinguishable as those of o-DCBz reactions.

1,2-dichlorobenzene was the only chlorination products observed in MCBz reaction. This may be due to the less abundance of chlorine ions as MCBz only contains one chlorine ion and DCBz has two. Such lower degree chlorination was also observed in oxidative reaction of MCBz, where only trichloroethylene was observed instead of both tetra- and tri- chloroethylene in o-DCBz case.

4.3   Flow Reactor Studies of Soot Formation Mediated by Metal Oxide Nanoparticles

Soot formation was thought to be a high temperature gas-phase reaction. Under fuel rich condition, the formation of soot is even more favored, accompanied by the formation of polycyclic aromatic hydrocarbons (PAH).[37] The pathway to the formation of large PAH was known through the recombination of small unsaturated hydrocarbon species, e.g. C_2H_2, which was produced with the breaking down of fuel molecules.[38] However, the conversion of PAH to soot is still unclear. It was proposed that a condensed nucleus is needed to form particulate matter via K-V mechanism. Though mostly SO_4^{2-} had been thought to be the composition of this

type of particles, the role of cation has been proposed also.[39] It has been reported recently that metal species were found in the emitted carbonaceous particulate matter from the heavy oil combustion.[40] The remarkable feature of this finding was the concentration of metal shown increase with the decrease of particle size. Specifically, as the particle size decreased below about 2 microns into the submicron range, the concentration of transition metals, Zn, Ni and Fe increased exponentially to greater than 60% and the carbon concentration decreased from nearly 90% to less than 30%. This result provided evidence that cations type particles can be the likely source of condensation nuclei for soot formation.

Though many studies regarding soot formation were performed in flaming combustion, there are some limitations in the control of reaction conditions, e.g. temperature, stoichiometric ratios of fuel/oxygen. An alternative approach to quantify soot formation is to utilize a flow reactor, which could provide an accurate solution to control the experimental condition of combustion. However, it is in general more difficult to produce soot using a flow reactor than open flame. To reduce the difficulty to observe soot formation, high sooting fuels were preferred in the initial flow reactor experiments. The sooting tendency of hydrocarbon fuel commonly used in combustion studies can be arranged in sequence: methane < ethylene < acetylene < benzene < toluene < naphthalene < anthracene < pyrene.[41] However, the last three sooting candidates are in solid form under room temperature, which is not suitable for quantitative injection using syringe. Therefore, 1-methylnaphthalene was selected due to its structural similarity to naphthalene but in liquid phase under room temperature.

The preliminary studies using the two-zone flow reactor system indicated high temperature and sub-stoichiometric (fuel rich) condition was favored by soot formation. At temperature lower than 1000 °C, no soot formation was observed even at the highest tested C/O (= 5) condition. The most remarkable feature of these results was that the presence of metal

127

oxide nanoparticles did increase the production of soot particles. In addition to the visual observation of solid carbonaceous materials which deposited on the wall of the flow reactor, the identity of the condensable substances as soot was confirmed using TEM (cf. **Figure 3.21** and **Figure 3.22**). The micrographs in this figure clearly show typical soot particles with diameter <50 nm that are aggregated into chains of a few 100 nm in length. The semi-crystalline, pseudo-onion skin structure ascribed to individual soot nanoparticles is evident. The increasing d_{002} spacing of the graphitic domains may indicate a relatively poor coordination between the graphitic layers in the soot microstructure.[42]

     Figure 3.23 shows the most dominant forms of carbonaceous materials formed at temperature of 1100 °C with various C/O ratios from 1.4 to 5. It can be seen that the less oxygen was supplied, the more condensable materials like soot were formed. Compared the combustions with iron addition to those without iron addition, the formers shown higher tendency to soot formation, as indicated by its observation starting from a relative smaller C/O value (C/O = 2.0) than that of the non-iron case (C/O = 2.5). Under same oxygen concentration, the combustion with iron involved did produce more soot or soot like black carbon which was indicated by the thicker deposit at the outlet and the greater particles population through TEM observation. This conclusion was also supported by the results of UV-Vis experiments performed by other colleague in our lab. By measuring the absorbance of particles collected under 1100°C, the higher absorbance with metal presence indicated higher yield of soot formation. However, the microstructure of soot particles obtained from these two cases shows no distinct difference under TEM analysis, as indicated by **Figure 3.21** and **Figure 3.22**. .

     Figure 4.11 depicted the absorbance of soot with regard to the ratio of metal/fuel at temperature 1100 °C. With the increase of metal in combustion, the formation of soot was increased too. Furthermore, the higher C/O ratio also promoted the formation of soot, which was

consistent to the observation in TEM studies. However, when C/O ratio was maintained at 2.5 or higher, the absorbance was not close to 0 even no metal was added to combustion in blank experiments. This result indicated other sources of metal were available in the flow reactor system other than that from the injection of metal precursor. For example, the gas cylinder used in experiment may release trace metal species to the system through the delivery of gas stream.

The presence of metal oxide nanoparticles not only promote the formation of soot, but also the formation of PAH compounds, which was suggested by the GC/MS results. Chemical analysis (GC/MS) of the extractable organic materials from soot revealed the presence of the typical array of PAHs in combustion (c.f. **Figure 3.23**). With the addition of metal, the relative total yield of PAH (amu < 250) was increased. **Figure 4.12**depicted this effect of metal addition on PAH formation.
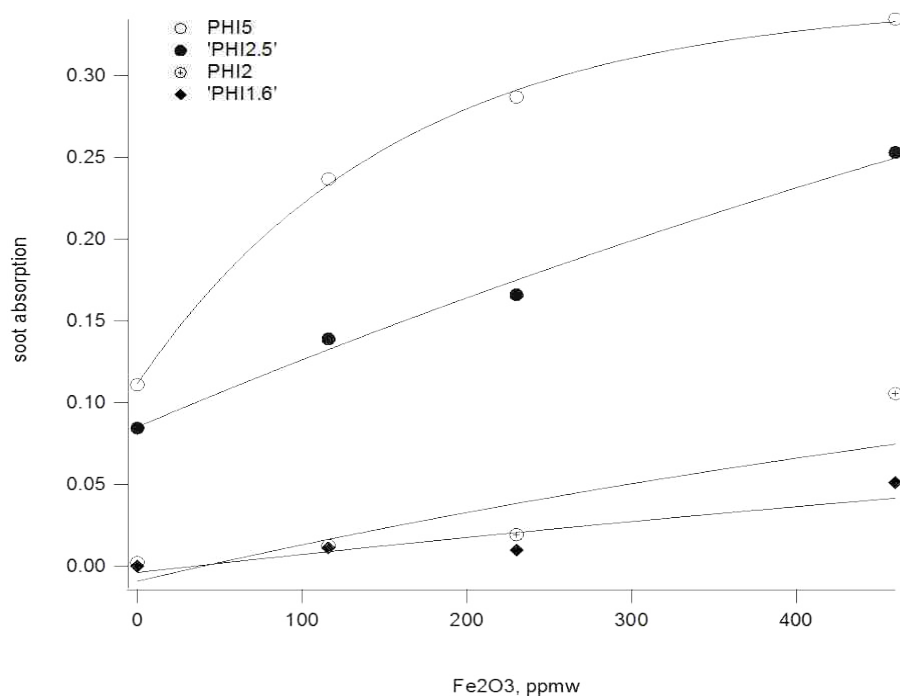
Figure 4.11 UV absorbance of Soot formation with regard to the metal/fuel concentration (0 to 500 ppmw) and C/O (Phi) ratio from 1.6 to 5
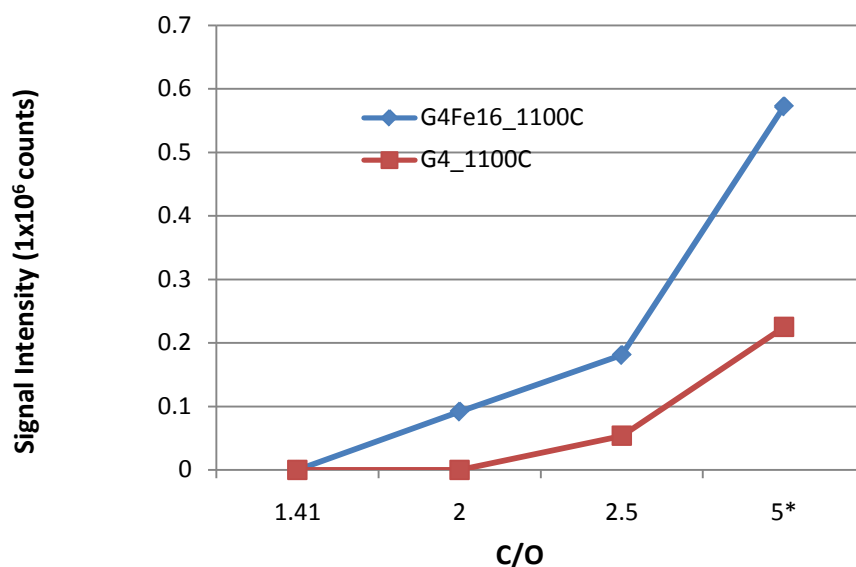
Figure 4.12 The relative intensity of total extractable carbon from soot
which was formed at 1100 °C with or without metal addition

The custom-designed-and-built flow reactor was used for all experiments. One of the significant features of this system was that quantitative metal oxide species in the form of nanoparticles can be directly introduced into the combustion process of hydrocarbon fuel. Methanolic solution of dendrimer-metal complex was chosen as the precursor of metal oxide nanoparticles, due to the unique feature of dendrimer which can coordinate metal ions stoichiometrically. Ideally, the dendrimeric backbone of these metallic compounds could be decomposed as gaseous species (mostly are CO_2 and H_2O) through thermal oxidation, while the enclosed metal was oxidized and condensed to a nanoparticles. Indeed, 1-3 nm metal (oxide) nanoparticles were produced with the thermal treatment, as seen in Figure **3.17 to 3.18**. However, at the lower temperature 500 °C, even 600 °C, dendrimer was not completely burned-off, which was indicated by the carbonaceous residual on TEM grids. Since the goal of this project was to investigate the effect of metal oxide on soot formation, the unburned organic ligand portion of dendrimer may add more complicate assumption to the model for study.[42]

Therefore, the generation of "clean" (no organic content) metal oxide nanoparticles is critical important. By increasing the temperature to 700 °C, no carbonaceous particulate matter, except the nonvolatile metal oxide nanoparticles, was observed under TEM. Increasing temperature also resulted in the growth of metal oxide particles. This effect was implied by the fact that particles collected at 700 °C were slightly larger than those collected at 600 °C. Such growth trend is more evident when temperature increased to 900 °C, where copper oxide particles with size ~50 nm were produced and exhibited crystalline structure (c.f. **Figure 3.19**). This phenomenon can be attributed to the fact that increasing temperature increases the opportunities of particles collision in a limited space and thus particle growth because of their aggregation. A recent combustion study on heavy oil has provided implicit data that combustion generated particles had core composed of metal nanoparticles of < 10 nm.[40] This is a reasonable size for metal oxide nanoparticles formed through the pathway of evaporation (flame zone) and condensation (post-flame zone). To mimic the real-world combustion process, we chose to work at 700 °C to produce non-carbonaceous-residual metal oxide nanoparticles (1~3 nm) for the hydrocarbon combustion studies.

4.4   References

1.   Knecht, M. R.; Garcia-Martinez, J. C.; Crooks, R. M., Synthesis, characterization, and magnetic properties of dendrimer-encapsulated nickel nanoparticles containing < 150 atoms. *Chemistry of Materials* **2006,** 18, (21), 5039-5044.

2.   Esumi, K., Dendrimers for nanoparticle synthesis and dispersion stabilization. *Colloid Chemistry Ii* **2003,** 227, 31-52.

3.   Lang, H. F.; May, R. A.; Iversen, B. L.; Chandler, B. D., Dendrimer-encapsulated nanoparticle precursors to supported platinum catalysts. *Journal of the American Chemical Society* **2003,** 125, (48), 14832-14836.

4.   Liu, D. X.; Gao, J. X.; Murphy, C. J.; Williams, C. T., In situ attenuated total reflection infrared spectroscopy of dendrimer-stabilized platinum nanoparticles adsorbed on alumina. *Journal of Physical Chemistry B* **2004,** 108, (34), 12911-12916.

5.	Drake, I. J.; Fujdala, K. L.; Baxamusa, S.; Bell, A. T.; Tilley, T. D., Effects of Precursor Composition on the Local Structure of Cu Dispersed on Mesoporous Silica: A Detailed X-ray Absorption Spectroscopy Study. *J. Phys. Chem. B* **2004,** 108, 18421-18434.

6.	Chase, P. A.; Gebbink, R. J. M. K.; van Koten, G., Where organometallics and dendrimers merge: the incorporation of organometallic species into dendritic molecules. *Journal of Organometallic Chemistry* **2004,** 689, (24), 4016-4054.

7.	Wu, C. K.; Yin, M.; O'Brien, S.; Koberstein, J. T., Quantitative analysis of copper oxide nanoparticle composition and structure by X-ray photoelectron spectroscopy. *Chemistry of Materials* **2006,** 18, (25), 6054-6058.

8.	Gan, Z. H.; Yu, G. Q.; Tay, B. K.; Tan, C. M.; Zhao, Z. W.; Fu, Y. Q., Preparation and characterization of copper oxide thin films deposited by filtered cathodic vacuum arc. *J Phys D Appl Phys* **2004,** 37, (1), 81-85.

9.	Alderman, S. L.; Dellinger, B., FTIR investigation of 2-chlorophenol chemisorption on a silica surface from 200 to 500 degrees C. *J Phys Chem A* **2005,** 109, (34), 7725-7731.

10.	Lomnicki, S.; Truong, H.; Vejerano, E.; Dellinger, B., Copper oxide-based model of persistent free radical formation on combustion-derived particulate matter. *Environmental Science & Technology* **2008,** 42, (13), 4982-4988.

11.	Grosvenor, A. P.; Biesinger, M. C.; Smart, R. S.; McIntyre, N. S., New interpretations of XPS spectra of nickel metal and oxides. *Surf Sci* **2006,** 600, (9), 1771-1779.

12.	Amama, P. B.; Maschmann, M. R.; Fisher, T. S.; Sands, T. D., Dendrimer-templated Fe nanoparticles for the growth of single-wall carbon nanotubes by plasma-enhanced CVD. *Journal of Physical Chemistry B* **2006,** 110, (22), 10636-10644.

13.	Choi, H. C.; Kim, W.; Wang, D. W.; Dai, H. J., Delivery of catalytic metal species onto surfaces with dendrimer carriers for the synthesis of carbon nanotubes with narrow diameter distribution. *Journal of Physical Chemistry B* **2002,** 106, (48), 12361-12365.

14.	Bosman, A. W.; Schenning, A. P. H. J.; Janssen, R. A. J.; Meijer, E. W., Well-defined metallodendrimers by site-specific complexation. *Chem Ber-Recl* **1997,** 130, (6), 725-728.

15.	Floriano, P. N.; Noble, C. O.; Schoonmaker, J. M.; Poliakoff, E. D.; McCarley, R. L., Cu(0) nanoclusters derived from poly(propylene imine) dendrimer complexes of CU(II). *Journal of the American Chemical Society* **2001,** 123, (43), 10545-10553.

16.	Vanderah, T. A., *Chemistry of superconducting materials. Preparation, Chemistry, Characterization and Theory*. Noyes Publications: Park Ridge, New jersey, USA, 1992.

17.	Crooks, R. M.; Zhao, M. Q.; Sun, L.; Chechik, V.; Yeung, L. K., Dendrimer-encapsulated metal nanoparticles: Synthesis, characterization, and applications to catalysis. *Accounts of Chemical Research* **2001,** 34, (3), 181-190.

18.   Esumi, K.; Goino, M., Adsorption of poly(amidoamine) dendrimers on aluminan-water and silica/water interfaces. *Langmuir* **1998,** 14, (16), 4466-4470.

19.   Sun, L.; Crooks, R. M., Dendrimer-Mediated Immobilization of Catalytic Nanoparticles on Flat, Solid Supports. *Langmuir* **2002,** 18, 8231-8236.

20.   Ebert, M. Non-thrombogenic prosthetic material. 3914802, 1975.

21.   Hierlemann, A.; Campbell, J. K.; Baker, L. A.; Crooks, R. M.; Ricco, A. J., Structural distortion of dendrimers on gold surfaces: A tapping-mode AFM investigation. *Journal of the American Chemical Society* **1998,** 120, (21), 5323-5324.

22.   Velarde-Ortiz, R.; Larsen, G., A poly(propylene imine) (DAP-Am-64) dendrimer as Cu2+ chelator for the synthesis of copper oxide clusters embedded in sol-gel derived matrixes. *Chemistry of Materials* **2002,** 14, (2), 858-866.

23.   Datye, A. K.; Xu, Q.; Kharas, K. C.; McCarty, J. M., Particle size distributions in heterogeneous catalysts: What do they tell us about the sintering mechanism? *Catalysis Today* **2006,** 111, (1-2), 59-67.

24.   Zaera, F., The surface chemistry of hydrocarbons on transition metal surfaces: A critical review. *Israel Journal of Chemistry* **1998,** 38, (4), 293-311.

25.   Khaleel, A.; Al-Nayli, A., Supported and mixed oxide catalysts based on iron and titanium for the oxidative decomposition of chlorobenzene. *Applied Catalysis B-Environmental* **2008,** 80, (1-2), 176-184.

26.   Evans, C. S.; Dellinger, B., Surface-mediated formation of polybrominated dibenzo-p-dioxins and dibenzofurans from the high-temperature pyrolysis of 2-bromophenol on a CuO/silica surface. *Environmental Science & Technology* **2005,** 39, (13), 4857-4863.

27.   Alderman, S. L.; Farquar, G. R.; Poliakoff, E. D.; Dellinger, B., An infrared and X-ray spectroscopic study of the reactions of 2-chlorophenol, 1,2-dichlorobenzene, and chlorobenzene with model CuO/silica fly ash surfaces. *Environmental Science & Technology* **2005,** 39, (19), 7396-7401.

28.   Reshetnikov, S. I.; Lukashevich, A. I.; Alikina, G. M.; Sadykov, V. A., Effect of oxygen mobility in solid catalyst on transient regimes of catalytic reaction of methane partial oxidation at short contact times. *Catalysis Letters* **2006,** 110, (3-4), 235-242.

29.   Keulks, G. W., Mechanism of Oxygen Atom Incorporation into Products of Propylene Oxidation over Bismuth Molybdate. *Journal of Catalysis* **1970,** 19, (2), 232-&.

30.   Nganai, S.; Lomnicki, S.; Dellinger, B., Ferric Oxide Mediated Formation of PCDD/Fs from 2-Monochlorophenol. *Environmental Science & Technology* **2009,** 43, (2), 368-373.

31.   Ihm, H.; White, J. M., Stepwise dissociation of thermally activated phenol on Pt(111). *Journal of Physical Chemistry B* **2000,** 104, (26), 6202-6211.

32.   Lomnicki, S.; Dellinger, B., A detailed mechanism of the surface-mediated formation of PCDD/F from the oxidation of 2-chlorophenol on a CuO/silica surface. *J Phys Chem A* **2003,** 107, (22), 4387-4395.

33.   Takasuga, T.; Makino, T.; Tsubota, K.; Takeda, N., Formation of dioxins (PCDDs/PCDFs) by dioxin-free fly ash as a catalyst and relation with several chlorine-sources. *Chemosphere* **2000,** 40, (9-11), 1003-1007.

34.   Bond, G. C.; Slaa, J. C., The origin of particle size effects in supported metal catalysts: Propane hydrogenolysis on Ru/Al2O3 catalysts. *Journal of Chemical Technology and Biotechnology* **1996,** 65, (1), 15-20.

35.   Makino, T.; Matsumoto, K.; Ebara, T.; Mine, T.; Ohtsuka, T.; Mizuguchi, J., Complete decomposition of benzene, toluene, and particulate matter contained in the exhaust of diesel engines by means of thermally excited holes in titanium dioxide at high temperatures. *Japanese Journal of Applied Physics Part 1-Regular Papers Brief Communications & Review Papers* **2007,** 46, (9A), 6037-6042.

36.   Stieglitz, L.; Vogg, H.; Zwick, G.; Beck, J.; Bautz, H., On Formation Conditions of Organohalogen Compounds from Particulate Carbon of Fly-Ash. *Chemosphere* **1991,** 23, (8-10), 1255-1264.

37.   Bockhorn, H., *Soot Formation in Combustion: Mechanisms and Models*. Springer-Verlag: Berlin, 1994.

38.   Richter, H.; Howard, J. B., Formation of polycyclic aromatic hydrocarbons and their growth to soot - a review of chemical reaction pathways. *Progress in Energy and Combustion Science* **2000,** 26, (4-6), 565-608.

39.   Leavittt, A. J.; Wyrwas, R. B.; Wallace, W. T.; Serrano, D. S.; Arredondo, M. G.; Leslie, L. M.; Khan, F. A.; Whetten, R. L., Efficient low-temperature oxidation of carbon-cluster anions by SO2. *J Phys Chem A* **2005,** 109, (28), 6218-6222.

40.   Allouis, C.; Beretta, F.; D'Alessio, A., Structure of inorganic and carbonaceous particles emitted from heavy oil combustion. *Chemosphere* **2003,** 51, (10), 1091-1096.

41.   Tesner, P. A.; Shurupov, S. V., Soot formation during pyrolysis of naphthalene, anthracene and pyrene. *Combustion Science and Technology* **1997,** 126, (1-6), 139-151.

42.   Wong, C., Characterization of Metal Soot Systems by Transmission Electron-Microscopy. *Carbon* **1988,** 26, (5), 723-734.

CHAPTER V: SUMMARY

5.1   The Role of Dendrimer in the Synthesis of Metal Oxide Catalysts

The addition of dendrimer in the synthesis of metal oxide catalysts had a significant effect in stabilizing and controlling the size of metal oxide clusters on substrate surface. This dendrimer-assisted synthetic route is based on the unique characteristic of dendrimer which can stoichiometrically complex with metal ions in aqueous solvent and be stabilized on various substrate surface, e.g. silica, titanium oxide. To reduce the potential interference of dendrimer on the catalytic activity of metal oxide nanoclusters, it is critical to setup the optimized thermal condition to get rid of the dendrimeric body while retaining the nanoclusters immobilized on surface. It had been shown that the carbonaceous backbone of dendrimer could be completely removed at furnace temperature of 450°C in air. Though very small agglomeration of metal oxide nanoclusters was observed, the clusters size was still very uniform in the scale from 1-3 nm. XANES and XPS data indicated that the metal nanoclusters are in transition metal oxide compound. HR-TEM was employed as a direct imaging technique to obtain the size and size distribution. By changing the amount of metal ions complexed by the dendrimer, the size of metal oxide nanoclusters deposited on surface can be selectively controlled with narrow size distribution. The loading of metal on the surface of supporting matrix also affect the size of metal oxide nanoclusters. The less metal present on surface, the smaller the clusters will be because of less agglomeration. To enhance the adsorption of precursor to the surface of substrate, a 24 hr "pre-adsorption" process was introduced prior to the deposition of dendrimer-metal complex on silica. This procedure resulted in a significant, 22%~38% decrease of the size of nanoclusters. Increasing the furnace temperature resulted in the "growth" of clusters size statistically. However, while most of the particles remained in the 2-4nm domain, the shape of

the size distribution became boarder and positively skewed due to the particle migration and coalescence mechanism of growth.

Though copper/silica matrix was most intensively studied in this experimental work, we have demonstrated this dendrimer based technique can be universally applied to other metals (nickel, iron) and substrate materials (titanium oxide). we anticipate that our procedure for the size controlled synthesis of supported metal oxide nanoclusters can also be readily extended to other metal (such as Co, Cd, Ag) and other supporting materials (such as magnesia or alumina).

Table 5.1 lists the available sizes of CuO/Silica nanoclusters which had been synthesized. Based on our works, application of the dendrimer-assisted deposition of metal oxide on silica appears to be a powerful tool for the precise control of the size of synthesized nanoclusters. This method can be further expanded by application of different generation of dendrimers to further tune the size of nanoclusters.

Table 5.1 Available sizes of copper oxide clusters supported on silica using the dendrimer-assited method described in this chapter

Precursor	Temp. (°C)	Pre-adsorption	Dia. (nm)	Std. Deviation (nm)
5 wt.% G4Cu(II)$_{16}$/silica	650	YES	**5.64**	2.52
5 wt.% G4Cu(II)$_{16}$/silica	600	YES	**4.09**	1.59
5 wt.% G4Cu(II)$_{16}$/silica	450	NO	**3.27**	0.24
5 wt.% G4Cu(II)$_{16}$/silica	550	YES	**3.17**	0.71
2 wt.% G4Cu(II)$_{16}$/silica	450	NO	**2.60**	0.34
1 wt.% G4Cu(II)$_{16}$/silica	450	NO	**2.40**	0.31
5 wt.% G4Cu(II)$_{8}$/silica	450	NO	**2.37**	0.34
1 wt.% G4Cu(II)$_{16}$/silica	600	YES	**2.09**	0.76
5 wt.% G4Cu(II)$_{16}$/silica	450	YES	**2.05**	0.23
5 wt.% G4Cu(II)$_{8}$/silica	450	YES	**1.86**	0.17
1 wt.% G4Cu(II)$_{16}$/silica	550	YES	**1.84**	0.55
2 wt.% G4Cu(II)$_{16}$/silica	450	YES	**1.76**	0.25
5 wt.% G4Cu(II)$_{4}$/silica	450	NO	**1.68**	0.19
1 wt.% G4Cu(II)$_{16}$/silica	450	YES	**1.55**	0.19
5 wt.% G4Cu(II)$_{4}$/silica	450	YES	**< 1**	NA

5.2　The Effect of Particle Size in Catalysis

Transition metal oxide was proven to promote the decomposition of chlorinated hydrocarbon through the surface-mediated reactions.[1-2]　However, less studies has focused on the effect of metal oxide cluster sizes in these reactions, mostly due to the lack of capability to produce monodispersed nanoclusters with desired diameter on certain substrates, e.g. silica, titanium oxide in amorphous form.　For catalysis, it has been widely accepted that when the metal oxide cluster size falls into the range < 10 nm, their activity in catalytic reactions becomes nonlinear and the formation of by-products may be selective.[3]　In this study, metal oxide particles supported on silica (Cab-O-Sil) were used for the catalyzed thermal degradation of chlorinated benzenes.　To determine the size effect of metal oxide particles in these reactions, catalysts were prepared in two different methods: dendrimer-template route and incipient wetness impregnation method.　The first method was used to produce nano-size clusters according to the results obtained from project of size-controlled synthesis of metal oxide nanoparticles.　The second method was used to produce surrogate of coarse particles which indeed had particles size varying from several to several hundred nanometers, as indicated by both TEM and XRD results.　To study the catalytic performance of metal oxide in the combustion-generated pollutants formation, copper and iron were selected as the studied metals due to their abundance in combustion-generated fly ash.[4]　1,2-Dichlorobenzene (o-DCBz) and monochlorobenzene (MCBz) were used as the model compounds for catalysis test as chlorinated benzenes represent a large group of chlorinated volatile organic compounds which has been identified toxic pollutants.[5-6]

In all catalysis experiments, nano-size metal oxide samples exhibited superior activity in the overall conversion of chlorinated benzenes.　Catalytic destruction of chlorinated benzenes was initiated by their chemisorption onto metal oxide surface with the elimination of hydrogen

chloride and formation of surface bound phenolate and bidentate.[6] For the same mass loading, nano-size catalysts contained more metal oxide sites exposed on surface for these chemisorption and subsequent reactions. As benzene and chlorobenzene are the direct desorption products of chemisorbed species, their higher yield on nano-size catalyst corresponded to the higher surface area. In the decomposition reaction of o-DCBz, the size effect of metal oxide nanoclusters on the chlorobenzene yield was not as significant as they were on the benzene yield. One of the probable explanations for this phenomenon is the superior chlorination capability of larger metal oxide particles, which increased the chlorobenzene yield and decrease the competitive benzene yield. The higher yield of polychlorinated benzene over coarse metal oxide catalyst also supported this hypothesis. In comparison of copper and iron effect on products formation, the stronger oxidative properties of iron cause more chlorinated species formation under pyrolytic condition and more complete destruction of o-DCBz under oxidative condition. For the MCBz reaction over the iron oxide catalyst, the most dominant products was benzene, which was yielded maximally to 44% at 500 °C and 14% at 550 °C for nano-size and coarse catalysts, respectively. The extraordinary selectivity of benzene formation over nano-size iron oxide catalysts suggests their potential application in the dechlorination treatment of chlorinated benzenes.

Phenols products formed under pyrolytic condition, including phenol, benzofuran, and dibenzofuran, all show higher maximum yields at equal or lower temperature from the reaction over nano-size catalysts than their coarse analogues. These results can be correlated to the relatively easier access of surface-bound oxygen of smaller clusters which can be readily regenerated by the diffusion of oxygen from internal layers to particles surface.

The decomposition products of chlorinated benzenes under oxidative condition are dominated by chlorinated ethylenes and chlorinated benzenes. Ethylene has been widely

recognized as one of the soot precursors in combustion system.[7-8] Furthermore, it was reported that the addition of chlorinated organic species into combustion enhanced soot formation.[9-10] Therefore, the higher yield of chlorinated ethylenes over nano-size copper oxide (G4Cu$_n$) catalysts indicates that small metal oxide nanoparticles may promote the formation of soot-like carbonaceous materials. This assumption was reinforced by the TEM results shown in **Figure 5.1**. The carbon like deposit indicates the reaction of o-DCBz over G4Cu$_n$ has resulted solid form carbonaceous materials.
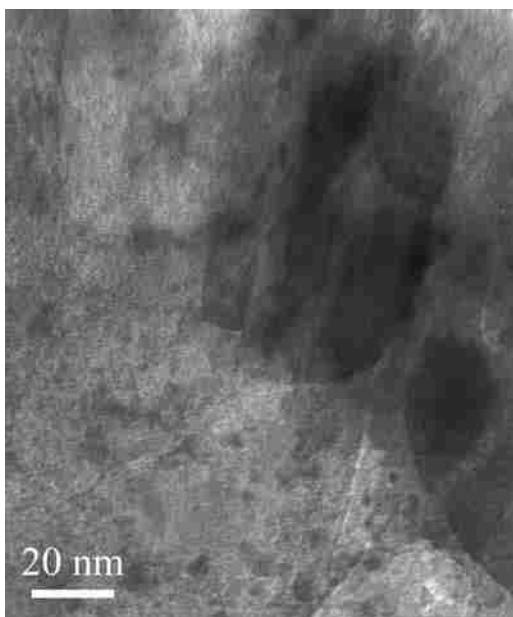
Figure 5.1 TEM micrographs of G4Cu$_{16}$ catalyst collected after reaction with 1,2-dichlorobenzene under oxidative condition at 400 ℃. The small black spot is the copper oxide nanoclusters and the larger black area is the carbonaceous deposits formed during the thermal process. Some clusters became larger due to the high temperature reaction and diffusion caused by passing gas.

5.3 The Impact of Metal Oxide Nanoparticles on Soot Formation

Although the effects of metal additives on soot formation have been studied in many practical and laboratory-scale combustion systems, there is no reported research work regarding the roles of already-formed metal/metal oxide nanoparticles in combustion. In contrast, most studies used the fuel premixed with metal additives in which the formation of metal oxide nanoparticles and carbonaceous material may occur at the same time.[8, 11-13] Though it has been proposed that the cation nucleus may also be the condensation centers for soot formation in

combustion, it is impossible to have direct observation to determine the effect of metal oxide nanoparticles on soot formation using fuel premixed with metal additive.

In this study, we investigated the influence of metal oxide as nucleation mode seed on the formation of soot-like carbonaceous particulate matters under isothermal conditions. This strategy involved the generation of gas-suspended metal oxide nanoparticles and their interaction with gaseous hydrocarbon under parametrically controlled high temperature condition. The most desirable approach to test this hypothesis is to conduct a non-metal combustion as the blank reference using same experimental condition. However, it is difficult to remove metal compounds completely in many combustors using ordinary methods. Furthermore, flames have limited reaction conditions that could make it difficult to quantitate the impact of metal nanoparticles. To avoid these uncertainties, a high temperature flow quartz reactor was built to use for isothermal flameless combustion, with or without the addition of metal species.

Methanolic solution of dendrimer-metal complex was chosen as the precursor of metal oxide nanoparticles because dendrimer can host various kinds of metal ions stoichiometrically and lead to the formation of monodispersed nanoparticles with dendrimer burned-off. Under oxygen rich condition, the organic portion (dendrimer, methanol solvent) of the precursor can be removed efficiently at 700 °C, leaving the formation of 1-3 nm metal oxide nanoparticles as the only condensed particulate matter which is immediately transferred to the combustion chamber by carrier gas. By increasing the furnace temperature to 900 °C, larger crystalline metal oxide nanoparticles with size up to 80 nm were observed.

The formation of soot was identified by their pseudo onion like structure shown on TEM micrographs. Experimental results indicate the addition of metal oxide nanoparticles into combustion process increased the yield of soot as well as high molecular weight PAH under fuel rich condition. Temperature is a critical factor affects the soot formation. The higher the

temperature (> 1100 °C) was, the more soot was produced and the less PAH was formed. But there was no soot particles formed under 1000 °C. Fuel/Air ratio is another key parameter determined the formation of soot. Though in all experiments soot was observed only under fuel rich (C/O > 1) condition, the addition of metal oxide nanoparticles initialize the formation of soot started by a lower C/O values 2.0, compared to 2.5 for non-metal combustion, as indicated by TEM micrographs.

5.4   References

1.   Nganai, S.; Lomnicki, S.; Dellinger, B., Ferric Oxide Mediated Formation of PCDD/Fs from 2-Monochlorophenol. *Environmental Science & Technology* **2009,** 43, (2), 368-373.

2.   Moon, S. W.; Lee, G. D.; Park, S. S.; Hong, S. S., Catalytic combustion of chlorobenzene over supported metal oxide catalysts. *J Ind Eng Chem* **2004,** 10, (4), 661-666.

3.   Aiken, J. D.; Finke, R. G., A review of modern transition-metal nanoclusters: their synthesis, characterization, and applications in catalysis. *Journal of Molecular Catalysis a-Chemical* **1999,** 145, (1-2), 1-44.

4.   Stieglitz, L.; Vogg, H.; Zwick, G.; Beck, J.; Bautz, H., On Formation Conditions of Organohalogen Compounds from Particulate Carbon of Fly-Ash. *Chemosphere* **1991,** 23, (8-10), 1255-1264.

5.   Kasai, E.; Kobayashi, T.; Nakamura, T., Formation of PCDD/Fs on iron oxides from chlorobenzene and chlorophenol. *Organohalogen Compd. FIELD Full Journal Title:Organohalogen Compounds* **1999,** 41, 187-190.

6.   Alderman, S. L.; Farquar, G. R.; Poliakoff, E. D.; Dellinger, B., An infrared and X-ray spectroscopic study of the reactions of 2-chlorophenol, 1,2-dichlorobenzene, and chlorobenzene with model CuO/silica fly ash surfaces. *Environmental Science & Technology* **2005,** 39, (19), 7396-7401.

7.   Commodo, M.; Violi, S.; D'Anna, A.; D'Alessio, A.; Allouis, C.; Beretta, F.; Minutolo, P., Soot and nanoparticle formation in laminar and turbulent flames. *Combustion Science and Technology* **2007,** 179, (1-2), 387-400.

8.   Hirasawa, T.; Sung, C. J.; Yang, Z. W.; Joshi, A.; Wang, H., Effect of ferrocene addition on sooting limits in laminar premixed ethylene-oxygen-argon flames. *Combust Flame* **2004,** 139, (4), 288-299.

9.   Mckinnon, J. T.; Howard, J. B., Application of Soot Formation Model - Effects of Chlorine. *Combustion Science and Technology* **1990,** 74, (1-6), 175-197.

10.   Leylegian, J. C., Soot formation in aerodynamically strained methane-air and ethylene-air diffusion flames with chloromethane addition. *Combust Flame* **2008,** 152, (1-2), 144-153.

11.   Feitelberg, A. S. The effects of metal additives on soot formation. Massachusetts Institute of Technology, 1990.

12.   Kasper, M.; Sattler, K.; Siegmann, K.; Matter, U.; Siegmann, H. C., The influence of fuel additives on the formation of carbon during combustion. *J Aerosol Sci* **1999,** 30, (2), 217-225.

13.   Jung, H.; Kittelson, D.; Zachariah, M. R. In *The Influence of Metal Additives on Diesel Exhaust Particles: Size Distribution, Morphology, Charge and Kinetics of Oxidation*, WSS/Ci Davis, CA 2004; Davis, CA 2004.

APPENDIX 1. HR-TEM IMAGES AND SIZE DISTRIBUTION OF NICKEL AND IRON OXIDE NANOCLUSTERS

A: Nickel Oxide Nanoparticles Obtained from Calcinated (450 ºC) Silica Impregnated with DAB-Am32-Ni(II)$_n$ (n=16, 8, 4) Complexes

n=16

n=8

n=4

143
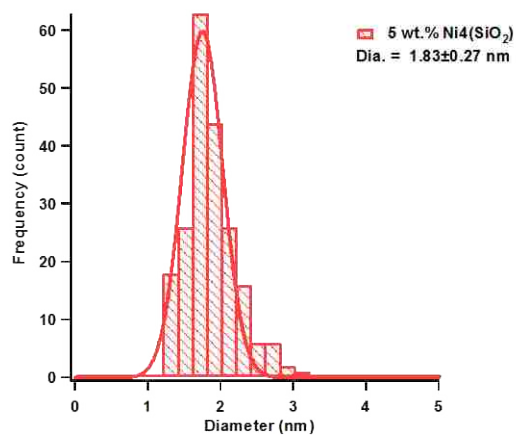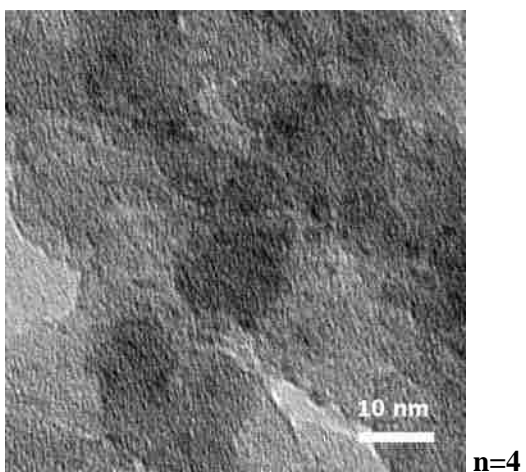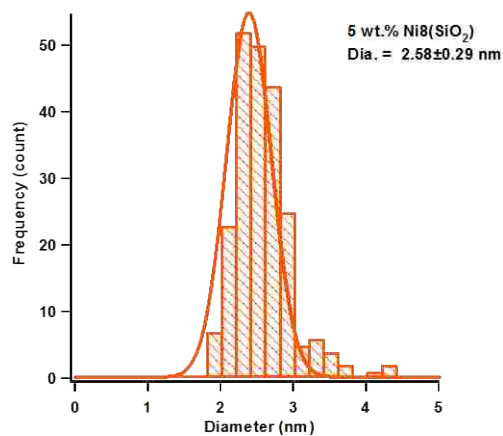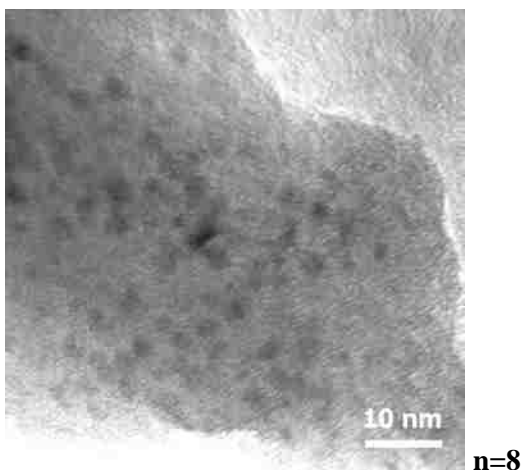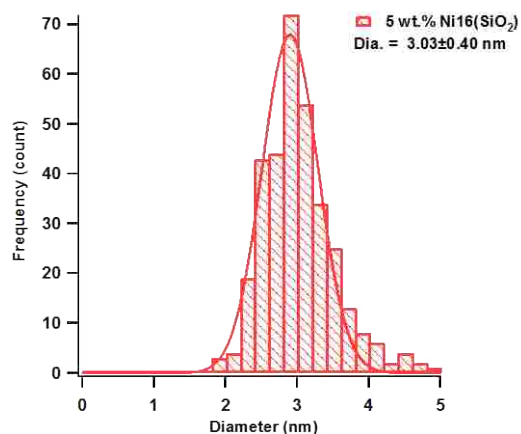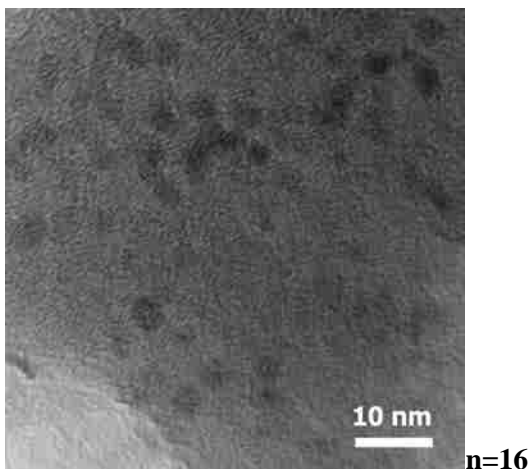
B: Iron Oxide Nanoparticles Obtained from Calcinated (450 ºC) Silica Impregnated with DAB-Am32-Fe(II)$_n$ (n=16, 11, 8, 4) Complexes

n=16

n=11

n=8
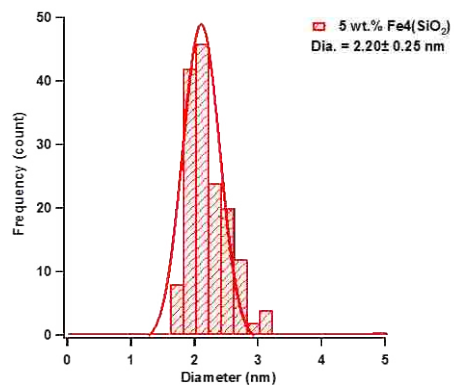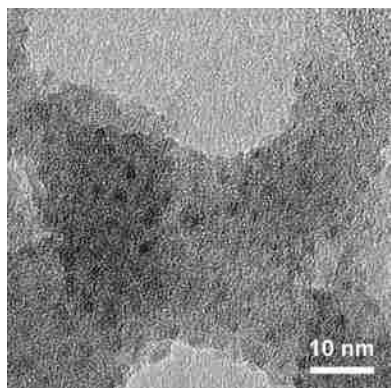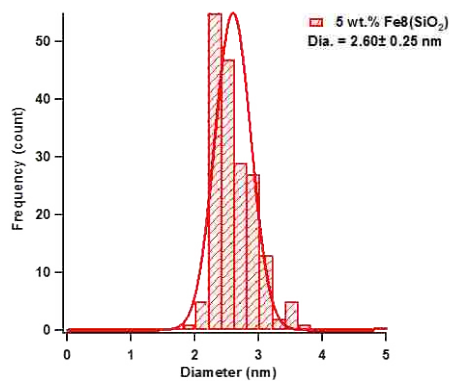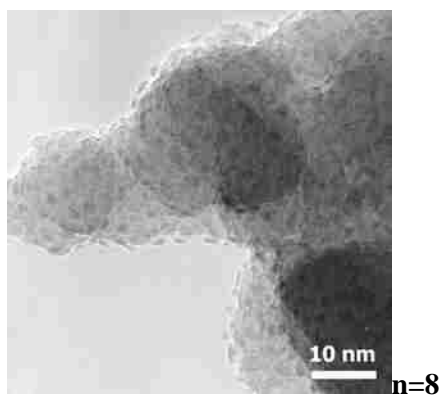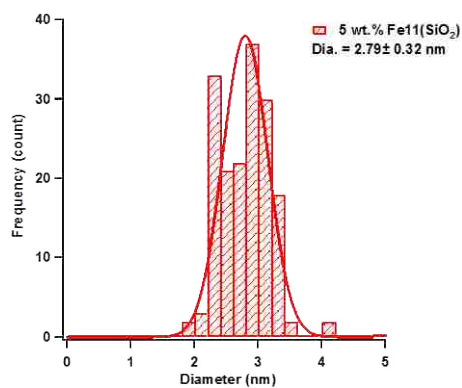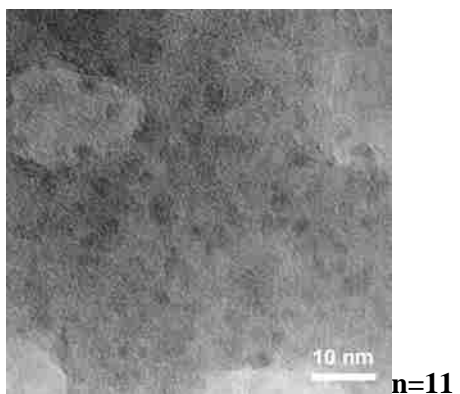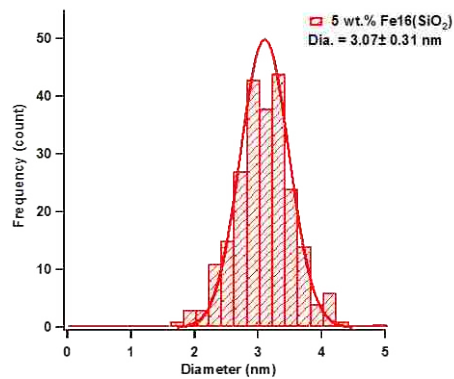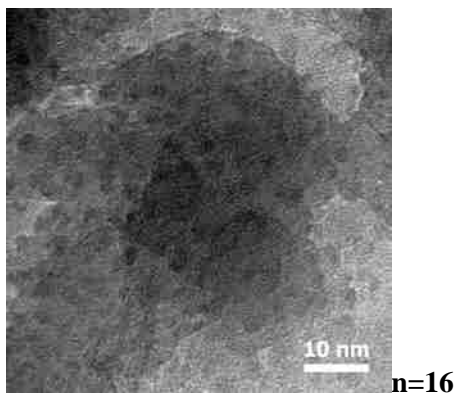
C: Thermally Treated (450 ºC) DAB-Am32-Ni(II)$_{16}$ with
Various NiO Loading (1~5 wt.%) on Cab-O-Sil® Silica

5 wt.%

5 wt.% Ni16(SiO$_2$)
Dia. = 3.03±0.40 nm

2 wt.%

2 wt.% Ni16(SiO$_2$)
Dia. = 2.47±0.39 nm

1 wt.%

1 wt.% Ni16(SiO$_2$)
Dia. = 2.35±0.25 nm
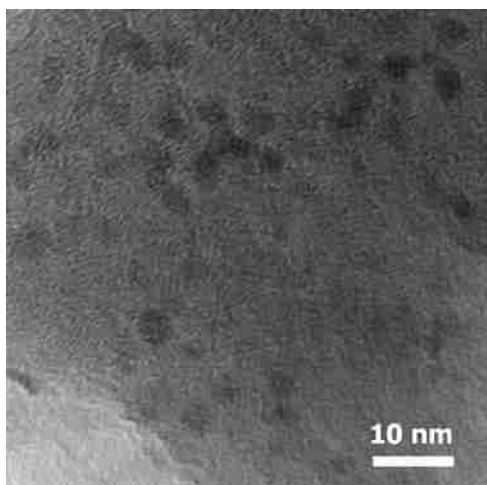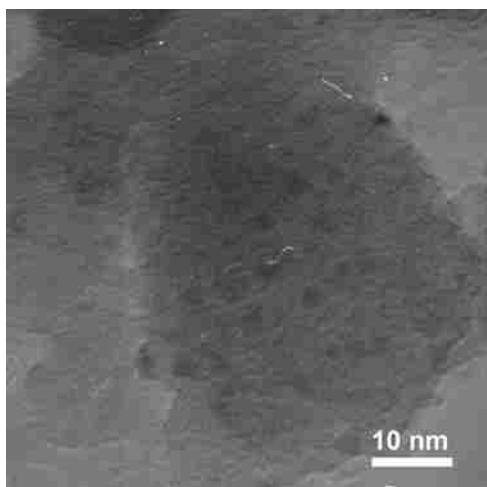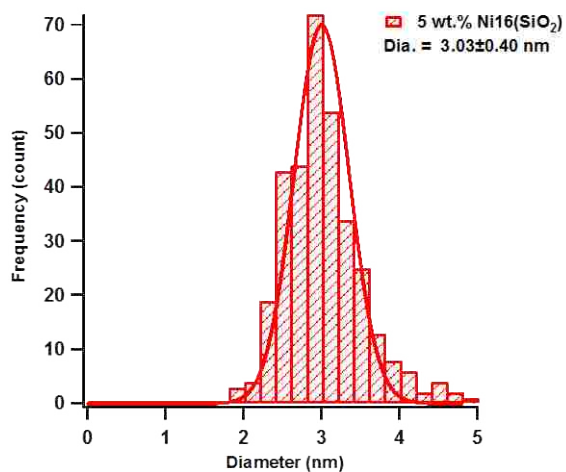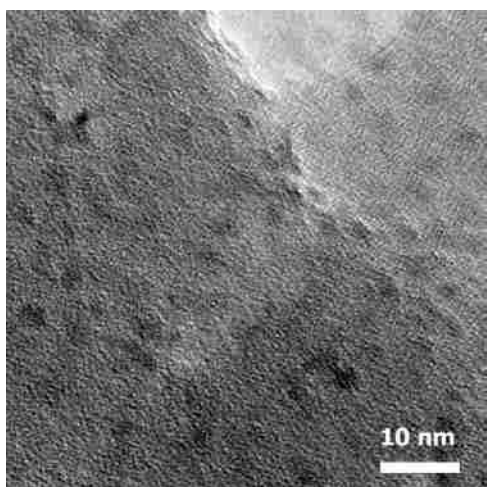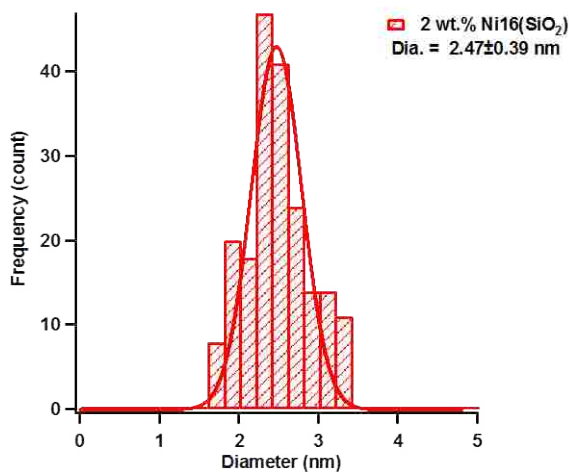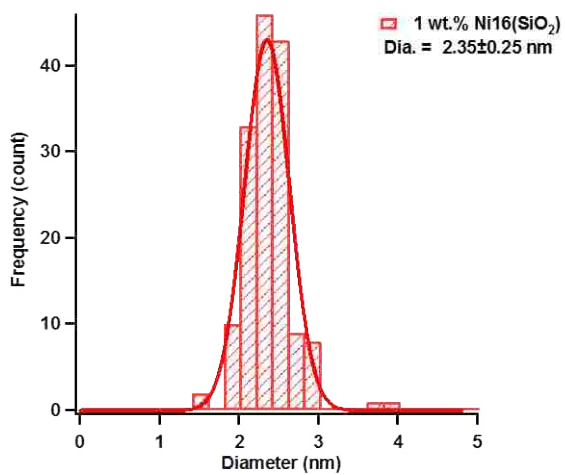
D: Size distribution of CuO Nanoparticles Obtained from High Temperature (550 to 650ºC), Calcinated DAB-Am32-Cu(II)$_{16}$ on Cab-O-Sil® Silica
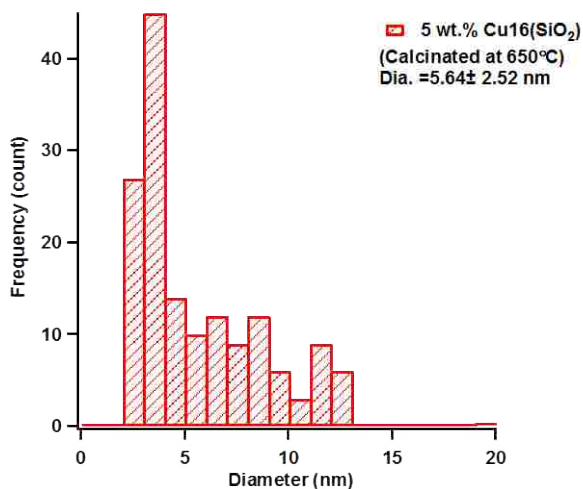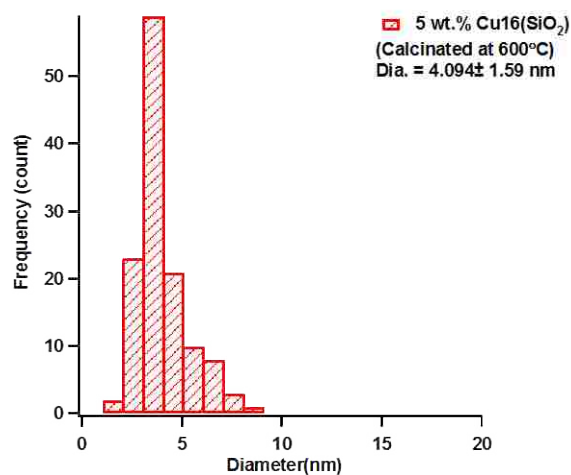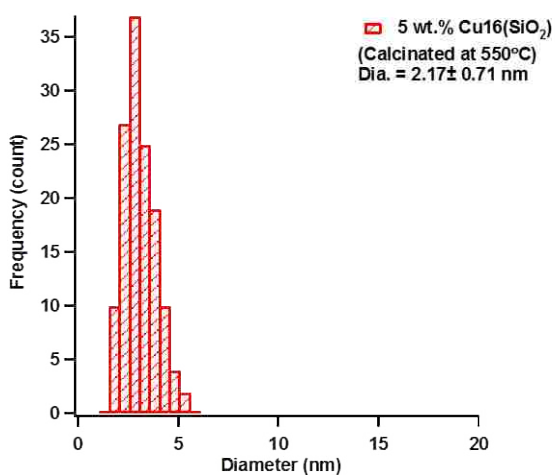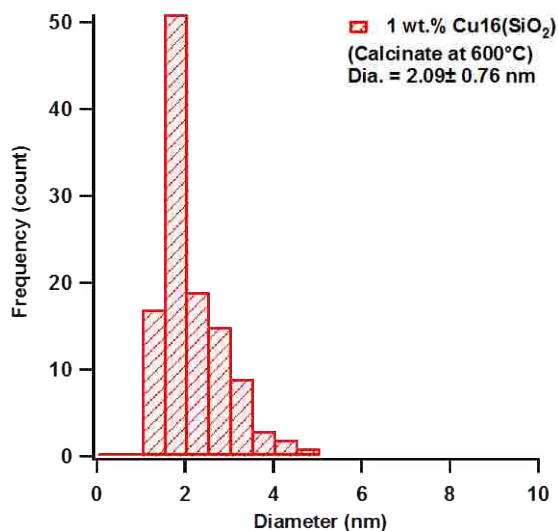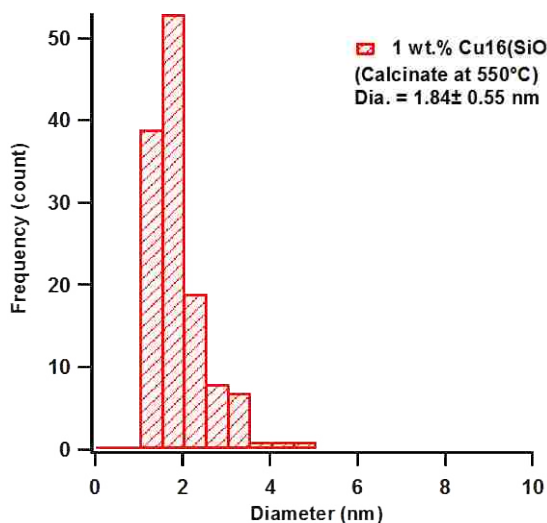
# APPENDIX 2. PRODUCTS YIELDS OF CHLORINATED BENZENES REACTION OVER METAL OXIDE CATALYSTS

A: Products Yield of 1,2-Dichlorobenzene over CuO/silica under Pyrolytic Condition
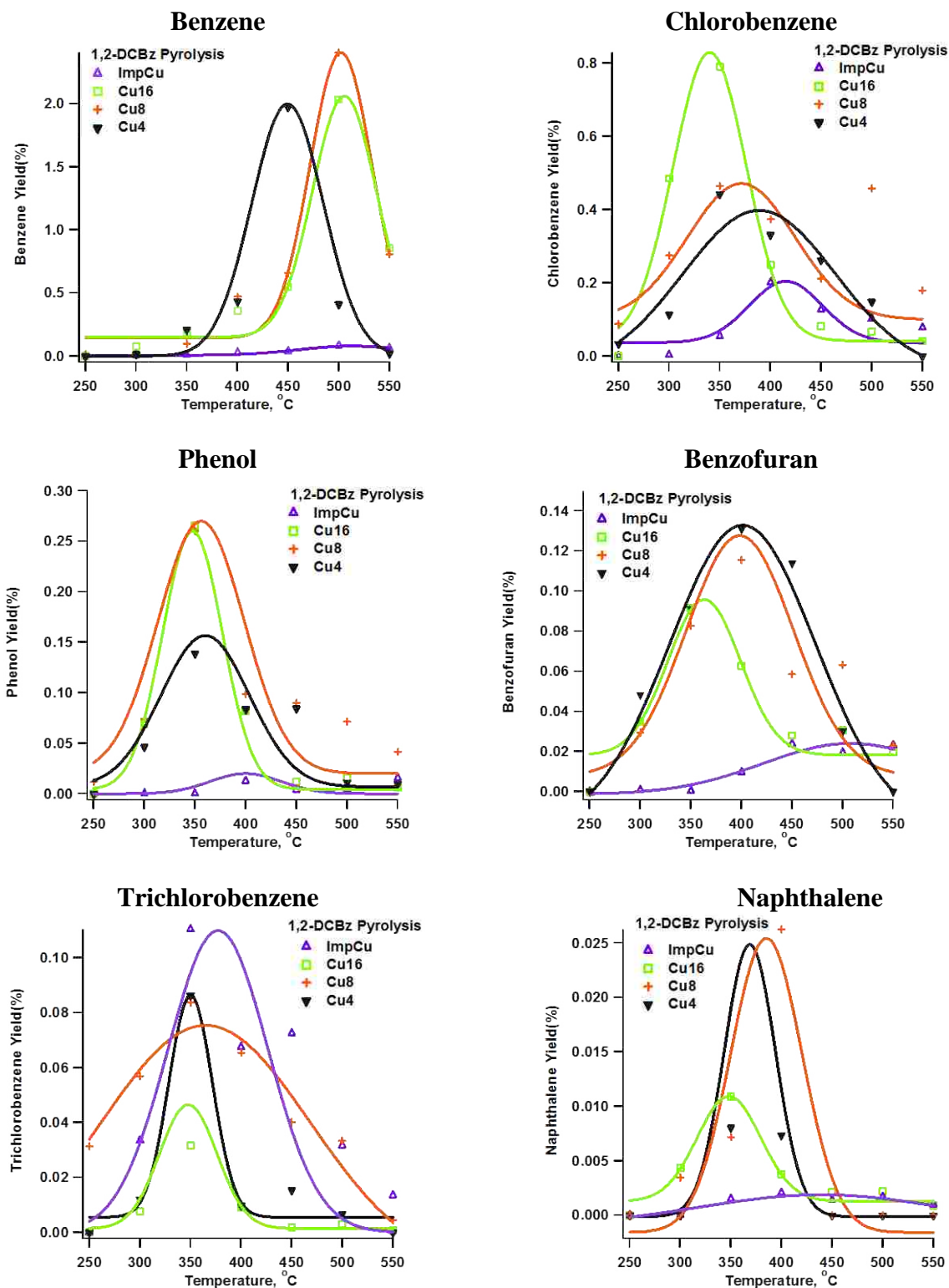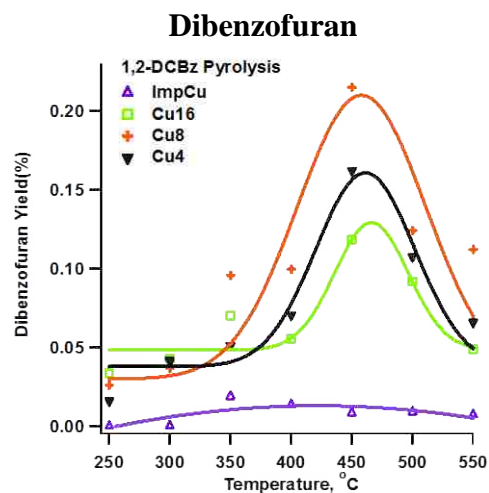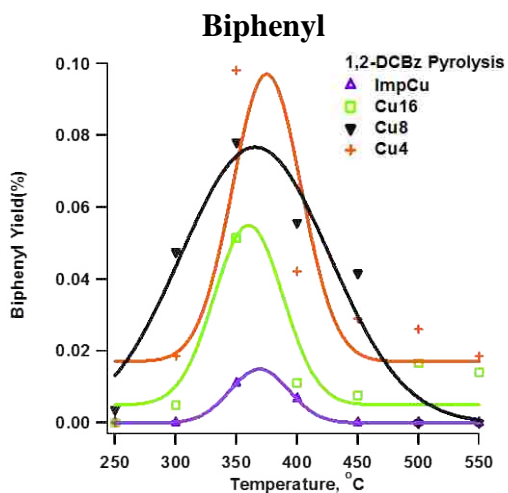
147

Biphenyl

Dibenzofuran

B: Products Yield of 1,2-Dihlorobenzene over CuO/silica under Oxidative Condition

Trichloroethylene

Tetrachlorobenzen

Trichlorobenzene

Tetrachlorobenzene

Pentachlorobenzene

Hexachlorobenzene

C: Products Yield of 1,2-Dihlorobenzene over Fe_2O_3/silica under Pyrolytic Condition
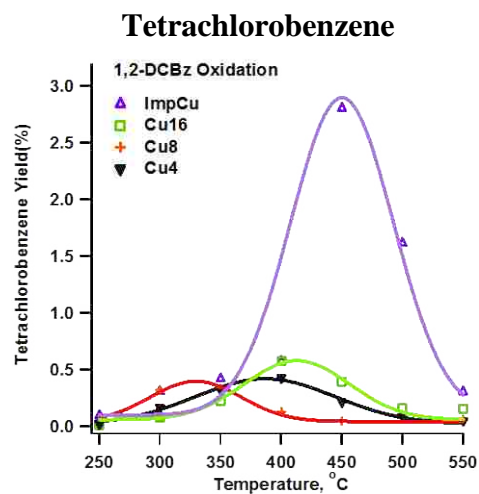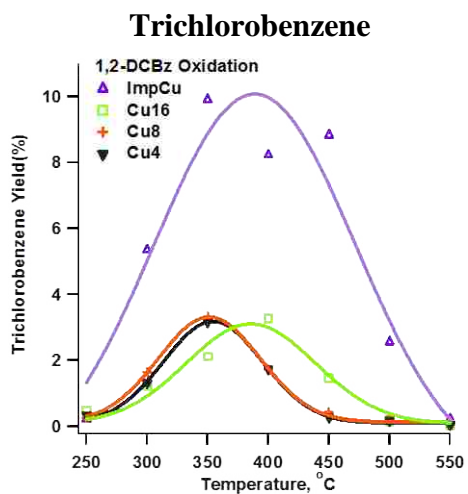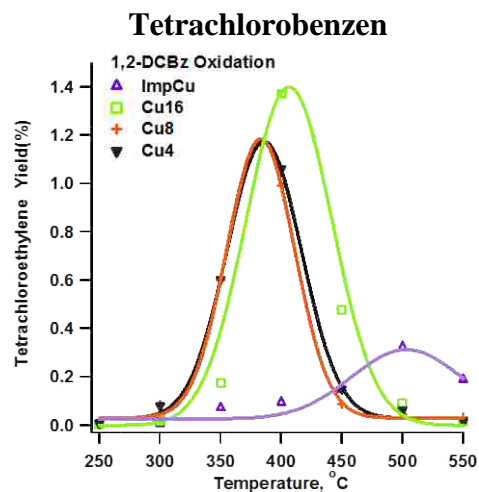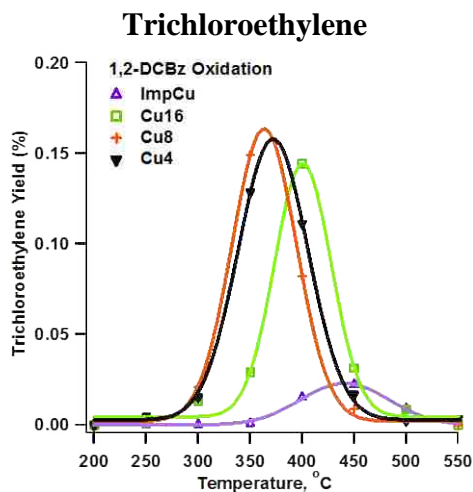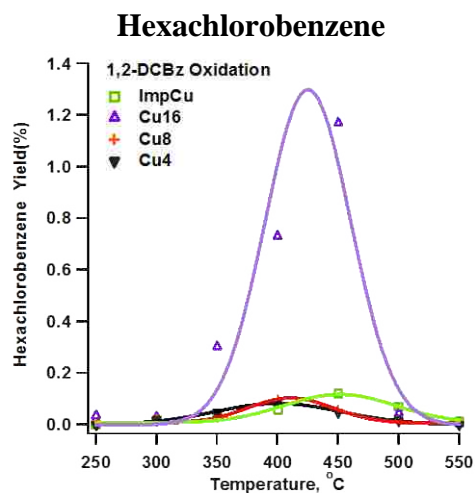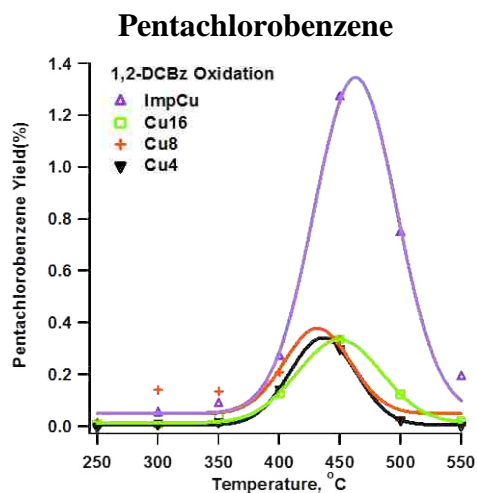
Benzene

Chlorobenzene
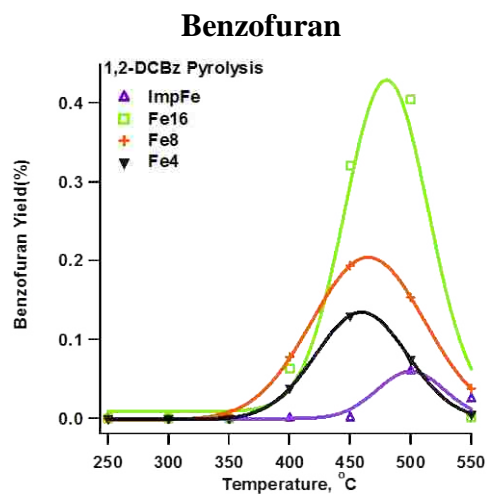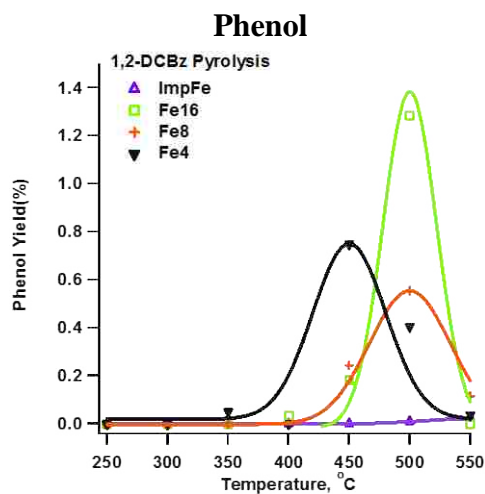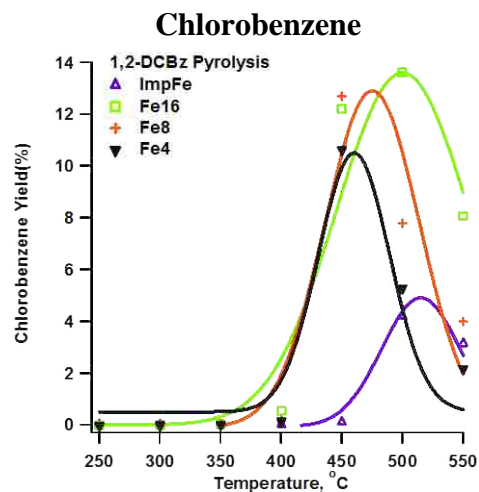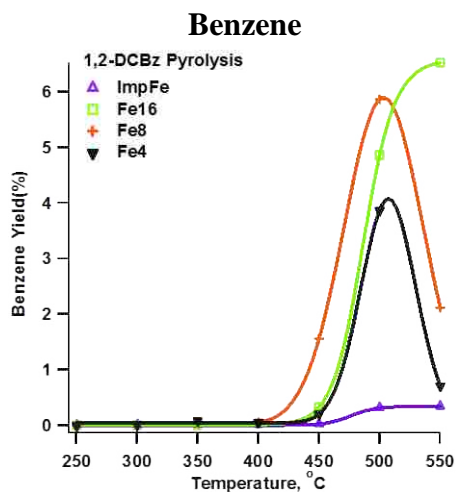
Phenol

Benzofuran

2-Monochlorophenol
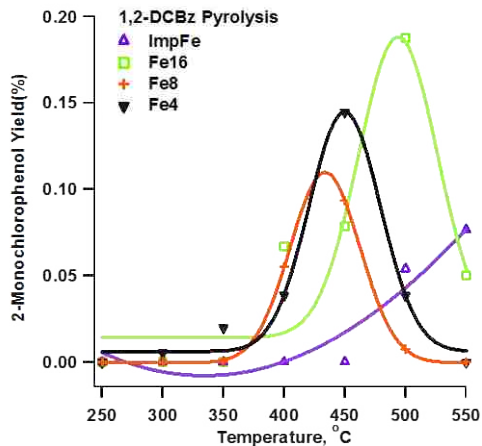
Dichlorophenol
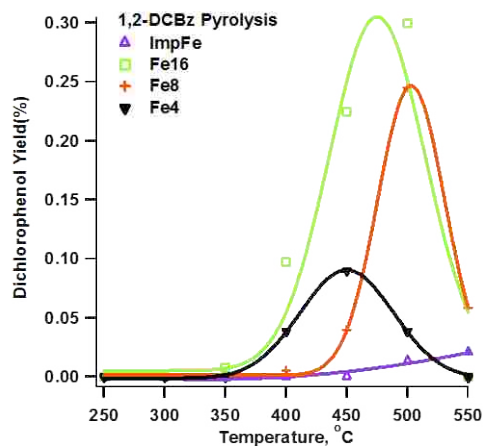
Trichlorobenzene
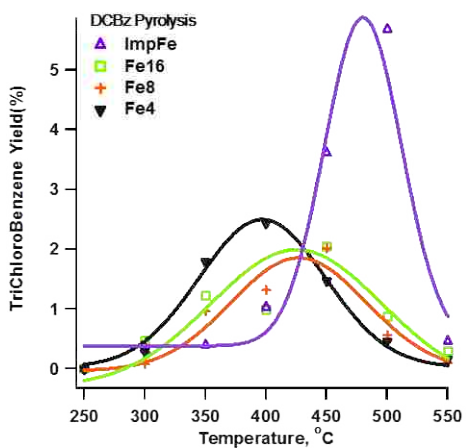
Tetrachlorobenzene

Dibenzofuran

150
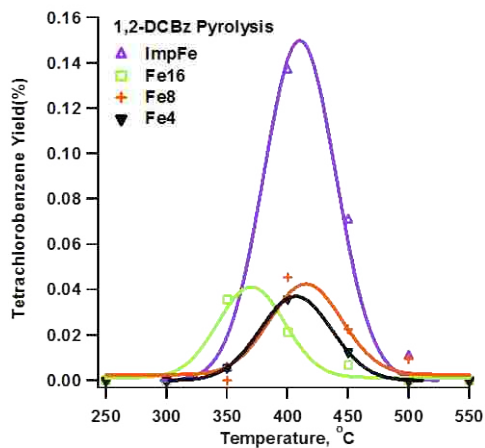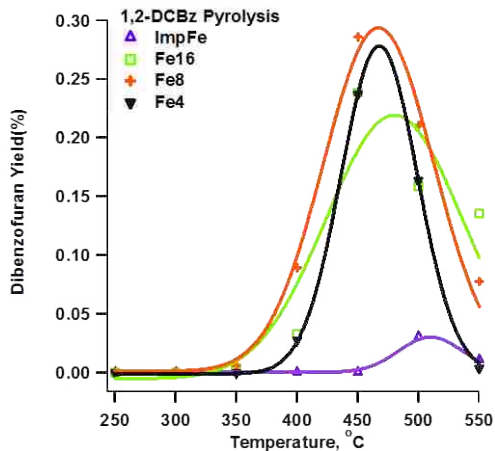
D: Products Yield of 1,2-Dichlorobenzene over Fe$_2$O$_3$/silica under Oxidative Condition
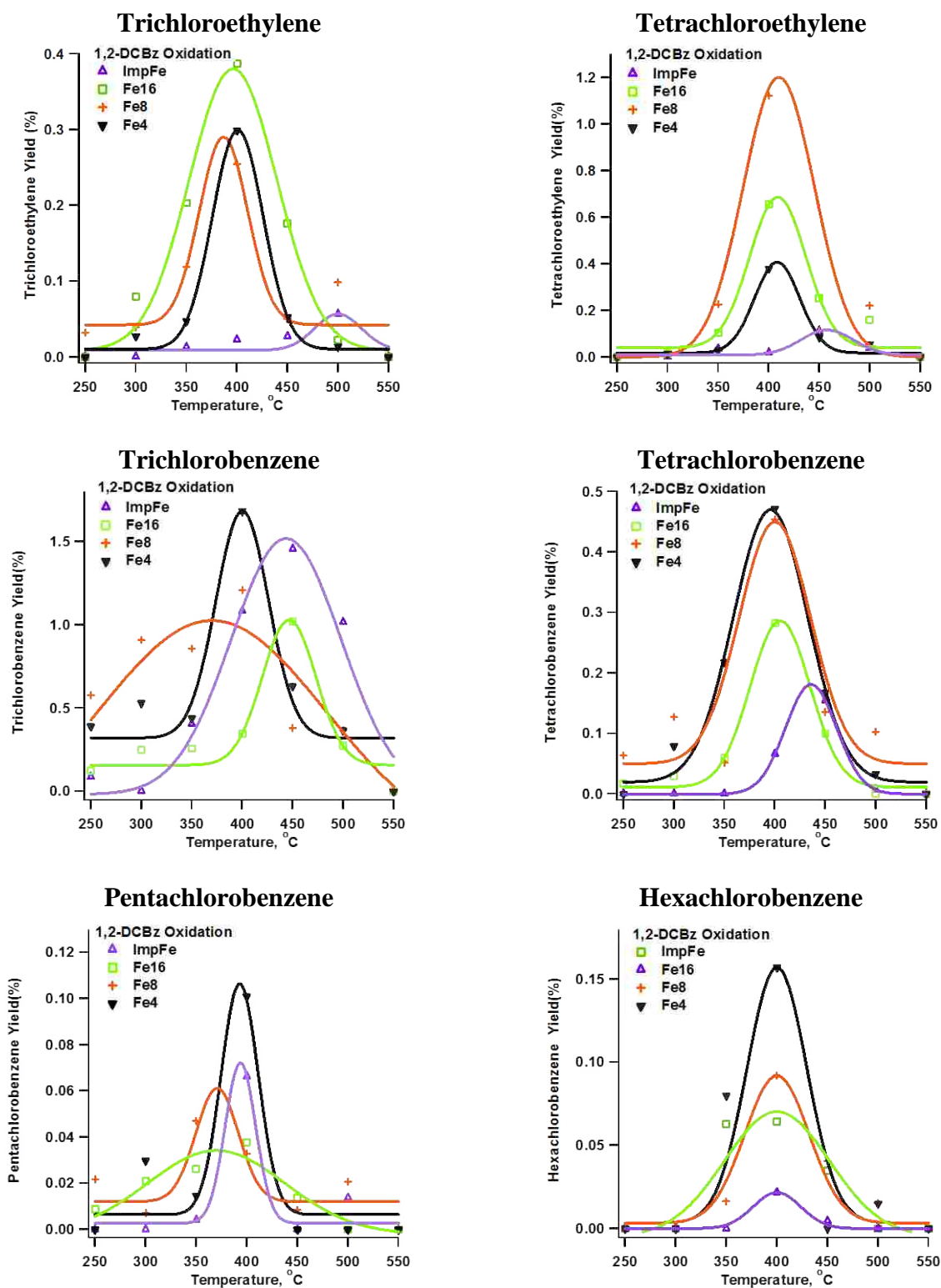
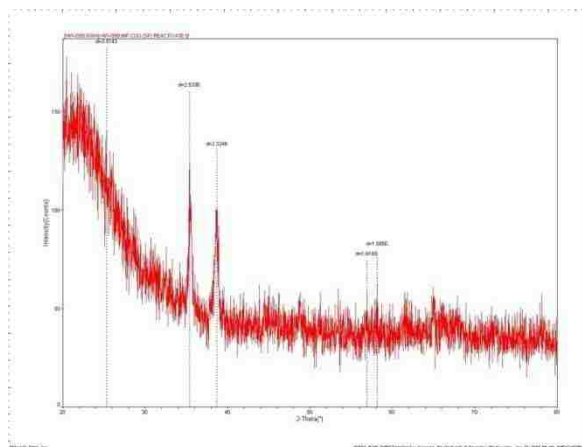**E:** Products Yield of Chlorobenzene over Fe_2O_3/silica under Pyrolytic Condition
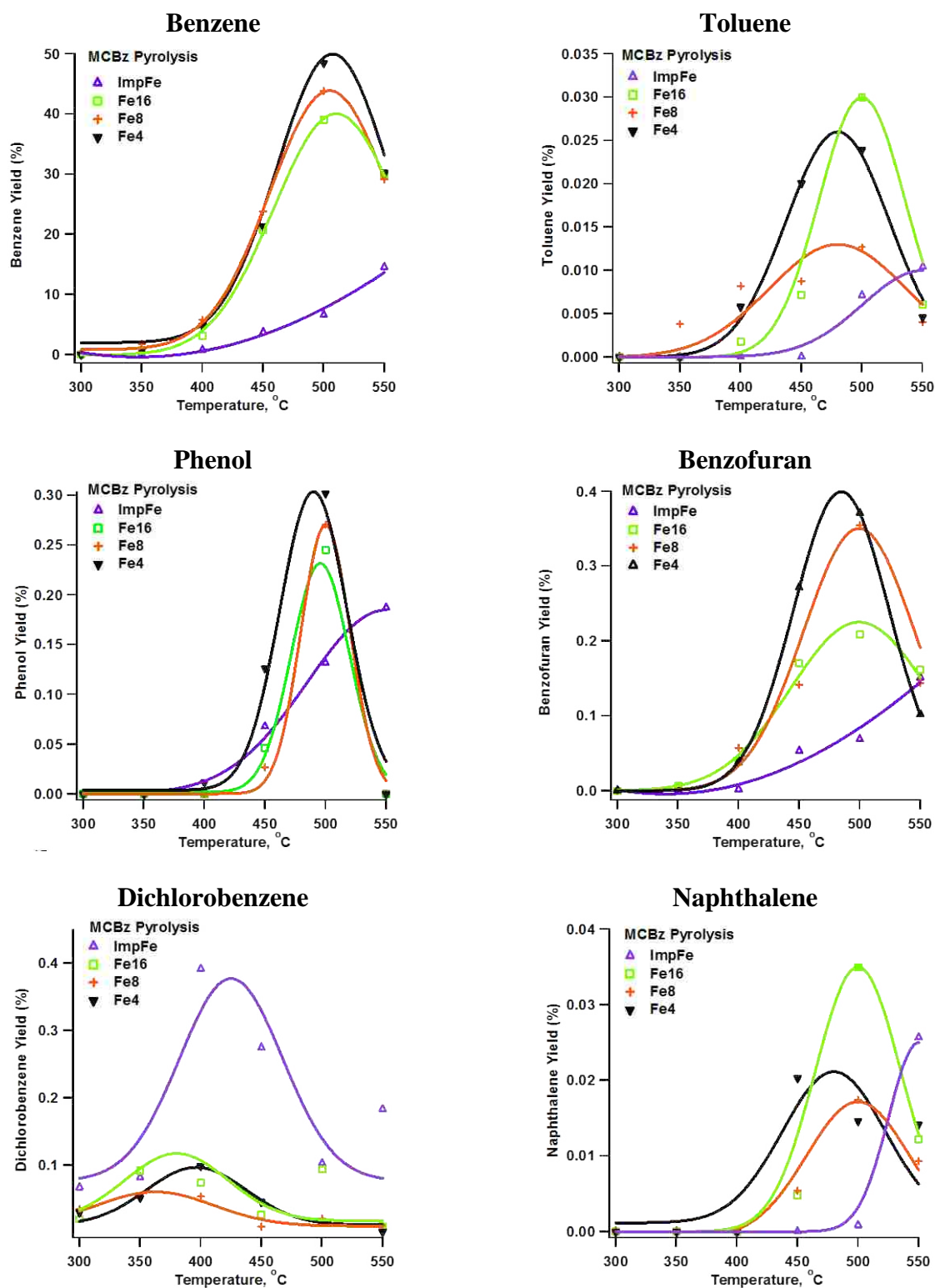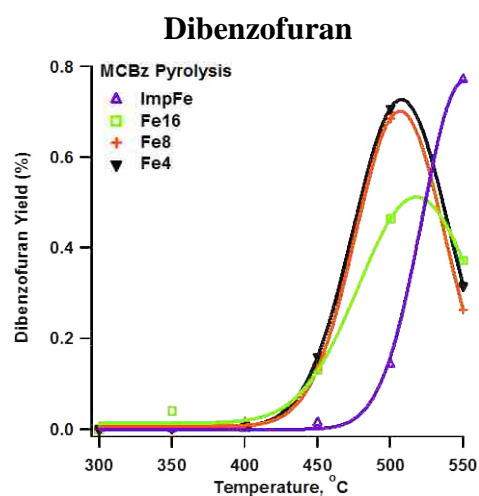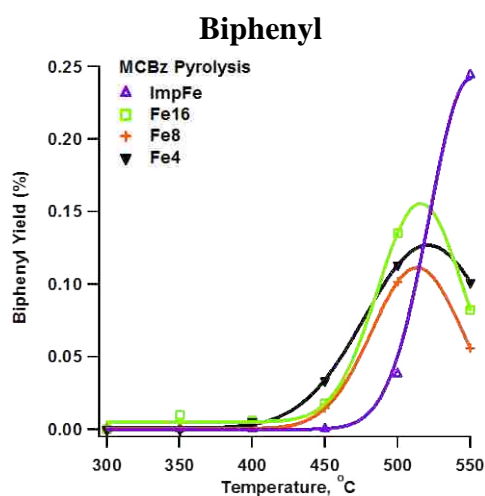
Biphenyl

Dibenzofuran

F: Products Yield of Chlorobenzene over Fe_2O_3/silica under Oxidative Condition

Benzene

Trichloroethylene

Dichlorobenzene
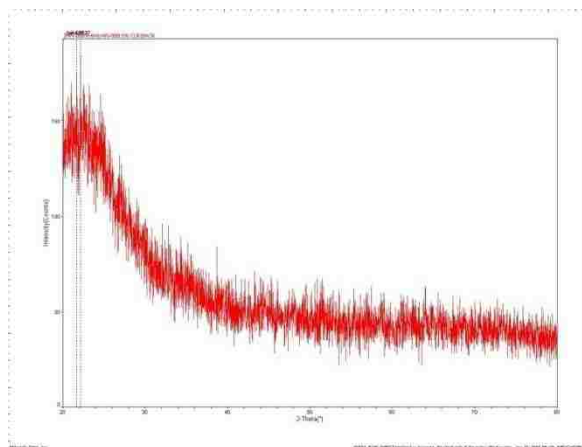

153
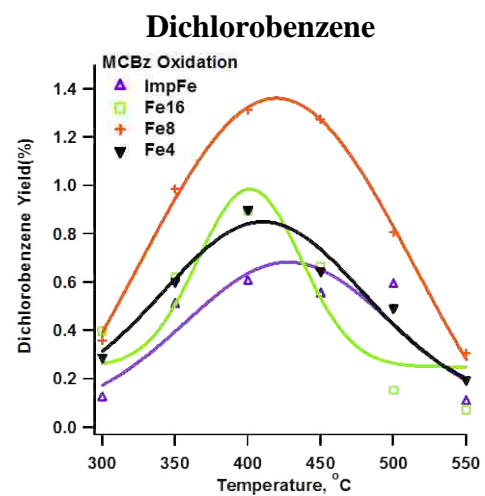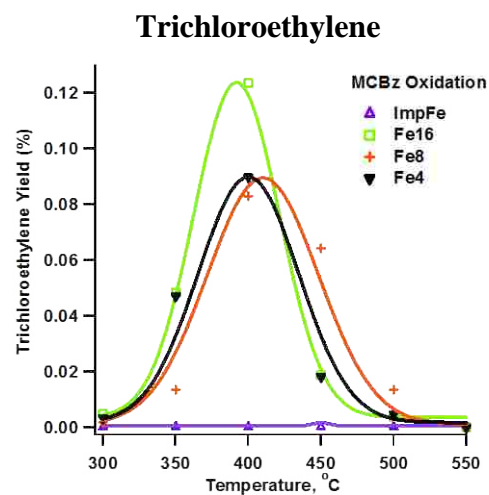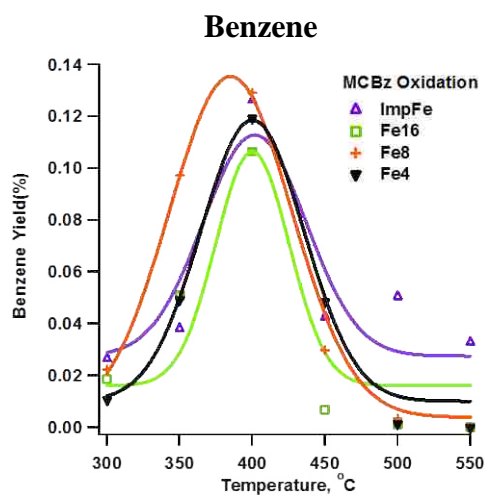
APPENDIX 3. XRD ANALYSIS OF COPPER OXIDE CATALYST SAMPLES (5 WT.% ON SILICA)
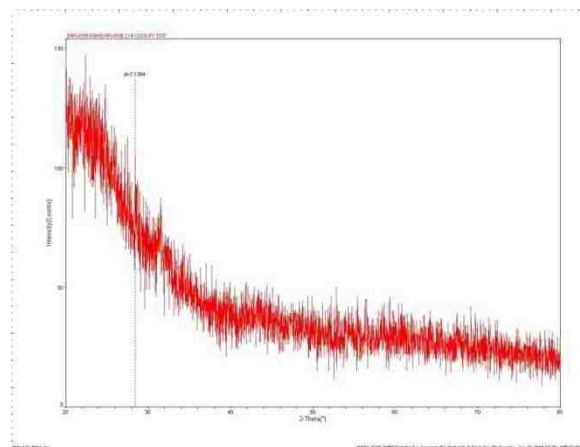

IMPCu
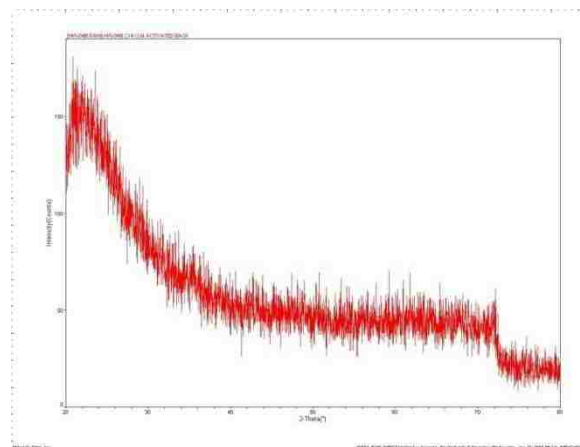
G4Cu4

G4Cu8

G4Cu16

VITA

Hongyi Wu was born in December, 1977, in Shantou, China. He earned a Bachelor of Science degree in materials science and engineering from University of Science and Technology of China in June 2002 at Hefei, P.R.China. He went on to pursue a doctoral degree in environmental chemistry at Louisiana State University in Baton Rouge, Louisiana. His research was under the direction of Dr. Barry Dellinger and Dr. Erwin Poliakoff. He will receive his Doctor of Philosophy degree in May, 2010.